2016

Atomistic Mechanisms of Stress Evolution for Gold Thin Films on Nickel Substrates via Molecular Dynamics Simulations

Murat Al
Lehigh University

ATOMISTIC MECHANISMS OF STRESS EVOLUTION FOR GOLD THIN FILMS ON NICKEL SUBSTRATES VIA MOLECULAR DYNAMICS SIMULATIONS

by

Murat Al

Presented to the Graduate and Research Committee

of Lehigh University

in Candidacy for the Degree of

Doctor of Philosophy

in

Mechanical Engineering

Lehigh University

January, 2016

DISSERTATION SIGNATURE SHEET

Approved and recommended for acceptance as a dissertation in partial fulfillment of the requirements for the degree of Doctor of Philosophy.

_____

Date

_____

Edmund B. Webb III

Dissertation Director

_____

Accepted Date

Committee Members

_____

Edmund B. Webb III

_____

Herman F. Nied

_____

Terry Delph

_____

Richard P. Vinci

_____

Wojciech Z. Misiolek

ACKNOWLEDGEMENTS

As I am about to turn around a corner stone in my life, I have realized once again that I owe my everything to God who have surrounded me with so many wonderful people. The very first thanks goes to my dear mother Arife and father Mustafa, the most special and most precious gifts that I was blessed with at the beginning of my life journey. They are the two, who have been thinking of me more than I do, and praying for me since the first day. Then I was introduced a man, my only but is worth many, my brother, to whom I realized my love little later but have been growing since then, with whom I felt stronger and for whom I have felt grateful to God many times. Those two ladies, my aunts, who have been a second mother to me since the very first day also deserve special thanks.

And my beloved one, thank you for loving me so much and trusting me that you accepted to be my wife and left all your beloved ones behind to come to US with me. I owe you my dreams which have being turning into reality every day. Your emotional support has helped to overcome problems I came across during my dissertation study. No words would be enough to express my gratefulness and love to you. We, all, love you so much!

My dear son Mehmet, you are 2.5 years old, too little to understand how precious you are to me and how much I love you. I am not able to express my feelings about you and even if I could you can truly understand what I feel only when you have your own child. That's for sure,

since it happened to me. Thank you for being with us, thank you for your running to the door and hugging me in cheers.

Melek Seniha'm, our little 'Angle', you did not need to hurry to join us; I would still mention you in here. Thank you in advance for your hugs and kisses, too. I owe you two, Mehmet and Melek Seniha, the highest title I would get, being your "Father" in this life and same is true for your "Mother" as well.

I would like to express my sincere gratitude to my advisor Edmund B. Webb III for his great academic guidance and personal support. It was a pleasure to work with him as one of his first graduate students.

Besides my advisor, it was also a great privilege to work with Terry Delph, Herman F. Nied, Richard P. Vinci, and Wojciech Z. Misiolek in my dissertation committee. I owe thanks each of them for their insightful comments and encouragement that incented me to widen my research from various perspectives.

There are many special people I wish I could be able to put their names in here. Those are my dear teachers, who changed my life, who guided me towards the truth which shaped rest of my way of understanding and living in this life. And of course, my dear friends, with whom I shared rooms, accomplished great things, and had unforgettable memories; thank you for every odd second that we spent together.I also want to thank to Baiou Shi, with whom I worked together in the same lab for 5 years. I wish you best in your future career.

Finally, I want to thank all faculty and staff in MEM Department for their helps throughout my dissertation studies.

Table of Contents

List of Tables

List of Figures

Abstract

Evolution of deformation and stress in growing thin films has been studied in this work using computational simulations that resolve matter at atomic length and time scales. Thin films are ubiquitous in technology; further, deformation in structures with at least one very small dimension (e.g. thin films) manifests correspondingly large strain and stress, with concomitant effects on device performance. Knowledge is lacking about the spatial and temporal stress distribution in growing thin films and how this relates to specific mechanisms of stress evolution. Thus, developing highly detailed, fundamental atomic scale understanding of stress evolution during thin film growth is important to optimizing humankind's ability to engineer useful devices based on thin film technology.

It is well known for bulk systems and analytically has been shown that stress localization occurs around defects, edges, vacancies or impurity regions. However, in thin films, particularly for dissimilar material interfaces, analytical solutions are not available. For the surface layers of films laying on the substrate of a dissimilar material, the stress distribution analysis around defects becomes more challenging. Herein, spatial and temporal distribution of deformation and stress are presented for different thin film formation events including 1) sub-monolayer growth during an early film nucleation stage, 2) coalescence of adjacent monolayer 'islands', and 3) post-coalescence equilibration during subsequent film growth. Stress behavior during these events was evaluated spatially and temporally to reveal direct connections between atomic scale film growth behavior and the associated stress evolution.

Validity of the stress computed via local computations of the virial expression for stress in a system of interacting particles was checked by comparing to results obtained from

considerations of local atomic deformation in conjunction with existing expressions for epitaxial thin film growth stress. For the geometries studied here, where a monolayer of film with a highly characterized linear defect, a stacking fault, was simulated for coalescence, fairly g*ood agreement was found. This result demonstrates that, for similar defects at the surface layer, with sufficient sub-ensemble averaging of the standard virial expression for stress, semi-quantitative spatial stress distribution information can be obtained from atomic scale simulations.*

Using our validated stress computation method, we reveal significant stress localization during thin film growth processes, leading to pronounced differences in maximum and minimum stress observed over very small spatial extent (of order multiple GPa over 3-6 nm distances). One prominent mechanism of stress localization revealed here is coalescence between adjacent growing islands. Coalescence eliminates surface energy but it typically occurs at the expense of generating elastic energy. For geometries explored here, stress manifesting during coalescence is highly localized. Atomic structure in stress localized regions is presented and shown to agree well qualitatively with a locally deformed structure (i.e. corresponding gradients in deformation). Though MD simulations are constrained temporally, relatively long simulations (hundreds of ns) were employed to reveal any evidence of temporal evolution. No such evolution was observed, lending confidence that localized stress states are thermodynamically meta-stable to stable. Furthermore, a size dependence study was employed to verify that results obtained herein extrapolate to film dimensions typically employed in practice. While stress relatively far from coalesced regions was shown to go to zero with increasing system size, neither the extent of stress manifestation spatially nor the peak magnitude in stress/strain showed notable dependence on system size.

Stress relaxation during subsequent film growth is also presented and shown to preferentially eliminate localized deformation in the coalesced region. However, significant

lattice mismatch for the system explored here is predicted by epitaxial thin film stress theory to lead to misfit dislocation generation for of order one to two monolayers of film material. In direct agreement with theoretical predictions, simulations here showed dislocation generation occurred, relieving misfit stress, after roughly a second monolayer was deposited. Again, deformation and stress due to defect generation are explored and shown to exhibit significant localization.

In concluding, the implications of results presented are discussed, including the effects that stress localization can have on film properties. We note that success here in computing local stress on such small spatial scales bodes well that future investigations at the atomic scale can contribute quantitative stress knowledge to thin film growth theory development. We also highlight how results such as those herein can guide future development of continuum constitutive relations in the form of improved cohesive zone models. We finally point out simulation challenges that must be confronted for future similar work to extend success here to more general material systems as well as thin film growth geometries.

Chapter 1 Introduction

Advances in technology have made possible the fabrication of device components or device components with size down to a few nanometers. This novel technology has been broadly utilized in optoelectronics, piezoelectric and photovoltaic technologies, magnetic storage devices, and conductor/semiconductor industries. In order to attain the required properties for materials and to have the devices function as expected, atomic level control over the surface shape, material properties, stress generating mechanisms is desirable [1].

In many of these applications average stress and its distribution over the parts either directly affect the performance of the part or it act as one of the major driving mechanisms by which devices may be formed (i.e. stress driven self-assembly) [2]. The influence of stress on material properties can best be understood if there exists thorough knowledge on the magnitude of stress that manifests in a given device or a material structure. Property dependence on stress manifests for materials at the macroscale as well as for materials fabricated at smaller scales; however, because deformations in small structures correspond to larger strains, the influence of stress/strain on material properties might be more pronounced for small structures. Intimately connected to these observations and relevant to macroscale features and smaller, non-uniformity of stress evolution must be examined to quantify how well average stress in a structure (for example, as obtained from experiment) reflects stress distribution throughout the structure.

In the class of material structures with at least one dimension being very small, thin films stand out as perhaps the most ubiquitous. Thin films have one dimension that is relatively small, with many technologically relevant films possessing thickness of a few microns or even into the

nanometer scale [3]**.** Thin films are widely used as coating material (for aesthetic purposes or in order to enhance optical, electrical, chemical, mechanical or magnetic performance for relevant applications) or as a sheet from which identical parts are cut (See Figure 1-1). Predictability and controllability of stress is technologically highly relevant since effects due to stress/strain in determining thin film properties and performance are significant.

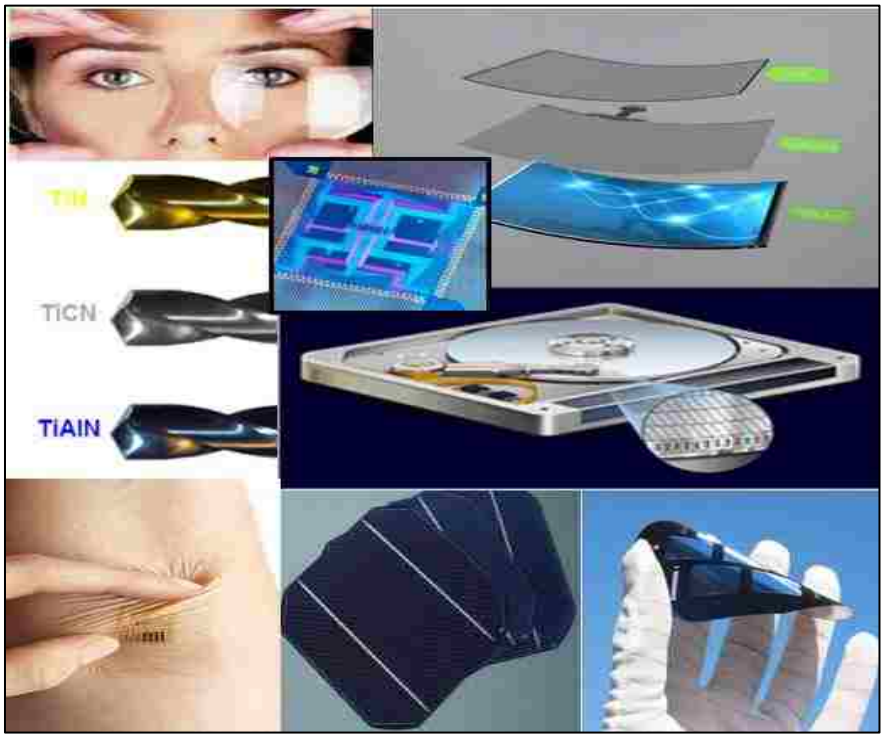

Figure 1-1 Examples of thin film applications from various fields of the industry are shown.

Different film deposition methods are utilized (i.e. electron beam, sputtering, evaporated vapor, chemical vapor etc.) varying according to the materials or film properties required by the specific application area. Generally for all growth methods, thin film growth involves removal of the film material from some bulk and depositing it on to a surface (substrate) until the film reaches the required thickness. Alternatively (or additionally) material might be deposited and subsequently etched away in some fashion to achieve a desired film geometry and chemistry.

Stress, which has not been quantitatively well explained in thin films, can arise due to different mechanisms such as lattice mismatch, grain growth, different thermal expansion rates, defect/vacancy annihilation etc. [4]. Thin films have been observed to exhibit different stress behaviors both during deposition process and after interruption or completion of the deposition [5], [6]. Besides potentially altering properties of the thin film material, stress in thin films may also cause film degradation, delamination, peeling or other mechanical defects. It can be seen that effects due to stress can be either beneficial (e.g. tuning a material's properties) or detrimental (e.g. mechanical failures) depending on the application. In Figure 1-2 below, self-assembled nanostructure of GDC islands are shown which formed due to the residual tensile stress. The picture on the right is an example for mechanical failures in thin films caused by stress, where Au thin film is peeled off the PMMA (Plexiglas) substrate after being heated due to the thermal stress caused by the different thermal expansion coefficients of the two materials. Therefore, characterization of the stress distribution and understanding stress generation and relaxation mechanisms is crucial for reliable manufacturing and better performance of emerging devices with very small feature sizes.

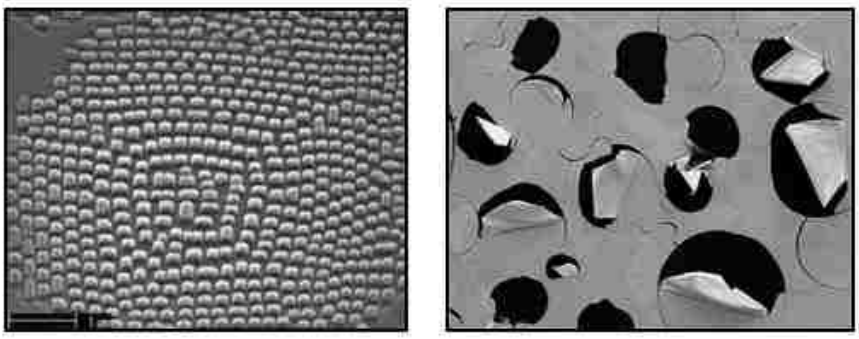

Figure 1-2 (Left) A planar film of gadolinia-doped ceria (GDC) deposited on the (100) surface of an yttria stabilized zirconia (YSZ) [7], (Right) Au thin film peeled off due to thermal stress (by Denis Michael)

Depending on the growth method, the growth parameters (i.e. deposition rate, temperature) and properties of the film/substrate materials chosen (i.e. melting temperatures, crystal structures, chemical interactions etc.) films may go through different morphological steps both during and after the growth process. Film growth types are classified according to different morphological evolutions and stress behaviors observed during the growth process. Growth types will be explained in detail in the following chapter.

Metal films have been studied for a long time driven largely by the use of many different metal or metal alloy films in the electronic industry. Thus, there exists significant experimental data in the literature relevant to stress evolution during metal film growth for various metals. The data provided is typically in the form of film force (or film stress) versus film thickness curves (see Figure 1-3) or stress evolution versus time curves which are obtained through substrate curvature measurements using X-Ray diffraction, or luminescence piezo-spectroscopy [7], [8]**.** The curvature measurements are related to stress-thickness via Stoney's equation, which will be discussed in detail in the proceeding section.

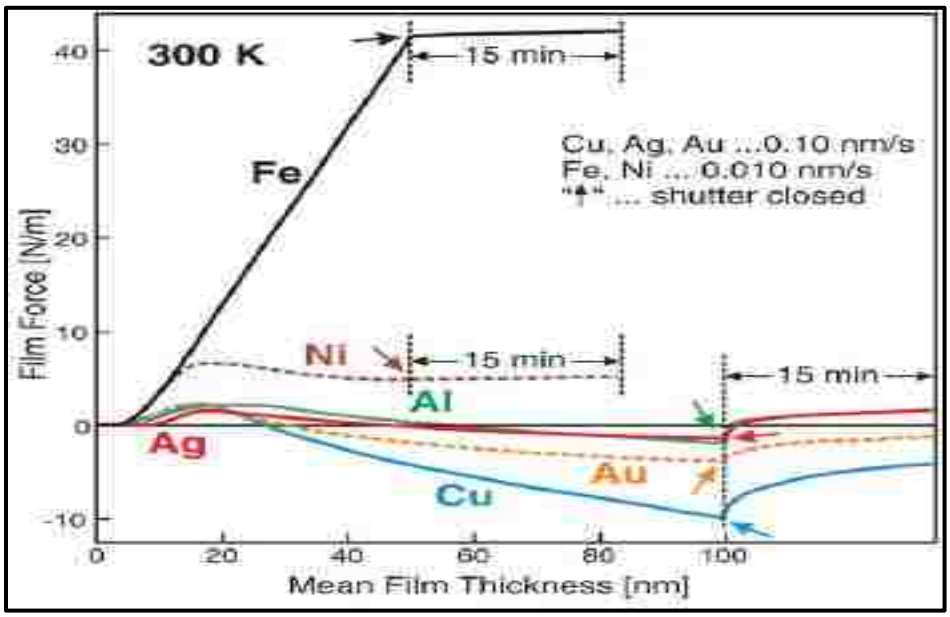

Figure 1-3 Film stress evolution during VW growth of evaporated FCC metal films on mica (001); the effect of interrupting growth on stress is also shown [1].

Figure 1-3 shows that for different materials under the same deposition conditions very different stress evolution data are obtained. Fe shows what is considered typical behavior for a low mobility metal in which only tensile stress is observed during growth. When growth is halted for 15 minutes, no relaxation is observed. Metals like Au, Cu, Ag and Al on the other hand, show tension, giving way to compression during growth and during the 15 minutes halt, tensile relaxation occurs. This is typical of high mobility materials. Mobility can be affected by temperature or surface chemistry as any given metal may show different type of behaviors at relatively high and relatively low temperatures. Thus, it is important to characterize the temperature at which a given data set was obtained (data shown in Figure 1-3 were all obtained from room temperature experiments). By taking the derivative of a film force (or stress thickness) versus film thickness curve like in Figure 1-3 above, one obtains the instantaneous stress (i.e. in the currently growing layer of the film). The overall change in the film force divided by the total film thickness gives a measure of the average film stress.

While data such as in Figure 1-3 have been invaluable in understanding evolution in thin film stress, systematic studies of stress *distribution* evolution are still needed to explain how the stress generating mechanisms (i.e. lattice mismatch, surface stress, grain boundary formation, recrystallization etc.) manifest stress concentration (or localization) during thin film growth.

In this study, "*stress localization*" refers to a spatial region in the material that experiences higher stress than the surrounding regions due to proximity to the stress generation event (e.g. coalescence of atomic islands). Thus, *stress localization* is used to avoid confusion with *stress concentration* as a term typically used in structural mechanics in regard to geometric features in a structure (e.g. holes, fillets, etc.).

Because stress evolution mechanisms are inherently associated with specific atomic behaviors, localization may occur on length scales inaccessible to experimental probing. Therefore, atomistic simulations may provide great insight about what magnitude gradients and maximum stress/strain result due to phenomena associated with stress evolution during deposition and thin film growth. If significant stress localization occurs, then there can be regions where maximum stress values are much larger than expected based on average stress. The evolution of these regions in position, size and stress magnitudes during and after growth should be elucidated because those regions are expected to be the sites where failure is most likely to initiate or material properties will be most altered by stress effects. In experiments, during deposition, randomly distributed atomic formations of different sizes and shapes are observed; different stress generating events take place simultaneously. Thus it is difficult to filter the effects of a certain mechanism and quantify it, although some notable experiments have been advanced that have explored highly characterized stress generation scenarios [10], [11]. Simulations can be manipulated to make the effect of a specific mechanism distinguishable. For example, introducing deposition during coalescence can allow us to see the effect of atom insertion into the surface and into evolving grain boundaries. Adatom steering – where a deposited atom's trajectory is altered due to non-uniformity in the surface morphology – can be directly observed. Changing the surface orientation allows one to explore how lattice mismatch stress manifests for varying surface structure. Changing the material pairs or manipulating the interatomic potentials that describe material interactions allows one to study the influence of underlying thermodynamics in determining stress evolution mechanisms and magnitudes. Lastly, altering the temperature can provide a better understanding on the effect of mobility changes.

The aim of this study is to achieve an understanding of atomic scale mechanisms of stress manifestation in metallic thin films with particular focus on the distribution of stress associated with specific mechanisms of stress generation via molecular dynamic (MD) method. Au film on

Ni substrate is modelled in LAMMPS [12], an open source MD simulation tool, to probe stress evolution during early film growth, coalescence and post-coalescence regimes of film growth. Au and Ni, both FCC metals, were selected since they display significant lattice mismatch. In this study, stress distribution evolution both spatially and temporally in metallic thin films during highly characterized stress evolution events associated with film growth is explored via MD simulations. Existing atomic interaction models for alloy systems will be used that are reasonably accurate in predicting relevant material properties for metals. Additionally, these models are simple enough that we can simulate "large" system sizes for "long" times, (relative to atomic simulation length and time scales).

In a relevant study, where they applied MD method, Luedtke et al. modeled deposition of Au onto Ni and vice-versa using the EAM interatomic potential (i.e. material interaction) model used here (discussed below). They showed via MD simulations that different growth mode and morphology occurred based on whether Au or Ni was the growing film material [13]. However, they did not explore stress evolution in their models. To simulate the island coalescence process, different island geometries, (i.e. 2D single layer islands, 3D hemi-spherical or rectangular islands, etc.) can be prepared and simulated during coalescence. A number of prior studies have taken this path and revealed useful information about atomic mechanisms of stress evolution[14]–[17]. However, none of the prior work explored stress localization as is addressed here. Finally for the full film growth mode, deposition onto coalesced islands can be modeled and the stress evolution can be recorded and prior work exists exploring this regime with atomic models [18]–[20]**.** Again, though, no effort was made in prior simulations to describe spatial distributions of stress associated with specific stress evolution mechanisms such as coalescence. This presented study also aims to explore stress relaxation behaviors and to obtain dependence of stress on geometry in terms of magnitude as well as the spatial extent over which different mechanisms manifest stress.

After presenting the background information and theoretical explanations for the topics germane to this study in Chapter 2 and Chapter 3, I will review the relevant previous work in the literature in Chapter 4. Chapter 5 is dedicated to explanation of the simulation models used in this study and to the procedures followed throughout the simulations. Chapter 6 through Chapter 8 include the three specific cases modeled in this study which are stress evolution during early stages of island formation, stress localization observed during coalescence stage of Au thin film formation on Ni (001) substrate and stress localization relaxation by subsequent deposition onto the coalesced Au film monolayer, respectively. The dissertation ends with the chapter including the conclusion and future works proposals.

Chapter 2 Background Information

2.1 Surface Stress and Surface Energy

Surface stress is one of the fundamental phenomena in surface morphology studies which has to be well understood since it's associated with all solid surfaces and interfaces as a thermodynamic quantity [3], [21]. Surface stress is observed in fluid and solid systems as a result of difference in free energies of the bulk and the surface atoms. Additional stress occurs intrinsically during material deposition where distorted surface regions by adatom binding yield anisotropic stress generation. Stress can also be applied to the system externally by means of mechanical loading or pre-patterning the substrate surface by using the lithography methods or by applying an electric field to the piezoelectric particles embedded into the substrate. Resulting stress (surface and interstitial stress) change the system morphology by effecting the adatom binding locations and preferential adsorption sites.

For the purpose of analyzing the phenomenon, theoretical work has been carried out for decades for defining the surface stress. Gibbs has formulated excess free energy per unit area and defined it as the "reversible amount of work needed to create a unit area". This is the surface energy required to form new surfaces, exposing new atoms[3]. There is another surface quantity, surface stress, which is defined as the "reversible work required stretching an existing surface per a unit area." [22].

Surface stress is related but not equal to surface energy although they have the same units as N/m. Both surface stress and surface energy arises as a result of the difference in electron

density of the surface atoms than that of the bulk atoms. Surface atoms are in a lower density thus they will try to lower their energies by adopting an equilibrium spacing which is different than the bulk. Underlying bulk atoms will force the surface atoms to the epitaxial order with bulk lattice set up which will create the surface stress. It is the result of this competition between surface and bulk atoms which yields the curved shapes of the droplets [3], [22].

These two quantities are related such that stretching the surface increases total surface free energy which is given as G= γ.A. Thus we can define the surface stress tensor f_{ij} that relates the variation in G to the strain ε_{ij} [22], [23]:

$$(\gamma.\mathrm{A})/(\mathrm{d}\varepsilon_{ij}) = \mathrm{A}.f_{ij} \tag{2-1}$$

Surface stress is symmetric tensor of rank two and the relation between surface stress and surface energy can be also given as

$$f_{ij} = \delta_{ij}\sigma + d\sigma/d\varepsilon_{ij} \tag{2-2}$$

where the f_{ij} is the surface stress tensor, σ is the surface energy and ε_{ij} is the surface strain. In this , δ_{ij} σ on the right is proportional to the change in surface area due to strain and $d\sigma/d\varepsilon_{ij}$ being the change in surface energy caused by strain [24].

2.2 Thin Film Stress Measurement

Different methods are utilized in measuring the stress in thin films on top of a substrate. One is classical cantilever beam bending method which is applicable for plates, beams or discs where substrate, with film on, is clamped on one side and bended. The radius of curvature or the displacement at the very end is measured via differential capacitance techniques [3], [25]. For more precise results and critical measurements diffraction methods are developed. These methods utilize laser beams where their diffractions are caught by optical sensors as in MOSS-Multiple beam Optical Stress Sensors [26], [27].

There are other methods where the stress is directly measured by X-Ray Diffraction technique or LEED - Low-energy electron Diffraction Methods. Crystal lattice strain is measured and using the film's elastic properties stress value is derived [24].

Cantilever method is advantageous in terms of its continuous applicability during deposition process as well as after the deposition for recrystallization stage. For the thin films with thickness relatively much less than the substrate in all dimensions Stoney's well known given below can relate the stress of the film to the curvature measured [3], [25], [26].

$$\kappa = \frac{6 < \sigma > h_f}{M_s {h_s}^2} \tag{2-1}$$

In this h_f is the film thickness, h_s is the substrate thickness and M_s is the biaxial modulus where M_s= E/(1−ν), E being the bulk modulus and ν is Poisson's ratio. The $<\sigma>.h_f$ product, also known as the *"stress thickness"* or "*force per unit width",* is proportional to the curvature. "σ" is the average stress in the film but it is not uniformly distributed in polycrystalline films. Thus average stress is obtained by integration over the thickness of the film (see Eq. (2-3)).

If the time derivative of the Stoney's is derived considering the non-uniformity of the polycrystalline film two stress terms are obtained as seen below in Eq.(2-4) .

$$< \sigma >= \frac{1}{h_f} \int_0^{h_f} \sigma(z) dz \tag{2-3}$$

$$\frac{d\kappa}{dt} \sim < \sigma > h_f \frac{\partial \mathrm{h}_f}{\partial \mathrm{t}} + \int_0^{h_f} \frac{\partial \sigma(z,t)}{\partial t} dz \tag{2-4}$$

First term on the right hand side is the "incremental stress" which is the stress added of amount $<\sigma>h_f$ to the upmost layer at a rate dh_f/dt . The second term is the contribution of the timely change of average stress to the change in curvature. This term shows that the curvature is not only effected by the deposition of new atoms, but also the stress relaxations taking place within the film can also change the curvature [26].

The sensitivity of the cantilever beam measurements is closely related to the surface roughness where it decreases as roughness increases [28].

2.3 Thin Film Growth Methods

Thin films can be manufactured using different methods which can be classified into two main groups as Physical vapor deposition and Chemical deposition techniques. Methods are named after the processes applied for the activation of the film source material.

Main physical vapor deposition methods can be classified as Thermal evaporation, E-beam evaporation and Sputtering. Atoms are evaporated from the source by physical means like heating, high energy electron or inert-gas ions bombarding depending on the nature of the source material and transferred to the targeted surface thorough air. Thermal evaporation method is done by heating the source material up to its evaporation temperatures and is applicable for almost all metals excluding refractory metals like Chromium (Cr) and Tungsten (W) which have very high melting points where heating is not feasible for evaporation [1]. E-beam evaporation method used for the refractory metals sends high energy electrons to the target film material instead of heating it. This method has the disadvantage that the some portion of the energized electrons can hit the substrate film pair and damage the film structure. Sputtering is another physical method which eliminates the necessity of high heat energy in thermal evaporation. Inert-gas ion beams are sputtered onto the source after being energized and the evaporated atoms are deposited onto the substrate [1], [27], [29].

Chemical deposition methods includes chemical reactions taking place between activated substrate and source material at the certain conditions yielding film material as a product on top of the substrate. Depending on the environment this can be applied in two ways as one being chemical vapor evaporation where substrate is exposed to vaporized source material for reaction, and the other chemical solution deposition where reaction takes place in liquid (electroplating).

Methods are different regarding the amount of energy to be provided, uniformity of the produced film (where chemical methods perform better), impurities involved, grain sizes and allowed deposition rates. All these cases mentioned above have been studied separately as the factors acting on the intrinsic stress generation on thin films [24], [30], [31]. Deposition methods have also been compared in terms of their effects on stress evolution [1].

2.4 Thin Film Growth Modes

During deposition, nucleation initially starts at substrate defective regions since they are energetically more favorable [3]. Later on depending on the competition between the surface and interface free energies in the film-substrate system growing mode is determined (see Figure 2-1). There are many factors which contribute to the resulting film morphology and stress behavior during and after the deposition process. (i.e. Temperature [3], [32], [33], pressure [34], [35], deposition rate [31], [35], surface orientation [36], surface defects [37]–[40], surface chemistry [41], growth method applied [1], material pairs [1], [31], [32] etc.) Leaving the detailed discussion for those factors for subsequent sections, the major growth modes will be covered here.

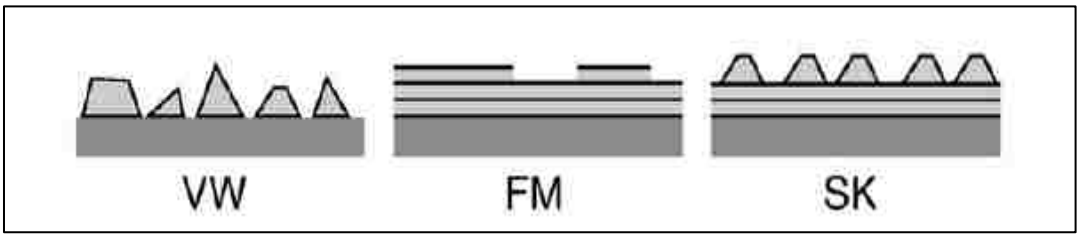

Figure 2-1 Schematic representation of the Volmer-Weber (VW), Franc-van Der Merwe (FM) and Stranski-Krastanow (SK) growth modes are shown.

2.4.1 Volmer–Weber (VW) Modes

This type of growth is also known as Non-Wetting Growth where due to the low film substrate interactions initial nucleation is starts in the form of distinct 3D islands. Small islands join together forming bigger islands to attain an equilibrium condition but as deposition continues a critical size is achieved where islands start to coalesce. At this coalescence (networking) stage

first grain boundaries form and islands grow together. Then channel stage takes part where all the deposited material is used to fill the gaps in the open channels, no significant increase in the film thickness is observed. Finally the continuous film stage is reached where film thickness increases linearly keeping the grain size average constant. Stress behaviors have been observed to be different during all these stages and after the deposition ends. In general Compressive, Tensile and Compressive stresses (CTC) have been recorded in nucleation, coalescence and continuous film stages, respectively. This is the characteristic stress evolution regime for most of the VW type growth of high mobility films (FCC metals like Ni, Ag, Au, Al etc.) above certain temperatures [1], [27], [42] as discussed in the Introduction Chapter above (see Figure 1-3). For film materials of low mobility, tensile stress cannot be relaxed and film tensile stress increases as deposition continues and does not relax when deposition ends [43]. Residual stress can vary depending on the relaxation mechanisms dominating the system [1], [3], [26], [29], [42], [44].

Thin films displaying VW type of growth are observed to have different microstructures. Depending on the substrate temperature three distinct microstructures were obtained. At low temperatures columnar growth, at medium temperatures polycrystalline and at relatively higher temperatures epitaxial VW growth is observed [1], [6], [32].

No stress is built up in epitaxial growth of VW type films due to the low film-substrate interaction forces in nucleation and island growth stage. The stress is compressive at coalescence stage opposite to the polycrystalline VW films [32](See Figure 2-2 below).

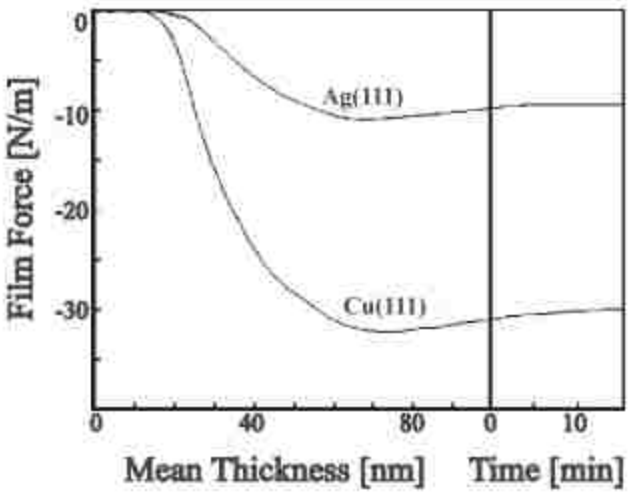

Figure 2-2 Epitaxial VW type of films; Ag/mica (001) and Cu/mica (001) deposited at 570 K and 715 K, respectively.

2.4.2 Franc-van Der Merwe (FM) Modes

When adhesion free energy is equal to the surface free energy then the thickness vanishes and 2D films starts forming, wetting the surface completely. They pass through the same stages as VW mode in 2D (i.e. nucleation, coalescence, continuous film formation). Second layer does not form before the first layer is completed [1], [3]. This form is, thus, known as Layer-by-Layer Growth mode. In a molecular simulation study, FM type of growth was achieved and it was seen that compressive stress was generated till the first monolayer was created, and then stress curve changed to tensile when deposition goes for the second layer, which indicated the thickness dependence of the stress generation [45].

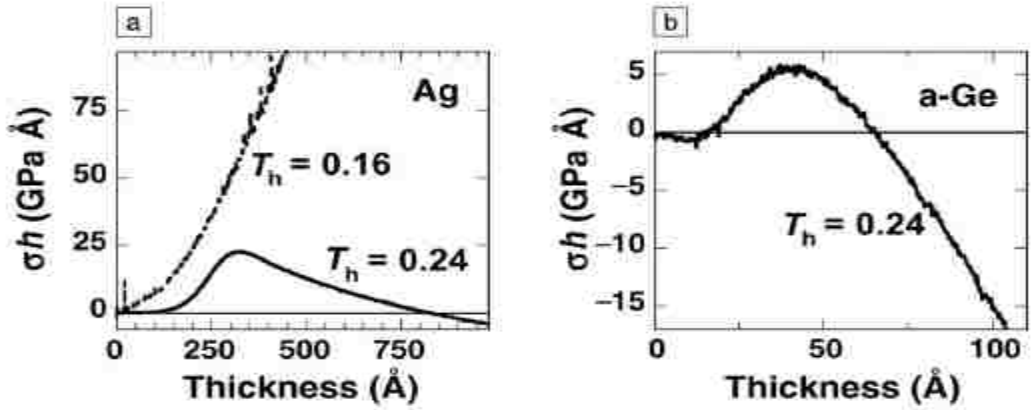

Figure 2-3 a) Ag has high mobility at elevated T showing CTC behavior typical to VW growth, and has low mobility at lower T where only tensile growth is seen. b) a-GE displaying high compression at the post coalescence regime [42].

2.4.3 Stranski-Krastanow (SK) Modes

In this type of growth, surface free energy of the film material cancels out with the adhesion energy during the first steps of the deposition, which results in continuous layer deposition as in FM mode. The initial layers deposited may have mismatches with substrate or there may be some alloying interaction occurred in the substrate interface which affects the surface free energy of the film significantly. These changes in the surface energy in the deposited film layer makes it act like a different substrate surface for the deposited film material thus yielding new nuclei to form like in VW mode [21]. In SK type of growth stress relaxation is achieved by formation of 3D islands or misfit dislocations between islands. SK type also has its three growth stages starting with formation of wetting layer, then nucleation, growing islands and coalescence of the islands [32].

Chapter 3 Theory and Computational Methods

System properties expressed at macroscopic levels are the values obtained by averaging the sum of the respective quantities from each individual atom or molecule included in that particular system. Statistical mechanics enables us to exploit the microscopic data of the particles (i.e. position, velocity, etc.) generated by computer simulations to derive observable quantities (i.e. pressure, energy, heat capacity, etc.) for the macroscopic system.

In this section basics of the statistical mechanics theory will be presented and an overview of the molecular dynamics method (MD) will be discussed focusing on topics most relevant to the work done during this doctoral study.

3.1 Theory of Statistical Mechanics

Statistical mechanics is the bridge connecting the microscopic information like atomic position and velocities to the macroscopic thermodynamic or kinetic properties of the system. Along with the advance in computational capabilities, it has been possible to solve equations of motion for higher number of particles in a simulation and finding out more accurate results for those mathematical expressions which lead to realistic predictions for the macroscopic properties.

Thermodynamic state of a system can be expressed in terms of some of the parameters like number of particles (N), temperature (T), and pressure (P) so that other properties can be derived from them via equations of state and fundamental thermodynamic equations. A

multidimensional space can be represented by position (p) and the momenta (q) of the particles as its coordinates. This space, which is called "phase space", would have 6N dimensions for a system of N atoms. For a particular point in phase space (Γ), any instantaneous property *A* can be given as a function of Γ, i.e. *A*(Γ). As time evolves *A*(Γ) will also change and the macroscopic value for A will be the time average of A(Γ) taken over a long time.

$$A_{obs} =< A >_{time} =< A(\Gamma(t)) >_{time} = \lim_{t_{obs}\to\infty} \frac{1}{t_{obs}} \int_{0}^{t_{obs}} A(\Gamma(t))dt \tag{3-1}$$

Knowing the Newton's equations of motion one can solve those differential equations in a computer but it is not possible to extend the integration to an infinite time limit. Instead MD proposes averaging the property in finite number of time steps (τ) towards the finite time t_{obs}. Time averaging equation above in Eq. (3-1) can then be written as follows:

$$A_{obs} =< A >_{time} = \frac{1}{\tau_{obs}} \sum_{\tau=1}^{\tau_{obs}} A(\Gamma(t)) \tag{3-2}$$

This is the MD time average for the property *A*, but the experimental averages of the observable averages are the ensemble averages. In statistical mechanics MD calculation of time averages for the thermodynamic properties is substituted by ensemble averaging by Gibbs. An ensemble is a collection of all possible microsystems which possess the same thermodynamic state (temperature, pressure, chemical potential, etc.) with its macroscopic system but different microscopic properties like position and momenta of the particles (See Figure 3-1). According to the ergodic theory (which says all microstates attain equal probability to occur over a long time), ensemble average is equal to the MD time average of the system. This approach helps to avoid

dealing with the complexity due to the large number of particles in the system contributing to the property $A(\Gamma(t))$.

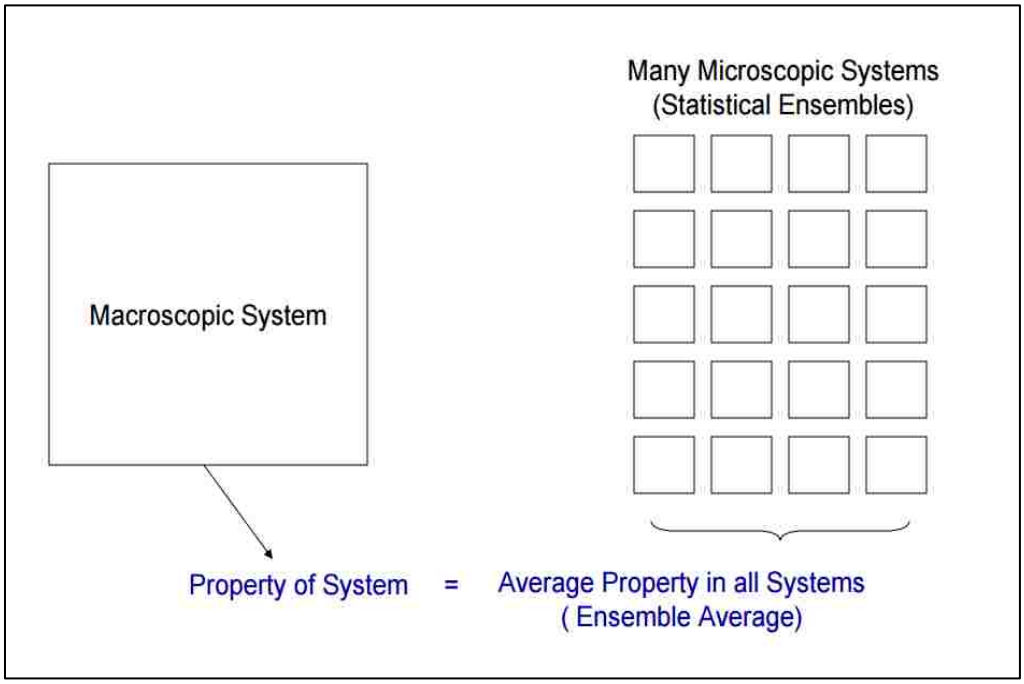

Figure 3-1 A phase space on the left, and microscopic systems contained in the macroscopic system which also represent the statistical ensembles are shown.[46]

Distribution of points in the ensemble are governed by *probability density function* $\rho(\Gamma)$, which varies according to the statistical ensemble chosen. Therefore, ensemble average of the property *A* can be expressed as a function of $\rho(\Gamma)$ as follows:

$$A_{obs} = < A >_{ens} = \sum_{\Gamma} A(\Gamma)\ \rho_{ens}\ (\Gamma) \tag{3-3}$$

In this equation, $\rho_{ens}\ (\Gamma)$ can be given in a more convenient form as:

$$\rho_{ens}(\Gamma) = \vartheta^{-1}{}_{ens} w_{ens}(\Gamma) \tag{3-4}$$

$$\vartheta_{ens} = \sum_{\Gamma} w_{ens}(\Gamma) \tag{3-5}$$

where w_{ens} is the weight function and ϑ_{ens} is the partition function (sum of all states) which is a function of the thermodynamic properties of the specific ensemble. (Discussed in detail at the end of this section) Substituting these equations into Eq. (3.3) we obtain the ensemble average equation as:

$$A_{obs} = < A >_{ens} = \sum_{\Gamma} A(\Gamma) * w_{ens}(\Gamma) / \sum_{\Gamma} w_{ens}(\Gamma) \tag{3-6}$$

As proposed by the ergodicity hypothesis, A_{obs} computed by time averaging in the long time limit in Eq.(3-2) gives the ensemble average computed above in Eq. (3-6).

$$< A >_{ens} = \frac{1}{\tau_{obs}} \sum_{\tau=1}^{\tau_{obs}} A(\Gamma(t)) \tag{3-7}$$

This relation in Eq. (3-7) between statistical mechanics and the MD computations basically depends on the assumption that for an indefinite time, the system of ensembles will eventually pass all possible states, and therefore MD tool should generate enough representative configurations to verify the equality mentioned above.

There are different statistical ensembles which vary depending on the fixed macroscopic parameters by which the thermodynamic state of the system is characterized. Most common ensembles are:

- *NVE-Micro-canonical ensemble:* Number of atoms (N), volume (V), and energy (E) are fixed. This corresponds to an isolated system where there is no exchange of energy or particle with the environment.
- *NVT-Canonical Ensemble:* Number of atoms (N), volume (V), and temperature (T) are fixed.
- *NPT-Isobaric-Isothermal Ensemble:* Number of atoms (N), pressure (P), and temperature (T) are fixed.
- *μVT- Grand canonical Ensemble:* Chemical potential (μ), volume (V), and temperature (T) are fixed.

Thermodynamic quantities which are not fixed in the ensemble are computed via ensemble averaging for particular state points using the appropriate probability density and relevant partition functions.

For example, in the micro-canonical ensemble (NVE), probability density corresponds to a phase space of constant energy (E), and it is proportional to:

$$\rho_{NVE}(\Gamma) = \delta(H(\Gamma) - E) \tag{3-8}$$

where $H(\Gamma)$ is the Hamiltonian for the total energy as a function of the set of state points with six coordinates (3 for positions and 3 for momenta). Delta function selects only the states which satisfy the desired energy level. The partition function for the NVE ensemble is:

$$\vartheta_{NVE} = \sum_{\Gamma} \delta(H(\Gamma) - E) \tag{3-9}$$

For a quasi-classical expression, for an atomic system, the partition function for the NVE ensemble can be written:

$$\vartheta_{NVE} = \frac{1}{N!}\frac{1}{h^{3N}} \int d\boldsymbol{r}\, d\boldsymbol{p}\, \delta(H(r,p) - E) \tag{3-10}$$

where the integration is over 6N phase space, and the Plank constant h is for the zero entropy for the ideal gas.

And lastly, the thermodynamic potential function is given as negative of entropy:

$$-\frac{S}{k_B} = -\ln \vartheta_{NVE} \tag{3-11}$$

Similarly, for the canonical ensemble NVT, where the temperature is the thermodynamic property kept fixed, the probability density corresponds to the Boltzmann function:

$$\rho_{NVT}(\Gamma) = \exp(-H(\Gamma)/k_B T) \tag{3-12}$$

together with the partition function (Eq.(3-14) is for a quasi-classic atomic system)

$$\vartheta_{NVT} = \sum_{\Gamma} \exp(-H(\Gamma)/k_B T) \tag{3-13}$$

$$\vartheta_{NVT} = \frac{1}{N!}\frac{1}{h^{3N}} \int d\boldsymbol{r}\, d\boldsymbol{p}\, exp(-H(r,p)/k_B T) \tag{3-14}$$

and the thermodynamic function where A is the Helmholtz free energy

$$A/k_BT = -\ln \vartheta_{NVT} \tag{3-15}$$

Computer calculates a set of trajectories in the phase space of 6N dimensions, depending on the set of configurations dictated by the statistical ensemble chosen for the specific simulation.

Partition function ϑ, which is defined particularly for each ensemble is a function of temperature T and the microscopic energies which are also determined by other thermodynamic properties like number of particles, system volume etc. It is highly significant in statistical mechanics studies since it allows reaching macroscopic properties via microscopic variables in combination with the fixed ensemble properties. In order to demonstrate how it works, take the canonical case (NVT) where temperature is constant.

Using the partition function given in Eq. (3-13) we can calculate the ensemble average for the system energy Hamiltonian H, (known as the internal energy U in thermodynamics) via Eq.(3-3) as follows:

$$< H >_{ens} = < U >_{ens} = \sum_{\Gamma} H(\Gamma)\ \rho(\Gamma) \ = \frac{1}{\vartheta} \sum_{\Gamma} H(\Gamma) \exp(-H(\Gamma)/k_BT\ ) \tag{3-16}$$

For convenience, we can substitute β for $1/k_BT$ exponent and denote function names in letters only. Then Eq. (3-16) can be in the form: (with substitution of the partition function ϑ from Eq. (3-13));

$$U = \frac{1}{\mathcal{Z}} \sum_{\Gamma} H \exp(-H\beta) \tag{3-17}$$

U can also be derived directly from the derivative of the partition function $\mathcal{Z}$ with respect to β as:

$$U = -\frac{1}{\mathcal{Z}} \frac{\partial \mathcal{Z}}{\partial \beta} = -\frac{\partial \log \mathcal{Z}}{\partial \beta} \tag{3-18}$$

Using this result we can derive other thermodynamic quantities, like specific heat, C which is temperature derivative of the energy U:

$$C = \frac{\partial U}{\partial \mathrm{T}} = \frac{\partial U}{\partial \beta} \frac{\partial \beta}{\partial \mathrm{T}} = \frac{\partial U}{\partial \beta} \frac{-1}{kT^2} = k\beta^2 \frac{\partial^2 \log \mathcal{Z}}{\partial \beta^2} \tag{3-19}$$

In thermodynamics specific heat C is also defined to be related to the entropy S, such that:

$$C = T \frac{\partial S}{\partial \mathrm{T}} = T \frac{\partial \beta}{\partial \mathrm{T}} \frac{\partial S}{\partial \beta} = -\beta \frac{\partial S}{\partial \beta} \tag{3-20}$$

This yields the integral below when equations (3-19) and (3-20) are solved together for C:

$$S = \int k\beta \frac{\partial^2 \log \mathcal{Z}}{\partial \beta^2} \partial \beta \tag{3-21}$$

which gives the entropy S as:

$$S = -k\beta \frac{\partial \log \mathcal{Z}}{\partial \beta} + k \log \mathcal{Z} \tag{3-22}$$

And finally, we can also write Helmholtz free energy F, by substituting the computed energy U the entropy S together with the temperature T into the free energy expression:

$$F = U - TS = -kT\ log\,\vartheta \tag{3-23}$$

It has been shown how statistical ensemble averages are calculated and how that atomic level information could be linked to macroscopic properties. In the following section MD method will be discussed as the computational application of statistical mechanics theory.[47]

3.2 Molecular Dynamic Method

Molecular dynamic (MD) is a computational method, which calculates positions, velocities and molecular orientations for a system of N particles by solving fundamental equations of motion using numerical integration and extracts ensemble averages for the macroscopic properties of the system via statistical mechanics techniques. It can be said that it is a computational experiment which can be used to test real experiments or to verify theoretical outcomes of equations hard to solve analytically.

From computational point of view of length and time scale limitations, atomistic modeling (Molecular Dynamics or Monte-Carlo) lies between quantum models for sub atomic particles and the continuum models which models realistic systems. Regions for time and length scale of the computational models are illustrated in Figure 3-2 below, where mesoscale methods are also shown which utilize both atomistic and continuum scale tools to some extent. MD, which is the computational method adapted in this study can access length scales of tens of nanometer for the structural feature sizes or spatial correlation distances. In a MD simulation minimum time step for the numerical integrations is defined by the fastest motion in the system which corresponds to a value around 1 femtosecond (10^{-15}second). Time step size also dictates the

maximum allowable time length depending on the computational resources available where it can go up to 100ns (10^8 time steps) (see Figure 3-2).

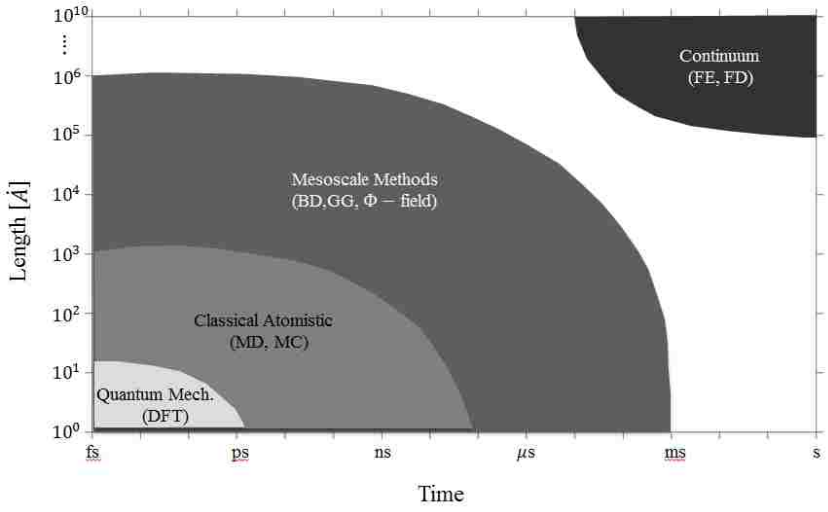

Figure 3-2 Schematic for the accessible length and time scales for different computational methods.

Researchers from different disciplines have been using MD method for wide range of applications. Some of the application can be named such that in chemistry and biochemistry MD is used for modelling biomolecular structures, membrane diffusion and protein folding, etc.; in statistical mechanics studies on theory of liquids or computing ensemble averages are carried out with MD calculations and in materials science MD simulations are performed to elucidate microscopic mechanisms of fracture, different types of crystal defect and their interactions, surface reconstruction and ***film growth*** etc.

In order to start computing iterative particle positions and velocities, MD requires initial conditions (position $\overrightarrow{r_o}$ and velocity $\overrightarrow{v_o}$) as an input together with the interaction model which govern the interactions between the particles.MD process steps can be summarized as : (Also see Figure 3-3)

1. Using current position and velocity and acceleration information calculate the successive respective values at the next time step
2. Evaluate force and accelerations using updated position data
3. Calculate any other variable of interest (energy, virial stress, temperature, etc.)
4. Continue iterations till required time limit (number of steps) is reached.

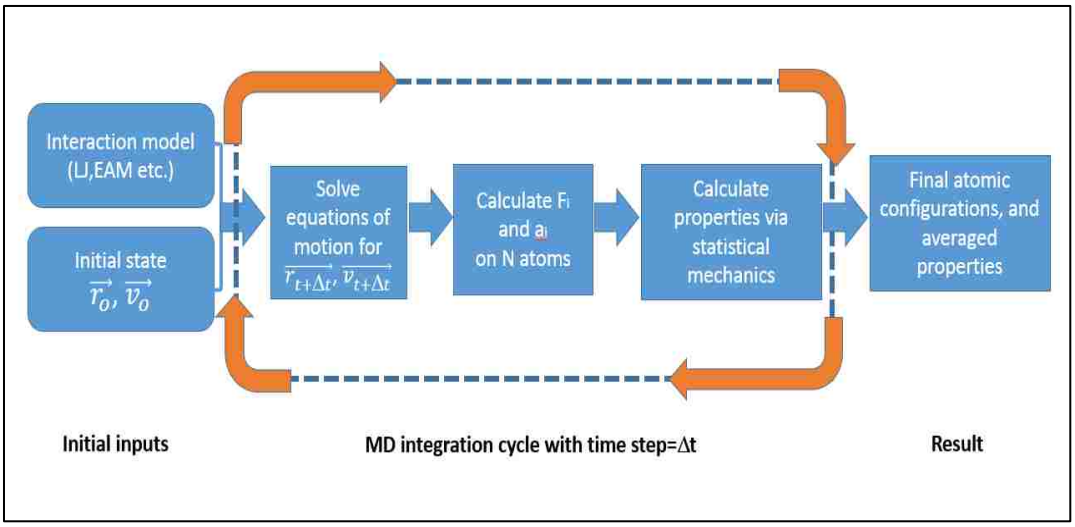

Figure 3-3 Basic steps in MD process

3.2.1 Numerical Solution of motion

Molecular dynamics simulations solve equations of motion based on well-known Newton's second law which relates force on a particle to the mass and the acceleration of the particle, such that:

$$F_i = m_i a_i \tag{3-24}$$

MD simulation calculates the force on each particle starting with the initial inputs for positions and velocities and updates the atomic configurations after every time step. This is a

deterministic method, since it can find out the system properties out of the trajectory computed out of the positions and velocity data of the particles.

Let's look at how MD determines the initial state variables and how it relates the solutions of equations of motion to system properties. First of all, initial positions can be obtained from experimental data such as the x-ray crystal structures of the materials being simulated. Initial velocities are chosen randomly from a Maxwell-Boltzmann or Gaussian distribution at a given temperature and are adjusted to zero momentum in overall for equilibrium as given in the equation below:

$$P = \sum_{i}^{N} m_i v_i = 0 \tag{3-25}$$

where P is the total momentum computed as the sum over N particles with m_i being the mass of the particle i and v_i being the velocity of that particle. Going back to the basic equation of motion, what we have is:

$$F_i = m_i a_i = m_i \frac{d^2 r_i}{dt^2} \tag{3-26}$$

$$a = \frac{dv}{dt} \text{ yields } v = at + v_0 \tag{3-27}$$

$$v = \frac{dx}{dt} \text{ yields } x = vt + x_0 \tag{3-28}$$

Eq. (3-27) and Eq. (3-28) yield the position as:

$$x = x_0 + v_0 . t + \frac{1}{2} a t^2 \tag{3-29}$$

Initial positon and velocities are provided as explained above and the last parameter is acceleration required to solve Eq. (3-29).It can be easily derived knowing that force is also

related to the system energy since the work done by the internal forces on the system reduces the potential energy since the system flows towards equilibrium. This relation is also the bridge which connects the position and velocity information to system properties, such that:

$$F_i = -\nabla_i V \tag{3-30}$$

where V is the energy. Substituting Eq. (3-26) we have

$$-\frac{dV}{dr_i} = m_i a_i \tag{3-31}$$

which also yields the expression for the acceleration:

$$a_i = -\frac{1}{m_i}\frac{dV}{dr_i} \tag{3-32}$$

3.2.2 Integration Algorithm

In the execution step of the MD cycles, equations of motion provided above with the initial configurational inputs (position, velocity) and the potential interactions can be solved numerically for the successive particle positions and velocities and system potential energies can be generated accordingly. Since potential energy is a function of all of the atomic position in the system, it requires numerical integration to solve the equations of motion for the atoms rather than analytically solving them which is impossible. For a successful numerical integration algorithm certain computational and theoretical constraints should be considered such that the code should be fast and simple and allow using a long time step. It should also be able to duplicate the classical trajectory as close as possible. Theoretically it should satisfy the conservation of energy laws as well as the momentum.

3.2.2.1 Verlet Algorithm:

There are several integration algorithms available Verlet Algorithm being the most widely used and yet the simplest one. In Verlet Algorithm, like all other algorithms, position, velocity and acceleration are represented in form of a Taylor series expansion such that:

$$r(t+\Delta t) = r(t) + v(t)\delta t + \frac{1}{2}a(t)\delta t^2 + \frac{1}{6}b(t)\delta t^3 \ldots. \quad (3\text{-}33)$$

$$v(t+\Delta t) = v(t) + a(t)\delta t + \frac{1}{2}b(t)\delta t^2 + \frac{1}{6}c(t)\delta t^3 \ldots \quad (3\text{-}34)$$

$$a(t+\Delta t) = a(t) + b(t)\delta t + \frac{1}{2}c(t)\delta t^2 + \frac{1}{6}d(t)\delta t^3 \ldots \quad (3\text{-}35)$$

Using finite differencing numerical methods one can reproduce the following:

$$r(t+\Delta t) = r(t) + v(t)\delta t + \frac{1}{2}a(t)\delta t^2 + \frac{1}{6}b(t)\delta t^3 \ldots. \quad (3\text{-}36)$$

$$r(t-\Delta t) = r(t) - v(t)\delta t + \frac{1}{2}a(t)\delta t^2 - \frac{1}{6}b(t)\delta t^3 \ldots. \quad (3\text{-}37)$$

The two equations above yield the position expression for the next time step $r(t+\Delta t)$ when summed, where velocity term is eliminated as:

$$r(t+\Delta t) = 2r(t) - r(t-\Delta t) + a(t)\delta t^2 + \frac{1}{6}e(t)\delta t^4 \ldots. \quad (3\text{-}38)$$

where the position at the next time step is given in the form of the current position and the acceleration with the error degree of δt^4. Subtracting Eq. (3-37) from Eq. (3-36) gives the velocity which is used for kinetic energy evaluations:

$$v(t) = \frac{r(t+\Delta t) - r(t+\Delta t)}{2\delta t} \quad (3\text{-}39)$$

In Verlet algorithm derived above, position is defined using the position and the acceleration of the current time and the position of the previous time step (see Eq. (3-38)) without

any use of velocity data. This algorithm is the modest in terms of computing storage space required and is straightforward. The weakness of the method arises at its accuracy which is moderate.

3.2.2.2 Velocity Verlet Algorithm:

This is an improved form of the Verlet algorithm where it stores the current position, velocity and acceleration and minimizes the round-off error.

$$r(t + \Delta t) = r(t) + v(t)\delta t + \frac{1}{2}a(t)\delta t^2 \quad (3\text{-}40)$$

$$v(t + \Delta t) = v(t) + \frac{1}{2}\delta t[a(t) + a(t + \Delta t)] \quad (3\text{-}41)$$

There are other integration algorithms (e.g. Beeman's, Leep-Frog, etc.] derived in a similar manner as described above which improve the precision at higher computational costs.

3.2.3 Interaction Models

Macroscopic state of a system can be defined in terms of the positions and the momenta of the particles that form the system. Total energy of a particular system with N particles can be represented by the Hamiltonian function, H, via summation of their potential and the kinetic energies, which are functions of coordinates and the momenta of the particles, respectively.

$$H\,(\boldsymbol{q}, \boldsymbol{p}) \;=\; V\,(\boldsymbol{q}) \;+ K\,(\boldsymbol{p}) \quad (3\text{-}42)$$

In the equation above $\boldsymbol{q}$ is the generalized coordinates for the position $\boldsymbol{r_i}$ of each individual atom or center of mass for molecules which are treated as single rigid particles and $\boldsymbol{p}$ is the set conjugate of momenta.

Kinetic energy term K, includes (x, y, z) components of the particle momentum .On the side, potential energy term V , contains interatomic or intermolecular information from which an

of motion can be obtained which dictates temporal evolution of the mechanical properties in the system.

For a basic system of N particles potential energy can be defined as sum of the individual contribution due to outer effects (first term in Eq.(3-43)) on each atom and contribution from pairwise interactions between neighboring atoms in terms of pairs, triplets, etc.

$$V = \sum_{i} v_1(\boldsymbol{r_i}) + \sum_{i}\sum_{j>i} v_2(\boldsymbol{r_i}, \boldsymbol{r_j}) + \sum_{i}\sum_{j>i}\sum_{k>j>i} v_3(\boldsymbol{r_i}, \boldsymbol{r_j}, \boldsymbol{r_k}) + \cdots \quad (3\text{-}43)$$

In the potential energy above, the second term is the pair summation and mostly reflects the system status, differing only around 10% from the computations including higher order interaction terms but saving in the computational time. In order to compensate this loss from the triple and higher order sets, an effective pair potential, v^{eff} is derived by fitting the pair potential results to the large experimental data used to generate the potential tables. These pair summations are computed in the nested loops, without counting the pairs twice. Assuming no external effects on the atoms, (which is the case for most studies) the first term vanishes and the second pair potential term, $v_2(\boldsymbol{r_i}, \boldsymbol{r_j})$, remains as the major contributor to the potential energy of the system. It is a function of the pair separation and pair potentials which are obtained from the experimental data in conjunction with the long-range theoretical calculations.

In MD simulations, like in all other computer simulations, the particle interaction models need to be well defined since they are the major criteria in computing the overall system properties. Interactions can be classified into two groups as intermolecular or interatomic interactions and intramolecular interactions. These interaction models define system energy depending on the interaction modes in the system which can be computed numerically in a reasonable time length. For discrete particles one can consider interaction modes like pair, coulomb or chemical interactions which contribute to the total energy. On the other side

molecules of two or more atoms can also affect the system energy due to the bond size and angle fluctuations.

In this study, systems considered contain atoms which chemically do not interact, and are single atom particles without any bond size or angle effects; therefore pair potential models which best describes such systems are discussed below.

3.2.3.1 Lennard-jones potentials

Lennard-jones potentials, which are extensively employed to compute the potentials for fluids and gases, describe the intermolecular potential energy at different separation distances of the particles due to the attraction and repulsion taking place between them (see Figure 3-4). Lennard-Jones potentials are given by the following:

$$V_{lj} = 4\epsilon\left[\left(\frac{\sigma}{r}\right)^{12} - \left(\frac{\sigma}{r}\right)^{6}\right] \tag{3-44}$$

In this equation, $\boldsymbol{\epsilon}$ is the well depth and shows the strength of the attraction between particles, $\boldsymbol{\sigma}$ is the distance where the interaction potential becomes zero, (it also shows the limit how close two particles get to each other) and r is the distance between two particles. The first term in brackets gives the repulsive potentials and the other generates the attractive interaction energy contribution.

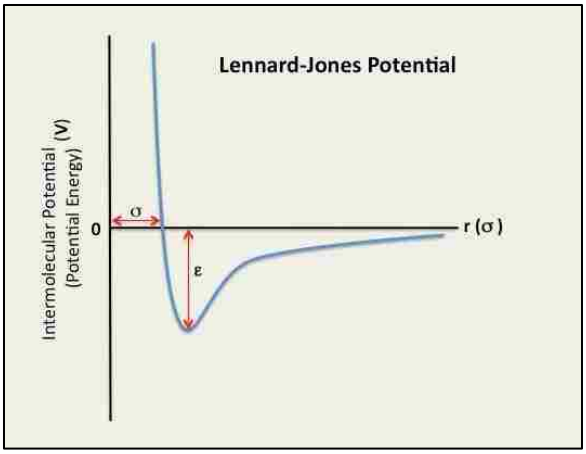

Figure 3-4 Schematic representation of a Lennard-Jones Potential

As seen in Figure 3-4 as particles get closer from infinity of no interaction, (zero potential) attraction increases and reaches to a maximum ($-\epsilon$) due to cohesive interactions which is the minimum at the well. Repulsion dominates the interaction potentials and a speed increase is observed in potential energy (positive potentials indicate repulsive interactions) for further reduction in the distance as a result of the non-bonded electron overlapping.

There are two main stages to build a well performing pair potential. First step is making a reasonable guess using the available energy and length parameters from relevant simulation studies done for the identical atom pairs. Next, ϵ and σ values are adjusted accordingly such that they yield the closest fit with the experimental data.

3.2.3.2 Embedded Atom Method (EAM) Potentials

Embedded atom method (EAM) is a pair potential which is, so far, the most appropriate potential used to calculate the total energy of metallic systems of pure metals or their alloys. It is also widely used for systems of large unit cells. EAM is especially powerful in producing more

realistic results at comparable simulation times for metallic cohesion problems, point defects simulations, epitaxial growth processes, grain boundary energy calculations, film growth processes, melting and alloying problems. (Ref. in [48].)

It was first developed by Daw and Baskes, where they defined the energy for each atom as the energy required for embedding that particular atom into its specific position in the system. The important point here is that energy required varies depending on the local electron density provided by the other atoms in the system [49]. Local electron density in metals can be obtained easily by superposition of the contributions from individual atoms in the neighborhood added to the density of the atom itself. As an addition to the embedding energy Daw et al. have also included the energy contribution from the electrostatic interaction of pairs while formulating the total system energy given below.

$$E_{tot} = \sum_{i} F_i(\rho_{h,i}) + \frac{1}{2}\sum_{i}\sum_{j\neq i} \emptyset_{i,j}(R_{i,j}) \tag{3-45}$$

This is the EAM functional for the total system energy which has the embedding energy F_i, the first summation term on the right above, as a function of the local electron density $\rho_{h,i}$ which is the sum of all electron density contribution from surrounding atoms. The second summation is the energy due to the pair repulsive forces between each atom pair where $\emptyset_{i,j}$ is the repulsive force between cores of atom i and atom j, at a distance $R_{i,j}$ from each other.

There are three parameters which must be in hand to be able to use Eq. (3-45) for energy calculations. They are embedding function F_i, electron density $\rho_{h,i}$ and lastly the pair repulsion function $\emptyset_{i,j}$. Foiles et al. determined a consistent set of embedding functions and pair functions in their work [49]**.** They obtained the functions for the FCC metals Cu, Ag, Ni, Pd, and Pt and their alloys empirically by fitting to the known bulk properties, particularly to sublimation energy, lattice constant, elastic constants, vacancy formation energy and the internal energy for

the FCC metals. For the embedding energy, it was considered to have zero energy at zero density and negative slope and positive curvature for the background electron densities of metals, during the fitting process (See Figure 3-5 left). The pair interaction term is purely repulsive and for alloys it was approximated as the geometric mean of the pure metals' pair interaction forces (see Figure 3-5 right). Lastly for the electron densities they used the Hartree-Fock calculations in their work.

As they have mentioned in their work, this method is also an approximation which was adjusted to yield the best result but at computationally reasonable and experimentally feasible way. Results can be improved towards accuracy by having more experimental data available for the fitting and including more system parameters which were omitted for simplicity. However, the validity of the functions has been tested for various bulk and surface properties and generally a good agreement has been observed.

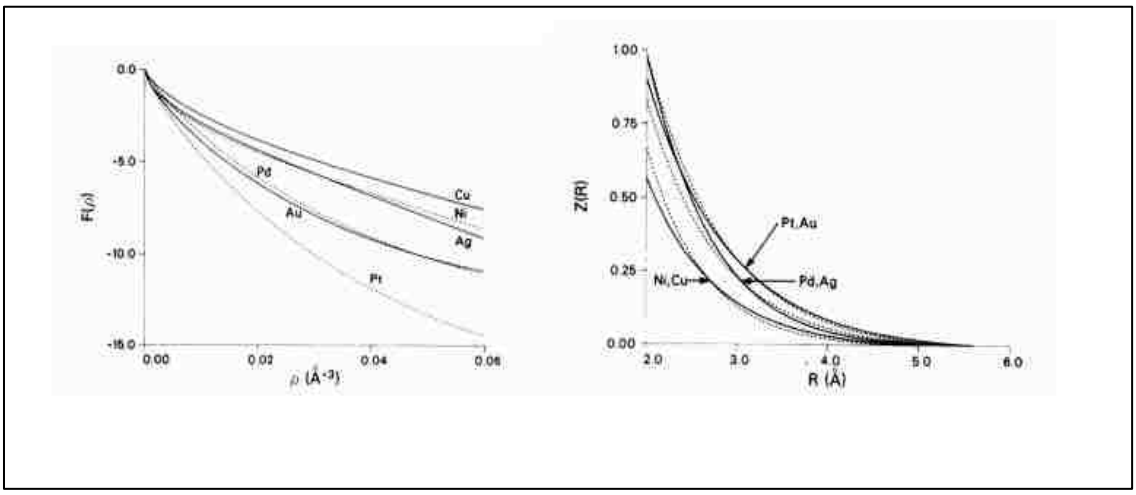

Figure 3-5 For metals Cu, Ag, Au, Ni, Pd and Pt; (left) the embedding function F (ρ) in eV is given as a function of electron density and (right) the effective charge Z(R) in units of electron charge which is used in calculation of the pair repulsive force is given [49]

3.3 Computational Issues

Computation time and the storage space required for simulations is the main concern for a feasible MD simulation. In a pair interaction involved MD simulation of N many particles, the computing speed is proportional to N^2. Therefore it is important to have a well-defined system size which is enough to represent the macroscopic system properties. Due to the computing resource limitation smaller systems are preferred. Surface atoms will not be behaving as they would in the bulk, which is a major concern for small models where atoms at the boundaries (outer surfaces) count almost half of the atoms in the system. So the computations will not yield pure bulk interaction scheme. This was overcome by introducing periodic boundaries to the system so that the model is identically replicated in all three dimensions.

In periodic boundary condition, a particle leaving the simulation box boundary at one direction enters the adjacent box from the opposite direction. All this in and out operations can be simulated in a single simulation box of periodic boundaries (see Figure 3-6)

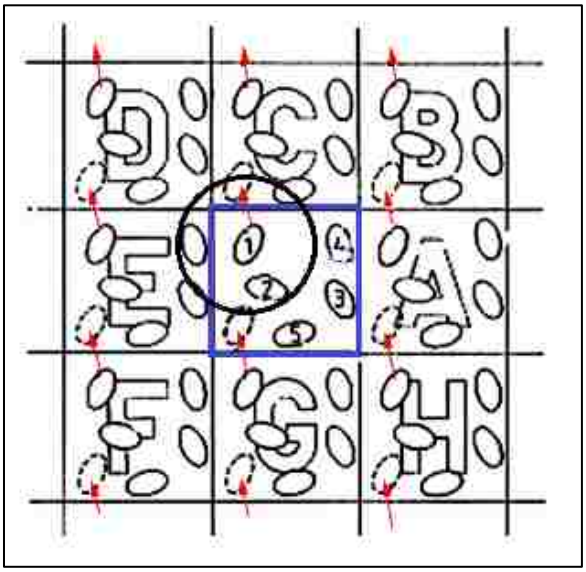

Figure 3-6 A schematic showing Periodic boundary motion and cut off radius. [47]

A 2D representation for the periodic boundaries is given in Figure 3-6 above, where the square box in the middle is the simulation region which is surrounded in all directions with identical boxes. Particle 1, moves into the upper box C leaving the simulation box where the corresponding particle in box G simultaneously enters the simulation box at the bottom. Thus, simulating the entire periodic system become equivalent to simulating the central box where only particles in that box are taken into account for computations. For instance, in the case of leaving the boundary in positive Y direction as shown above for particle 1, box size in the same direction is subtracted from the y coordinate of particle 1 and the coordinates for the particle at the bottom is obtained (same is done for the x and z coordinates) . This approach saves a significant amount of computation time and space while providing better bulk property results.

Another constraint in computer simulations is the number of particles in the simulation box. Although the periodic boundary approach saves time and space, the pair calculation for N number of atoms in the simulation box can be challenging. Similar to the truncation done in the potential energy calculation for the triple and higher interactions in Eq. (3-43), knowing that the largest contribution to the pair interactions are due to the atoms, a spherical cutoff (see Figure 3-7) region is defined for the particles interacting where only the particles in the cutoff limit are counted for pair calculations, assuming V=0 at $R>R_{cutoff}$. This truncation will result in loss in the accuracy of the calculation due to the omitted pair contributions. The cut off distance R_{cutoff} should not be greater than half of the simulation box length L. For the sample configuration given in Figure 3-7 below, particle 1 will interact with particle 2 in the same simulation box, and the particle which is the particle corresponding particle 4 in the duplicated box on left of the simulation box.

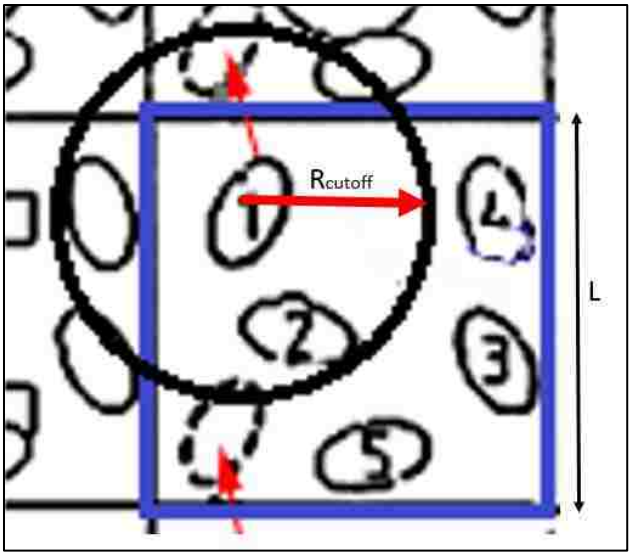

Figure 3-7 Spherical cutoff applied for the simulation box of size L with periodic boundary conditions.

There are numerous molecular dynamics simulation tools available most of which are free open source codes while some are commercial. There are codes specific to certain applications like Abalone and CHARMM which are developed for biomolecular simulations while CHEMKIN is for chemical reaction kinetics studies. In this study Large-scale Atomic/Molecular Massively Parallel Simulator (LAMMPS) was used as the MD code which is an open source code developed and distributed by Sandia National Laboratories in US. It computes interaction energy and forces between atoms, using appropriate interaction style functions (or functionals) and potentials which are available for solid state materials (metals, semiconductors) biomolecules, polymers and also for coarse-grained or meso-scale structures. Therefore, it can be utilized as a parallel particle simulator at the atomic, meso, or even continuum scale. [47]

3.4 Microscopic Stress

Definition of microscopic stress, which is a continuum quantity, has still been a debate since continuum concepts do not apply directly to discrete particles in atomic level simulations. However, it is a unique measure to understand the state of the simulated model in terms of its mechanical properties.

Studies on understanding the stress phenomenon at atomic level date back to Cauchy's stress definition for a crystalline solid. He proposed stress as being the force per unit area carried by the bonds crossing a given surface. Following his work, in order to interpret microscopic stress in a discrete system, Clausius and Maxwell, defined the "virial stress", which was the first attempt to define a tensor stress quantity both including the kinetic terms in addition to Cauchy's approach. This definition of virial stress is widely used in atomistic simulation due to its simplicity and computational advantages.

Similar to Cauchy's explanation for stress as the force being transferred across a boundary, Irwin-Kirkwood-Noll procedure also defines the stress or pressure as the force (or momentum) transfer via particles crossing a boundary (see Figure 3-8), where along with transferring actual particle momentum, interaction between atoms on opposite sides of the boundary also contributes to the total momentum transferred (see Eq.(3-46))

$$\mathrm{P} = \frac{F}{Area} = \frac{1}{Area}\frac{d(mv)}{dt} = \frac{1}{Area}\frac{dp}{dt} \tag{3-46}$$

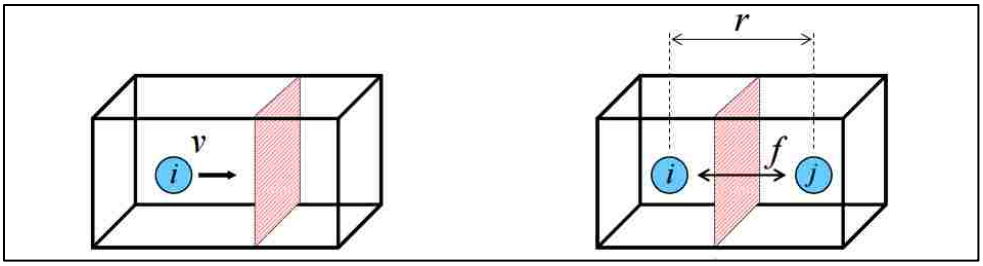

Figure 3-8 Force (momentum) transfer per unit area across a boundary in a closed volume (box) can originate from two mechanisms: particle motion across the boundary (left), force interactions between atoms on opposite sides of the boundary (right) [46].

In their fundamental work Irving-Kirkwood [50], proposed a stress tensor derivation in terms of molecular variables using the statistical mechanics approach where they used Dirac delta functions to define the pointwise stress. For the macroscopic stress they used spatial averaging over a domain which needs to be sufficiently large in microscopic scale. Noll developed their work by dropping the Dirac delta function and eliminating the infinite series expansion which is replaced with a closed integral expression giving its final form [51]. Other atomistic stress formulations are based on this definition with certain modifications in order to improve the computations. Virial stress σ_v can be derived from the Irving-Kirkwood expression by elimination of the all higher order terms due to expansion of Dirac-delta differences and selecting the averaging domain as the volume around the point of interest $\Omega(x)$. It is given as follows:

$$\sigma_v = -\frac{1}{\Omega(x)}\left[\sum_{i=1}^{N} m_i \boldsymbol{u_i} \otimes \boldsymbol{u_i} + \frac{1}{2}\sum_{i,j=1,i\neq j}^{N} \boldsymbol{f_{ij}} \otimes \boldsymbol{r_{ij}}\right] \tag{3-47}$$

This is the simplified version of the virial expression given in the study by Ulz et al. where they included forces due to triple and higher number of atomic interactions in their equation Eq.(1) in [52]. Here, m_i is the mass of atom I, and $\boldsymbol{u_i}$ is the relative velocity with respect

to the mean velocity of the N particle system, $\boldsymbol{f_{ij}}$ is the force on atom i exerted by atom j and $\boldsymbol{r_{ij}}$ is the position vector between two atoms, which is $r_i - r_j$ (see Figure 3-9).

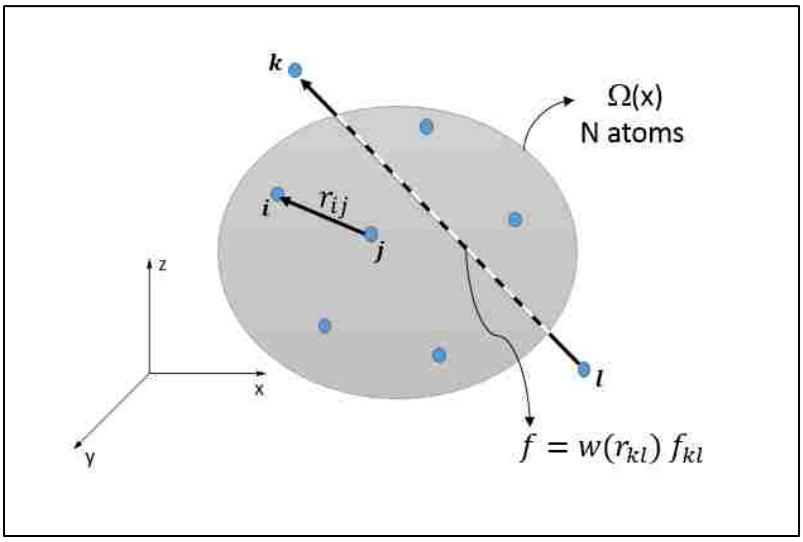

Figure 3-9 Schematic representation of the virial stress averaging domain volume $\Omega(x)$ consisting of N atoms and the weight function $w(r_{kl})$ by which the partial effects of the atoms outside the domain are included in Hardy stress definition.

Hardy stress is another method for atomistic stress calculation which incorporates the partial effect of the atoms that are out of the averaging space but interactions that take place through the space as illustrated in Figure 3-9 above for atoms k and l. In this method, a weight function, $w(r_{kl})$ in Figure 3-9, is introduced to the virial stress definition such that the contribution of forces which pass through the domain are also included in the sum in the amount proportional to the length segment (dashed line between atoms k and l in Schematic representation of the virial stress averaging domain volume Ωx consisting of N atoms and the weight function $w(r_{kl})$ by which the partial effects of the atoms outside the domain are included in Hardy stress definition) crossing through the averaging volume.

It can be concluded from the two definitions above that virial stress is the form of Hardy stress with a uniform weight function neglecting the atoms outside the domain. Similarly it can be seen that both identical in the thermodynamic limit where the volume $\Omega(x)$ goes to infinity including all atoms in the system since the weight function will converge to unity.

In general, Hardy stress is more accurate and converges faster in the averaging domain. The error that virial stress expression yields is mostly due to the surface atoms of the averaging domain since virial method does not consider the interactions between the surface atoms and the neighboring atoms outside the averaging volume. This error can be minimized if the surface to volume ratio is reduced. Provided that a reasonable domain size is defined, it was reported that virial stress interprets the surface contributions better from a physical point of view**.** [53]

Virial method is used in most of the MD simulations tools (including LAMMPS in this study) due to its simplicity and low computational costs although being less accurate and converging slowly in the domain [51]**.** However, it has been shown that for most situations of non-zero deformations of finite temperature, Hardy stress definition resulted in better estimates than the Virial stress [54].

Additionally, in a recent study, virial stress was reported to be out of equilibrium in the vicinity of a defect [55]. But it was also stated in the same study that the virial results are qualitatively consistent with the macroscopic stress phenomena and thus can be used for visualization purposes for defect simulations.

In this work, MD simulation tool LAMMPS, computes energy term (the term in the square brackets in Eq. (3.47) above) and leaves the averaging volume selection to the user where the definition may vary at the surface, around a defect or in the bulk, etc. It has been shown that the selection may affect the stress results significantly around such defect zones where high stress gradients are likely to occur [56] .

Chapter 4 Literature Survey

This section begins with the review of the previous works relevant to the general stress behavior during different stages of the thin film growth process. There are different mechanisms and conditions that play a considerable role on the stress behavior before, during, and after the film deposition process. These factors can act as a combination and their resulting affect can be superimposed [10], [30].

Subsequently, more specific studies related to major mechanisms and conditions which are known to be responsible for the stress and morphology evolution of the films being deposited will be discussed.

4.1 Stress Behavior during Pre-Coalescence Period

Absorption of film atoms at the substrate's surface changes the free energy distribution on the surface, thus changing the surface stress. For solid particles at equilibrium there is a balance between surface and the volume stresses. This balance brings into a pressure difference called Laplace Pressure given as

$$\Delta P = P_s - P_v = \frac{2f}{r} \tag{4-1}$$

where f is the surface stress. This expression can be modified for thin discs of radius relatively much larger than the thickness and it yields a radial pressure of 2f/h. This quantity acts like a hydrostatic pressure on the small island formations which results in compression [23], [42], [57].

One other mechanism inducing compressive stress is the lattice mismatch which yields the stress called misfit stress [32]. Surface stress arises due to the bulk atoms exerting a compressive stress to the deposited film layer atoms for being in different atomic registry. This mechanism is more clearly observed between a substrate and an overlaying film material. Both film and the substrate atoms have different lattice constant in their bulk forms .When deposition starts, nucleated small islands rigidly attaches to the substrate surface but as deposition continues added atoms will tend to increase the island size, while the substrate island interface will force in opposite in order to keep the original lattice size. This will result in compression on those small islands prior to coalescence [3], [23], [29], [58]. The critical size for the initial islands after which substrate start applying traction on them has also been studied [59]. This is strongly related to the bonding between the film and the substrate. Stronger bonding yields lower critical size and higher compressive stress generation [60]. These capillarity mechanisms mentioned above are commonly accepted as the major contributors to the compressive stress in pre-coalescence regime [58].

For the compressive stress it has been also suggested that the adatoms moving around the surface and interfaces of the film–substrate system act like effective force dipoles which cause compressive stress [61], [62].

4.2 Stress Behavior during Coalescence Period

It has been verified in many studies that tensile stress is observed at this stage of film formation (e.g. Figure 1-3). The major change that takes place during this period is the impinging of initially nucleated islands on each other and closing of the channels by formation of grain boundaries and also by the addition of new atoms from the ongoing deposition process [14], [42].

In order to explain the generation of tensile stress several models have been proposed. Hoffman taking into the grain boundary formation into consideration proposed a model where he attributes the tensile stress formation to the interchange between elastic energy and surface energy [62], [63]. He states that coalescence can take place if the elastic energy produced after the stretching of discrete islands to form grain boundaries is less than the loss of surface energy when grain boundaries are formed.

$$\frac{w^2}{2L}\bar{E} \leq 2\gamma_s - \gamma_i \qquad (4\text{-}2)$$

where left side is the strain energy resulting from the closing of a gap of width w between LxL sized islands (See Figure 4-1), and the right size is the surface energy lost form two island walls minus the gain from the single grain boundary interface. [42], [62].

This method assumes block coalescence where the islands snap at once by sliding on the substrate when they overcome the surface energy barier [42]. But Hoffman did not consider the flux and the mass transport.

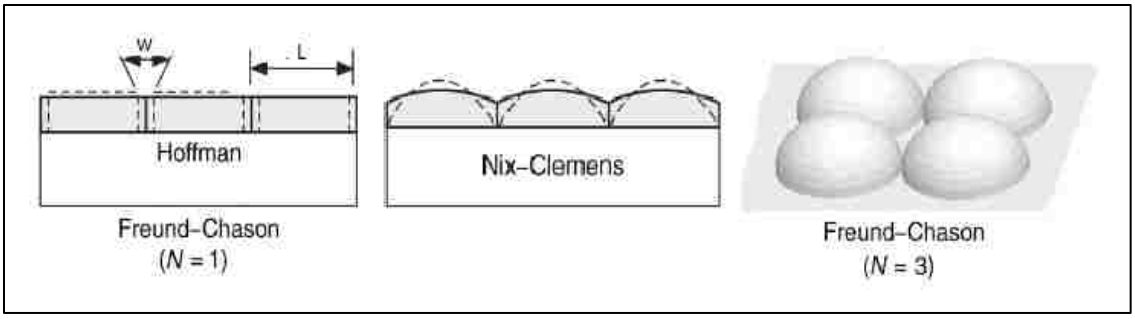

Figure 4-1 Models proposed for the generation of tensile stress during coalescence of islands

Nix and Clemens proposed the "crack closing by zipping" model where the gap is treated as a crack which starts closing at the bottom and keeps closing as long as the elastic energy increase is less than the loss in surface energy [42], [62], [64]. Their results overestimates the stress between islands.

Freund and Chason considered the overestimated stress values in Nix Clemens results [65] and developed the idea of "zipping" by considering the cohesive attraction taking place in between the islands and predicted better results in consistence with Hoffman's model for N=1 case [42]. Rajamani et al. and Hearne et al. showed in their FEM work that most of the tensile stress occurred after the initial coalescence in contrast to Nix-Clemens model where they attributte the tensile stress only to the initial coalescence [10], [66], [67].

All these models ignored the effects of mass trasportation taking place which highly effects the stress behaviour during and after deposition [42], [64]. Seel et al. using embedded atom interatomic potentials (EAM) in their molecular dynamics simulations, showed that approaches mentioned above overestimates the coalescence stress [15]. According to their study, spontaneous coalescence can take place at termodynamically favored cases, otherwise kinematic barries prevent this type of closure [15].

Seel and Thompson included the deposition flux in their studies [14]. They have considered the case of sliding and traction of islands in their 2D finite element model. Islands can slide at low coverage periods and this results a mean stress which is compressive, however, when coverage reaches a limit where sliding is constrained by other islands, coalesence leads high tensile stress generation.

Tello et al. also developed a continum model utilizing the cohesive zone law to define the coalescence. Cohesive zone law expresses the traction at a certain point on the grain boundary (GB) or the surface as a function of the gap size [43], [62]. They could also generate the deformed shaped of the coalescing islands and were able to explain the effect of deposition flux and diffusivity on stress generation. (See Sections 4.4.2 and 4.4.3)

Models developed to explain the coalescence process alwasys encountred the challenge of stochastic island nucleation and coalescence taking place at different instances and random locations. Bhandari et al. has approached this problem from the otherway. They used Au covered and lithography patterned Si layers as the conductive substrate surfaces in order to control the island nucleation locations and sizes and rates. They could achieve similar basic growth mode models as mentioned above in the simulation and verified that the the major tensile stress generation occurs after the initial coalesnce.They carried out the reaserch for the post coalescence period and found that tensile stress reaches a steady state value for higher growth levels depending on the deposition rate [67].

4.3 Stress Behavior in Post-Coalescence and Steady State Period

This period is where the coalescence events are mostly completed and a full monolayer is almost formed. Thickness increases as deposition continues. Various relaxation mechanisms (e.g. GB diffusion, recrystallization, etc.) are active and modify the stress and restructure the morphology both during and after the deposition till equilibrium is achieved. The defects, voids etc. are eliminated during the steady state period depending on the mobility of the film material and environmental conditions [1], [26].

Incremental stress, (the stress evolved due to the new atom incorporation to the system) is observed to change from tensile to compressive after the film completes the coalescence and forms continuous layers. In Equation (4-3), first term is the incremental stress and with the assumption that the average stress in the film is constant in time it modifies into:

$$\sigma(h_f) \sim \frac{\frac{\partial \kappa}{\partial t}}{\frac{\partial h_f}{\partial t}} = \frac{d\kappa}{dh} \tag{4-3}$$

where stress is related to the slope of curvature-thickness curve [26]. As shown by the dashed lines on the curve in the figure below (see Figure 4-2) it can been seen that initially the slope is negative then becomes positive and increases till it reaches a peak corresponding to the end of the coalescence period. After that instance slope changes to negative indicating addition of compressive stress as deposition continues. This is the surface stress producing net compression after coalescence [42].

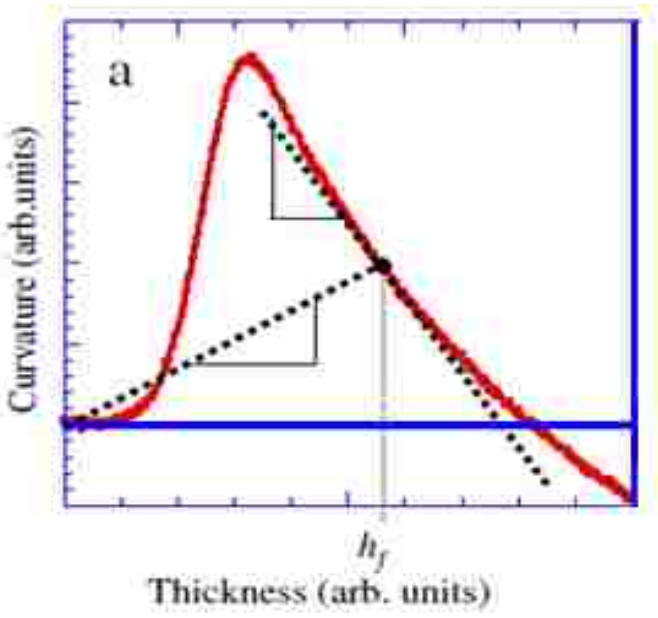

Figure 4-2 Evolution of curvature during a) growth of evaporated Ag on SiO2 at RT [42]

For most metals which display high mobility it is observed that they built compressive stress after full film layer is formed. Mobility of atoms provides relaxation of tensile stress inherited from coalescence step. This relaxation is due to the insertion of atoms into grain boundaries which generates compressive stress [3], [19], [68]–[70]. Chemical potential increased at the surface and surface becomes super saturated during the deposition flux (see Figure 4-3). This is proposed to be the driving force for atom insertion into the grain boundaries where the potential is lower [41], [68]–[71].

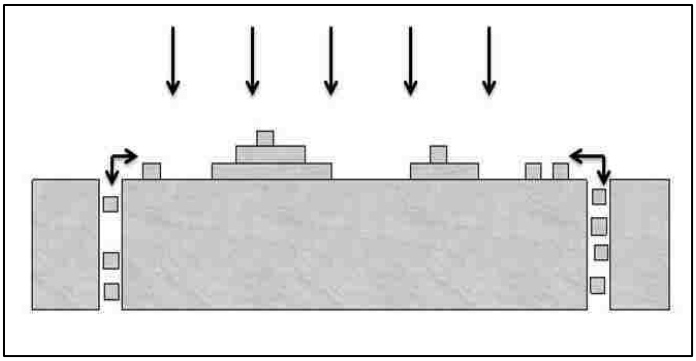

Figure 4-3 Schematic representation of reversible GB insertion of atoms under deposition flux [42].

The reversible effect of chemical potential on the GB diffusion was also verified experimentally. Stress evolution was observed to change from compressive to tensile when deposition was interrupted, but as deposition is resumed stress levels attain the previous conditions which indicates the validity of this mechanism (See Figure 4-4) [26], [29], [30], [71], [72]. Similar reversible stress changes were reported for the pre-coalescence regime as well [61].

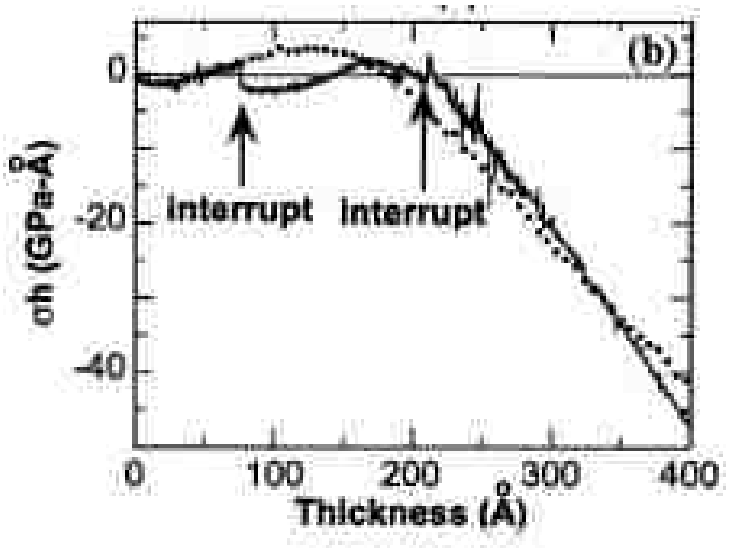

Figure 4-4 Stress thickness vs thickness curves showing growth interrupt behavior for *a*-Ge grown at 270 °C. The solid line is for growth with interrupts, while the dots are uninterrupted growth data [30].

There was reported a nice experiment which shows the role that GBs play in the stress evolution. It was observed that Pd films deposited on polycrystalline Pt grew compressive stress, while deposited on monocrystalline Pt resulted tensile stress [71].Effect of atoms insertion into GBs on compressive stress formation was also verified with a different experimental method. They utilized electro-deposition followed by etching at the same rate. Etching process which acts as negative growth reverses the surface chemical potential, where surface becomes lower in potential. As a result, atoms diffuse back to the surface leading relaxation in the compressive stress [26].

In a recent study, the effect of bombardment of film surface with energetic atoms was also shown to induce GB insertion, due to the momentum transfer to the surface atoms close to the impact site [73], [74].

The density of adatoms incorporated to the GB was demonstrated to be in an inverse linear relation with the stress-thickness value of the film [19].

Effects of the surface chemistry on post coalescence stress evolution have been studied by Qi et al. They showed that hydrogen concentration is increased at lower temperatures and this yielded grain boundary widening leading compressive stress increase by insertion of more atoms into the grain boundary. This result is surprising since it was common that for most low mobility materials tensile stress would occur [41]. As a continuation of this study, Yang et al. [75] used Kinetic Monte Carlo simulations to simulate the effect of a surfactant added on the surface of Cu (111) film surface and continued deposition process. The results showed that inclusion of surfactants lowered adatom insertion to the GBs and thus less compressive stress was observed. Utilization of surfactants or other impurities was proposed as a method that can used in controlling the stress state [27].

Sheldon et al. [76] has applied cohesive zone law to describe the tensile stress evolution in the post coalescence film growth period (See Figure 4-5).This is explained as a result of epitaxial templating imposed by the lower film atoms over the new layer atoms being deposited. They found that maximum tensile stress can reach up to fracture limit and is independent of the growth rate. In their study they have also concluded that sharper cusps at the grain boundaries lowered the steady state tensile stress in the film.

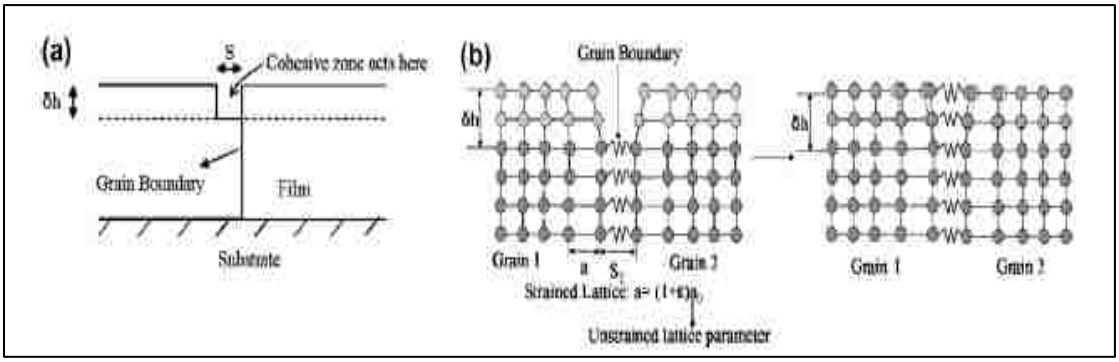

Figure 4-5 a) Cohesive zone applied (a) Schematic of grain boundary formation with a layer of thickness dh, where the cohesive attraction across the distance S creates a new segment of grain boundary; (b) epitaxial templating during the growth of a polycrystalline film [76].

In steady state where film gets thicker the incremental stress mentioned above becomes constant. Experiments showed that although initially stress is compressive in post coalescence regime, it turns into tensile at large thicknesses [77]. Chason developed a kinetic model and verified the thickness dependence to be consistent with the pervious experimental results [78]. He also included his results in his recent review paper where he demonstrated that the steady state stress depends on the D/RL dimensionless parameter where D is the diffusivity, R is the deposition rate and L is the grain size [26], [78]. Therefore similar conditions could be achieved by manipulating D, L, and R parameters for different trials. For high D/RL (high diffusivity, low deposition rate) there is compression since atoms can freely diffuse before the arrival of the next depositing atoms to the surface due to the low rate. It is the opposite for low D/RL values where

atoms tend to stick where they first hit before being diffused into the grain boundaries and other surface defects due to low diffusivity and high rate. This results in less compression or increased tension in the film. For the third parameter (L) they showed that there was a cross-over relation between the grain size (L) and the stress evolution (see Figure 4-6).General intention was that there would be higher tensile stress generation for finer grained structures for having more grain boundaries having formed which still holds for higher deposition rates (R). But smaller grains also provide more grain boundaries for the adatoms to be inserted into which is the case at lower deposition rates where compressive stress is enhanced.

The competition between the tensile stress and the compressive stress generation was studied very recently by Gonzalez et al. [79] where they proposed "inside bundling-outside grooving" model for grains of different sizes formed after coalescence. This was a more realistic approach since they considered the interaction between different sized grains. Their model showed compressive stress at deep grain boundary regions and tensile stress at the shallow regions close to the surface. In other words; gap regions above the grain junction are under cohesion forces whereas the buried regions below the junction experience shear loads.

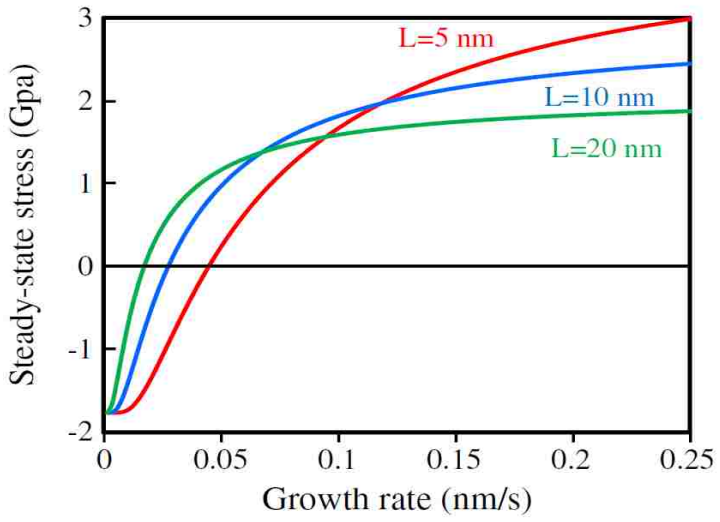

Figure 4-6 Model calculations of steady-state film stress vs growth rate for different values of the grain size (L=5, 10 and 20 nm) [26].

4.4 Factors Affecting the Stress Behavior in Thin Films

4.4.1 Temperature

Temperature is a major parameter in film deposition that has superior effects on mobility and diffusivity and therefore directly effects the resulting stress and morphology evolution in thin films [3], [14], [27], [80]. Thermal energy helps to overcome the energetic barriers during coalescence of islands or grain growth periods [15].

Seel et al. have found that the maximum tensile stress value decreased when temperature was increased. This was because of the enhanced diffusivity which works as a relaxation agent. Temperature also affected the grain size making them larger for enhanced grain growth at higher temperatures. Stress relaxation rate was shown to decrease with temperature increase which points out the dependence of the relaxation mechanism to the film thickness [14]. Similar results were obtained in amorphous Al deposition over Si [81].

Mobility could be discussed under a separate section but since it is closely related to the temperature it is included in here. Metals with low melting points (e.g. FCC metals Al, Au, Ag etc.) have high mobility and can show characteristic C-T-C VW type of film growth at elevated temperatures. But refractory metals are low mobility materials which require very high energetic conditions to be able to diffuse into the grain boundary or on the substrate surface. It is the homologous temperature ($T_{hom=}T_{deposiston}/T_{melting}$), the non-dimensional temperature parameter, taken into account in experimental data analysis. At low homologous temperatures, films cannot relax the tensile stress generated during coalescence and they develop more tension as deposition continues. During interruptions they cannot even relax the accumulated tension [22], [29], [43], [69], [80]. At lower T_{hom} a transition from 3D to 2D growth mode is observed [27].

Morphology of the grains in the films also varies depending on the temperature values and the material properties. Stress zone models have been defined for different morphologies [1], [80]. Refractory metals deposited at around 0.2-0.3 Tm (melting temperature in K) display a formation of Zone T and when temperature is increased above the melting point Zone II structures are observed. For T_{hom}> 0.2—0.3, FCC metals tend to display Zone II type of morphologies [80]. At low temperatures where the diffusion is very low, atoms stick to where they first hit, thus a porous type of film forms with low densities [16]. As the temperature is increased atoms can diffuse to fill in these pores and diffusion within the grains yields columnar type growth of type Zone-Ic. For relatively higher temperatures grain boundary diffusion barrier is also suppressed leading to a growth type of Zone-T. The buried grains will not be able to re-grow due to the immobility of the grain boundaries and they will remain as small grains, but grains above in the direction of the favored growth will overgrow other grains, forming the faceted structure as seen on Zone T [1].

Deposition temperature effects the preferred orientation of the film atoms. Abadias et al. observed in their experimental studies that Ti atoms change from (111) to (002) orientation when temperature is increased from RT to 300^{o}C [36].

Temperature effects have been also studied for nanocrystalline diamond films. The intrinsic stress was shown to drop from tensile to compressive as the temperature decreases where it became zero at around 700^{o}C. Achieving a zero stress at elevated temperatures was an important result for critical applications [33].

4.4.2 Diffusivity

Diffusion of surface atoms or deposited atoms into the grain boundary has been commonly accepted as a major mechanism responsible for the compressive stress generation in thin films. Molecular dynamics simulations [19], [70] and continuum level approaches both verifies this assumption and they also match well with experimental results [43], [62], [82].

Tello et al. considered the GB and the surfaces together in their continuum model study different than the other models where they treated them separately. They showed that diffusion was effected by the growth rate where high growth rate was reducing the range of diffusion and vice versa [43].

Grain boundary diffusion is also a stress relaxation mechanism. Ayas et al studied GB diffusion mechanism and found that when there was thermal stress available in columnar films, atoms were diffused into the GB forming wedges in order to relax the stress gradient at the GB [83]. It was also shown that GB diffusion was faster in slender columnar grains. For the case where traction was eliminated between the substrate and the film relaxation was faster [83], [84].

Effects of surface diffusivity have been analyzed in a recent paper which has shown the strong relation between the diffusivity and the film morphology. At high diffusivity columnar grain formation has been observed at Ag deposition on amorphous SiO_2. On the other side, Ag film deposited on amorphous Ge has been shown to have finer grained structures in contrary to the first case due to relatively lower diffusivity [29].

4.4.3 Deposition Rate

Deposition rate or growth flux is one of the major factors affecting the stress behavior in films during deposition. It has been shown that films grown at low deposition rates develop compressive stress. Depending on the rate of diffusion to the grain boundaries or to the surface, deposition rate alterations yield different results. When it is increased stress turns tensile for cases where the grain boundary deposition is equal or less than the surface diffusion [26], [35], [43], [62] (See Figure 4-7).

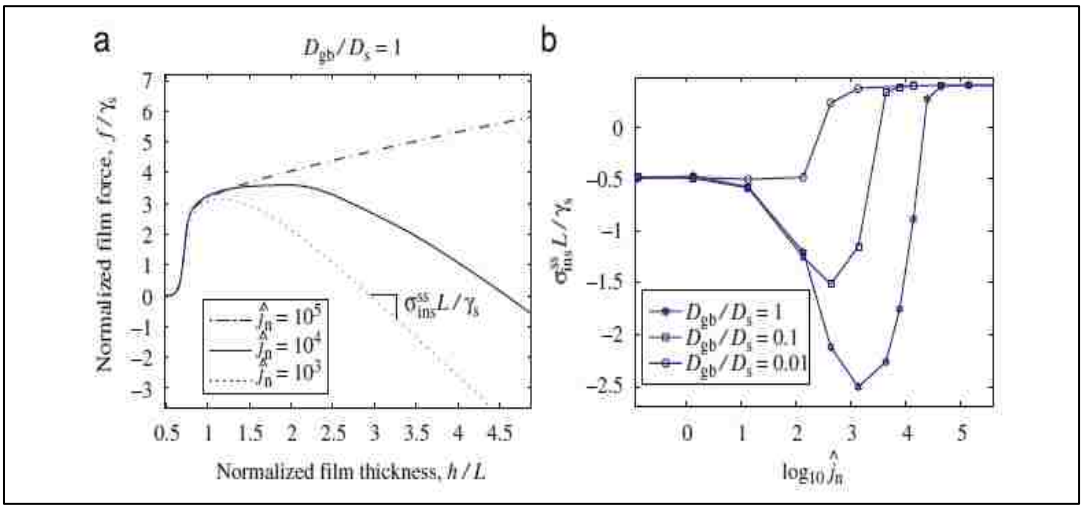

Figure 4-7 Representative behavior of normalized instantaneous stress with film thickness (left) and the variation in steady-state stress with growth flux and diffusivity ratio (right) [62].

High deposition rates results in incomplete bonding in the grain boundary, which explains well the tension observed [43]. More compression observed at lower rates is attributed to increased grain boundary diffusion since the atoms will have more time to diffuse before being distracted by the atoms being deposited [17], [67].

In experiments it is also shown that the reversible stress change would be more after the growth interruption if deposition rate is increased in the resumption period [61]. This is because of the increased chemical potential on the surface due to higher flux.

The effect of the deposition rate was studied experimentally by Vecchio and Spaepen on Cu and Ag films. They found in Cu films that increasing the rate did not affect the tensile maximum considerably, but there was a definite decrease in the compressive stress observed in the post coalescence period. Results were close for Ag, just the amount of decrease being less in compressive stress [31].

Deposition rate for alloy films play a crucial role in the morphology of the resulting film. Concentrated modulations (CMs) are observed (lateral or vertical) at different deposition rates under spinodal deposition. After repeated experiments, morphology maps have been established where slower rates leading to Vertical CMs, while faster rates lead to lateral as shown in Figure 4-8.

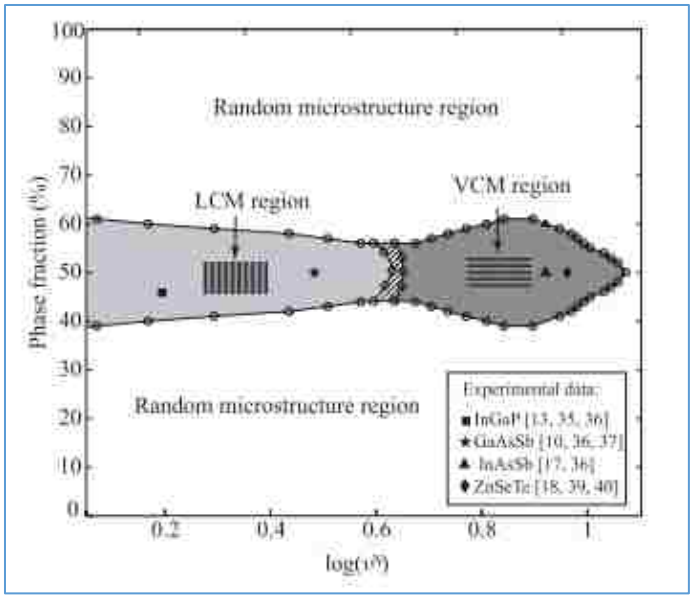

Figure 4-8 Phase diagram of morphological patterns, showing dependence on deposition rate (normalized) and alloy composition

4.4.4 Deposition Pressure

In order to investigate the role of pressure on film stress and morphology Pletea et al. conducted a series of experiments where they deposited Cu by sputtering on Si (001) at various pressures. They found that there was a transition from compressive to tensile stress as pressure increases. This was attributed to the increasing surface roughness and formation of less dense microstructures due to higher deposition pressure. It was seen that coalescence step was delayed to higher thicknesses, indicating formation of higher grains at higher pressures [34].

Low mobility materials deposited by thermal evaporation displays a tensile stress, while refractory metals of low mobility deposited by sputtering method which provides low Ar pressure and biased substrate grow compressive stress [27]. The compressive stress is attributed to the atomic peening process due to the scattered Ar atoms or sputtered atoms.

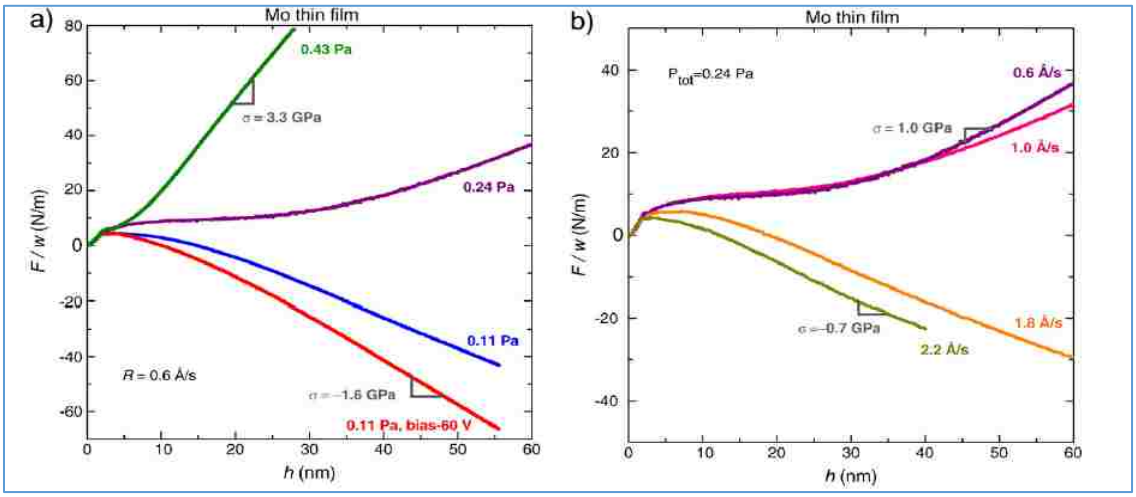

Figure 4-9 Force per unit width F/w versus thickness h during growth of pure Mo films on oxidized Si (a) at different Ar working pressures and constant deposition rate of 0.6 Å/s, (b) at various deposition rates and fixed pressure of 0.24 Pa [35].

Fillon et al. [35] also reported similar behavior in case of pressure increase during low-mobility Mo-Si alloy film deposition on Mo under-layer. In the same study deposition rate increase was found to lead increase in compressive stress where Chason [71] reported the opposite in his model (See Figure 4-9).

4.4.5 Grain Growth

Grain growth is a mechanism which causes tensile stress generation both during and after the coalescence periods. It is a coarsening process which increases the film density as film will tends to contract. This process will be prevented by the substrate traction leading tensile stress. It is the major mechanism responsible for the initial tensile stress generation in high mobility films at elevated temperatures. This mechanism also plays a stress relaxation role by either removal of the boundary segments formed by zipping or preferential growth seen at plastically soft grains [30], [42].

4.4.6 Surface Defects

Formation of defects is a stress relaxation mechanism which has been encountered in many experimental studies. This mechanism was studied using molecular dynamics modeling for Pd deposition on Au substrate and defects in form of stacking faults were observed to occur after 10 ML of deposition, relaxing the tensile stress accumulated [39].

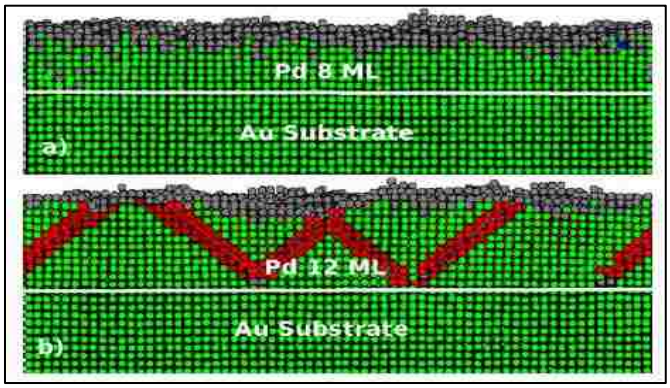

Figure 4-10 Defects in form of stacking faults after the 10^{th} ML deposition of Pd on Au (red slabs) [39].

Roughness can be in different forms such as surface terraces, vacancies, un-coalesced islands or adatoms bonded to the surface. The mechanisms behind roughening can be grain boundary crossing barriers, steering effects or low mobility behavior under high deposition flux [38].

Simulation results demonstrated that the defects decrease the tensile stress. This is estimated to be due to the reduction in contact area between the islands. Experimental studies also lead to the same conclusion [10], [34], [69], [85]. The presence of adatoms has little effect on the surface stress [69]. But when adatoms are injected to the terrace collectively forming a dislocation, they release the tensile stress at the terrace provided that this takes place away from the step edges of the terrace [86].

In a discussion made about the kinetic roughening which takes place at higher deposition rates it was said that this process could possibly carry the coalescence events to even post coalescence regimes due to the emerging island like roughness resulting decrease in compressive stress due to tensile stress generation [31], [77]. Kinetic roughening and surface flattening events are two processes which are of different origins (i.e. surface flux and surface diffusivity, respectively). Roughening enhances the tensile stress generation while flattening leads to compressive stress [1].

Chapter 5 Purpose of Research and Simulation Procedures

In this study, stress evolution phenomenon during FCC metal thin film deposition process, particularly at coalescence and post-coalescence stages, will be examined via atomic level MD simulations. Coalescence events between discrete growing structures (i.e. islands) cause dramatic changes in measured film stress, as reported in experimental studies. In many cases, stress curves display a significant tensile jump due to grain boundary formation and cohesive attraction during coalescence. Relaxation of the resulting tension and the distribution of the stress over the film depend on various parameters like the film material mobility, surface chemistry, or effects related to the size of the structures coalescing. Because coalescence plays such a significant role in determining overall film stress, simulations performed here are focused on this critical event in a relatively simplified geometry of adjacent monolayers coalescing to close an essentially linear gap between them. This approach is expected to help us explain how overall film stress values increase in tensile magnitude; more importantly, it will expand our understanding of how uniformly stress is distributed after coalescence events and, in turn, how this influences subsequent relaxation that takes place.

Depending on film and substrate materials, lattice mismatch may have significant influence. One limit that can be explored is for islands or films of a material on an underlying surface of identical material; such a limit is germane to late stage film growth. Even for early growth mechanisms, this limit can be explored as it possesses the advantage of eliminating effects due to lattice mismatch. Previously in our research group, coalescence of hemi-cylindrical Au islands on an epitaxially matched Au surface was explored. With the cylinder axis along a periodic dimension in y and the free surface direction along z, simulations explored coalescence

in the x direction under a plane strain condition. This geometry was adopted as it was in analogy to recent experiments; furthermore, the condition of plane strain simplified stress analysis [10], [87]. Simulations for the hemi-cylindrical geometry explored a single feature (i.e. island) size and examined stress upon initial island coalescence as well as with subsequent Au deposition on initially coalesced islands. It was demonstrated that specific stress evolution events could be connected with local atomic structural transitions. However, it was also found that, to more precisely examine stress distributions associated with film growth events like coalescence, more simplified geometries must be modeled.

This work will explore effects due to lattice mismatch by modeling Au thin films on Ni. In this study, Au and Ni, both FCC metals, were selected since they display significant lattice mismatch. Furthermore, EAM interaction potentials for this system already exist and they accurately describe many of the mechanical and thermodynamic properties of Au and Ni, both as pure individual species as well as the alloy system. For example, Table 1 shows a collection of property predictions by the model used here and a comparison to the same experimental values. As can be seen, very reasonable agreement exists for bulk properties tabulated; in most cases, this is because the potentials used here were fit to those tabulated bulk values (the exception is melting point T). Agreement with experiment for predicted energy of the low index surfaces (to which the model was not fit) is less satisfying; however, values are less than a factor of 2 off of experiment. Furthermore, energy of the low index surfaces orders properly when compared to *ab initio* quantum mechanical calculations and the difference between Au and Ni surface energies is comparable between model and experiment.

		Experimental		EAM	
		Au	Ni	Au	Ni
Equilibrium Lattice Const. (Å) (300 K)		4.078	3.52	4.078	3.52
Bulk Modulus (GPa)		180.3	180	178	181
Young's modulus (GPa)		78	200	78	217
Melting Point (K)		1337	1728	1281	1635
Mixing Enthalpies (eV)		0.28		0.30	
Lattice Structure		FCC		FCC	

Table 1 Mechanical and thermodynamic quantities of Au and Ni elements are compared for experimental and simulation values (Ref. in [49])

Most significantly for this research, it was desired to form a sharp interface between film and substrate. The heat of mixing for Ni and Au – both experimentally and in the model – is positive and relatively large; this imparts confidence that we can achieve the interface condition desired. While it is advantageous to have atomic force fields already available that possess reasonable accuracy compared to experiment, it is important to highlight that interests here are more generally around the notion of how stress evolution mechanisms in metallic films and structures spatially manifest stress (i.e. more or less uniformly) and how stress distributions evolve. Thus, interest is not so much in the Au/Ni system specifically; rather, this system possesses attributes that gave us confidence we could model dissimilar material growth scenarios with an atomically sharp interface.

Low-indexed Faces	Au	Ni
(111)	790	1450
(100)	918	1580
(110)	980	1730
Experimental (average face)	**1500**	**2380**

Table 2 Calculated surface energies of the low-index faces and the experimental average surface energy, in units of ergs/cm^2 [88].

In this regard, preliminary work that has been done before proceeding to coalescence simulations is summarized below. Note that both prior work [13] and our own simulations demonstrate surface alloying occurs when Ni is deposited on low index crystallographic surfaces of Au; the same occurs when Au is deposited on Ni (111). Surface alloying for immiscible metals has been demonstrated experimentally and may be well described by emerging complexion theory of interfacial phases [89], [90]. Given desire here to model a sharp material interface, such observations are of concern; however, for Au deposited on Ni (001) using the model here, deposited Au atoms adopt a purely over-layer structure. Thus, in this study Au monolayer coalescence on Ni (001) is modeled.

5.1 Preparation of Periodic Au Islands on Ni (001) Substrates

In preparation of the model, we start with building Ni (001) substrate of dimensions 3nm, 3nm and 20nm in x, y and z directions, respectively at 300K. The model is periodic in x and y, but not in z in order to have a free surface in z direction for deposition. Equilibrium lattice constant for Ni was calculated using the total lattice number in the model and the volume at which system pressure attained a value very close to 0, during a simulation of isothermal-isobaric (NPT) ensemble.

Next, system is formed with the computed lattice constant a=3.5357Å at 300K via performing an NVT run for 100ps. Periodicity is removed in Z direction by introducing a 1nm vacuum space in both directions in the data file which is generated at the end of the periodic NVT run. The density profile is generated to check if any half planes exist at both ends and are removed if any. This model is run in NVT for 10ps keeping bottom 6 layers frozen (forces and velocities are set to zero for all atoms in that region) to equilibrate the free surfaces just formed.

Before starting deposition two new regions are defined in the substrate in addition to the bottom region. First one is the region called “surface” which includes the uppermost 6 layers and the other is region “top” which includes all layers in between surface and bottom regions. Then, Au atoms are deposited randomly at a rate of 1 atom per 3 picoseconds (3000 simulation steps) until a full monolayer is formed. Surface region, where deposition takes place is simulated in an adiabatic (NVE) ensemble in order to prevent thermostat (NVT) algorithm affect the deposition trajectories (see Figure 5-1). In preparation of the model, initial goal is obtaining a complete Au monolayer. Thus, after the first deposition step the largest 2D island is selected and monolayer is forced to grow around this island (more be discussed in the following chapter, see Figure 6-2).

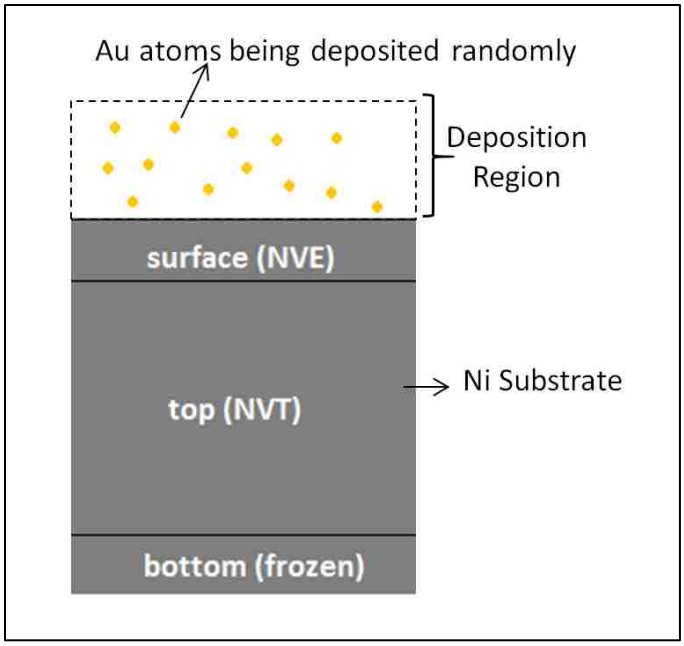

Figure 5-1 Schematic showing deposition process of Au atoms onto Ni substrate

Prior simulations indicated that Au on Ni(001) grows at least the first few layers in a layer by layer fashion [13]. Indeed, during deposition simulations here, atoms were observed to migrate down at step edges of initially formed 2D islands (i.e. down Schwoebel hops) whereas no such hops in the opposite sense (i.e. up Schwoebel hops) were observed. No attempt was made to compute the energy barrier associated with such hops (i.e. the Ehrlich-Schwoebel barrier, [91], [92]) for this model; however, layer by layer growth – at least initially – was confirmed. Consequently, ongoing deposition resulted in formation of 2D islands. To form an ideal Au monolayer, after an initial deposition step, one of the biggest islands was chosen to be kept and the rest of the Au atoms were manually deleted from the system. After each subsequent deposition step atoms sitting on the single growing island and atoms scattered away from the island were removed. This forced the system to grow a single, defect free crystalline monolayer on the Ni surface. To ensure that the monolayer was ideally dense, several Au atoms were inserted manually into the monolayer at random locations and the system was run for equilibrium

for 100 picoseconds after each insertion. This process was repeated until the inserted Au atoms were observed to leave the monolayer over to the second layer on top, which indicated the film was fully dense.

The Au monolayer atoms adopted a (111) hexagonal structure; as shown in Figure 5-2, using the underlying Ni(001) crystallography as reference, essentially straight rows of Au atoms were oriented along (110) type directions. To create the most simplified coalescence geometry, it was desired to remove a single row of Au atoms along either x or y; however, for Au grown on the initial Ni substrate orientation (i.e. (100) type directions along x, y, and z), only atomically zig-zag lines of atoms could be identified along x and y (see Figure 5-2). To overcome this, the Ni (001) surface formed was reoriented 45 degrees in XY plane so that (110) type directions laid along both x and y; the deposition process described above was repeated and the desired simulation configuration was so achieved (see Figure 5-).

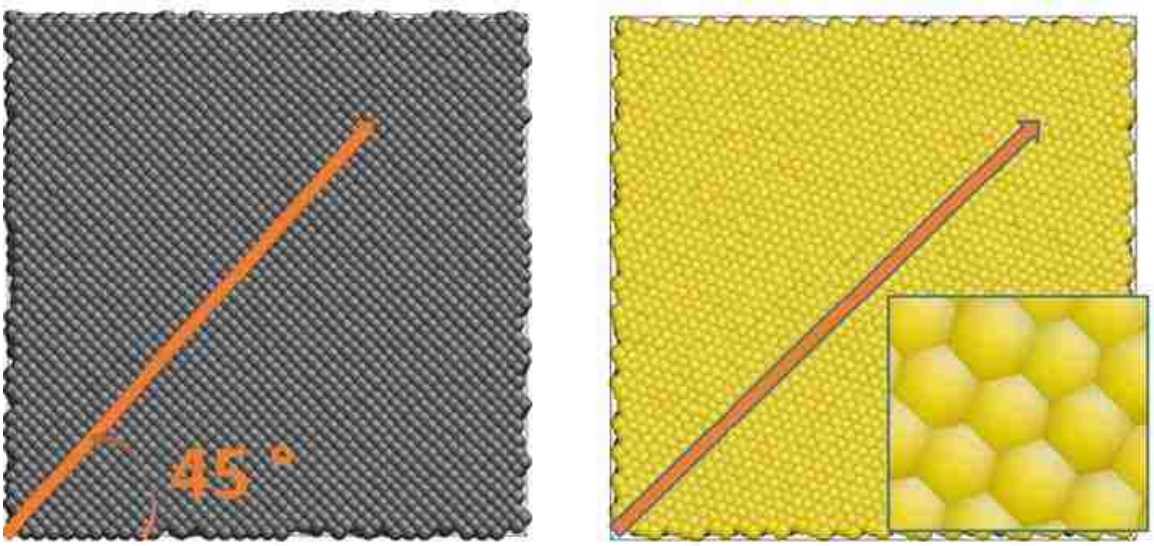

Figure 5-2 Top views are shown for the bare Ni (001) surface (left) and the Au monolayer grown on the Ni surface (right)

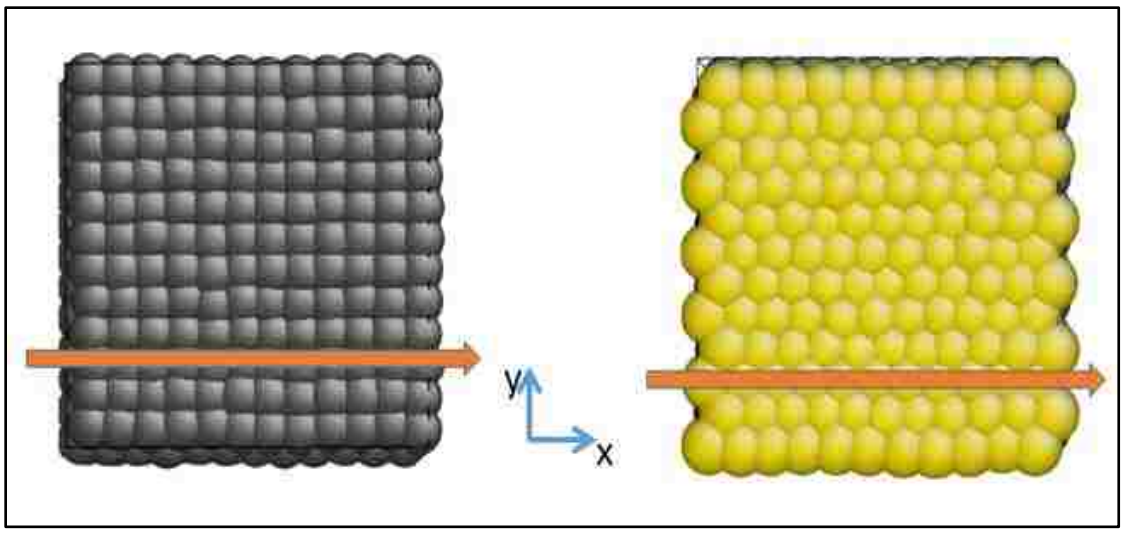

Figure 5-2 Looking "down" on the bare Ni (001) surface but with (110) directions oriented along x and y (left); deposited Au monolayer where Au atoms form straight rows horizontally.

With the Au monolayer so formed, an ideal line defect was formed via removal of Au atoms lying on the centerline of the film in x direction. This process yielded our primary set up of approximate size 3nm in x, 3nm in y, and 20nm in z directions. To explore the effect of system size, our primary system was then replicated in x and y directions to create systems of desired dimensions. In Figure 5-, the models formed by replication of the primary model in the y direction are shown. Given the use of periodic boundary conditions in both x and y, models so formed are of an infinite array of Au patches separated (in x) by single atom wide linear gaps. We describe such simulations as models of periodic islands and these will be distinguished from discrete islands. For periodic (and discrete) islands, in the x direction, Au islands (and gaps) are modeled to be infinite in length; however, a physical length scale exists and is given by L_x, the dimension of the simulation cell in x. Figure 5- shows periodic island systems with varying while Figure 5- shows periodic island systems with varying L_x. These model structures will permit my proposed work to probe stress evolution during coalescence of 2D ideal structures with different feature size.

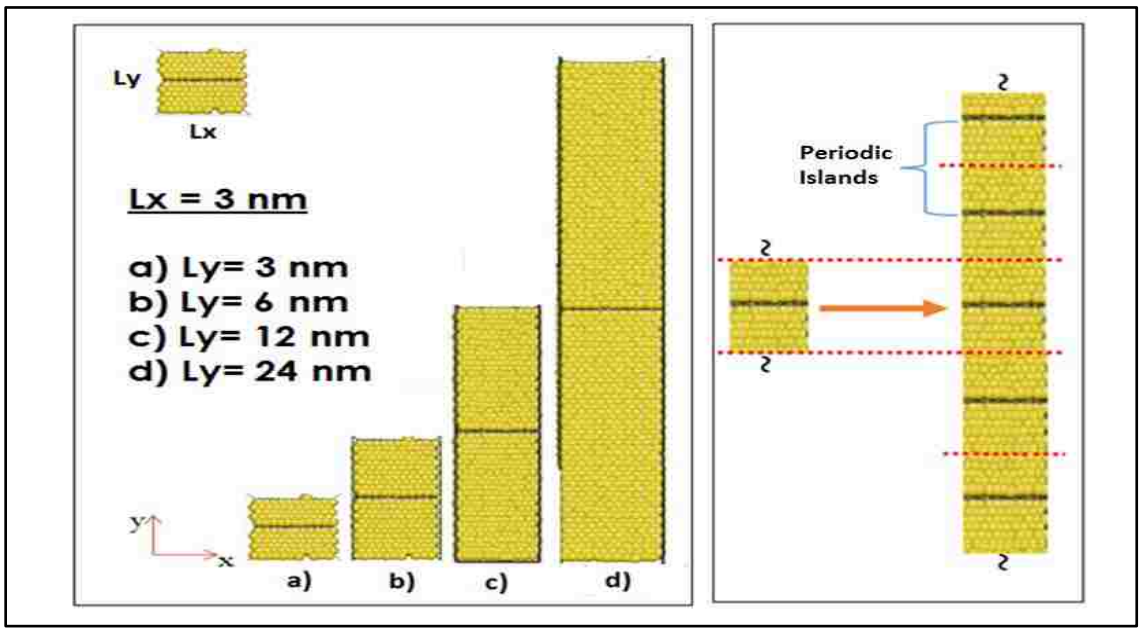

Figure 5-3 (Left) Periodic Au islands on Ni (001) substrates with L_x = 3 nm are shown for a) L_y = 3 nm, b) L_y = 6 nm, c) L_y = 12 nm, and d) L_y = 24 nm. (Right) A schematic representation is shown of how the model corresponds to an infinite array of islands.

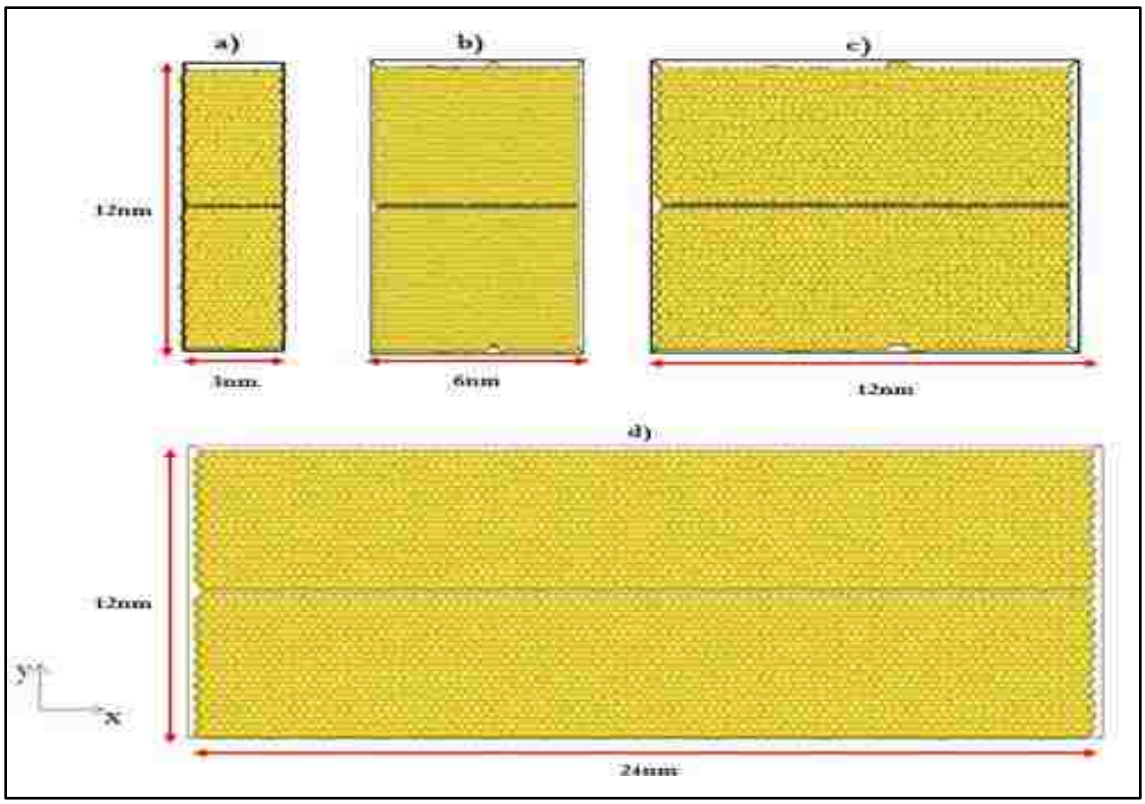

Figure 5-4 Top down views of periodic island models where L_y=12 nm and for a) L_x=3nm, b) L_x=6 nm, c) L_x=12 nm, and d) L_x=24 nm.

5.2 Analysis to Define Thin Film Thickness for the Models

Calculations have been performed to ensure that substrate sizes used here are sufficiently large that no simulation artifacts are introduced into the stress response due to monolayer coalescence.

Surface atoms in low index metals have a lower electron density than the bulk atoms and which leads them to adopt a smaller equilibrium lattice spacing to attain higher electron density. Contrary to this mechanism, bulk atoms impose an epitaxial constraint on the surface atoms, force them to adopt the same atomic registry with the underlying bulk layers, which thus in a surface tensile stress. The interaction between the substrate surface and the film atoms (i.e. the interface)

can also result in stress in the film due to the mismatch of the equilibrium lattice spacing or thermal expansion coefficients etc. Having said that, in order to be more realistic, determination of the minimum size in Z direction possible for computational constraints (the depth of the system) which would allow us to include all the effects from bulk and the interface became crucial. In the literature preliminary analysis have been performed for similar concerns where Luedtke et al. [13] completed their work on Au-Ni metal pairs using a 7 layers thick substrates and found similar results in terms of film texture and surface mixing behavior which will be discussed in the next chapters**.** In the study by C.M. Retford et. al. [93] , the formation energy of a Ge island grown on Si substrate was found to decay exponentially by the substrate thickness and converged to a steady value after 200 monolayers of Si. In another recent study, relevant to this work here, was done by Haifeng Zheng**,** [87] where stress evolution during coalescence of hemispherical Au islands on Au substrate was modeled in LAMMPS. Zheng modeled 3 identical systems with different substrate depths, as 5nm, 10nm and 20nm. He found the average tensile stress computed was not changing significantly after 10nm, thus he decided to continue with 10nm for the rest of his work.

In our work we started with 20nm in z for the Ni substrate (~100 Ni layers), which is less than that in Retford's work and higher than that in Zheng's study. We have also conducted a depth analysis where we plotted the average stress changes in Ni layers starting from top to bottom. Results were convincing that 20nm was more than enough for the reliability on stress evolution simulation. In Figure 5- below, L_x=L_y=12nm system with L_z =20nm is shown as a sample for depth analysis. Coalescence was completed at the center defect after 40ns of simulation run which put Au film monolayer in tension and the uppermost layer of the Ni substrate (dotted curve) in compression (less tension in the corresponding region). However, this effect is observed to become insignificant at deeper layers. This observation confirmed that 20 nm deep Ni substrate is reasonable.

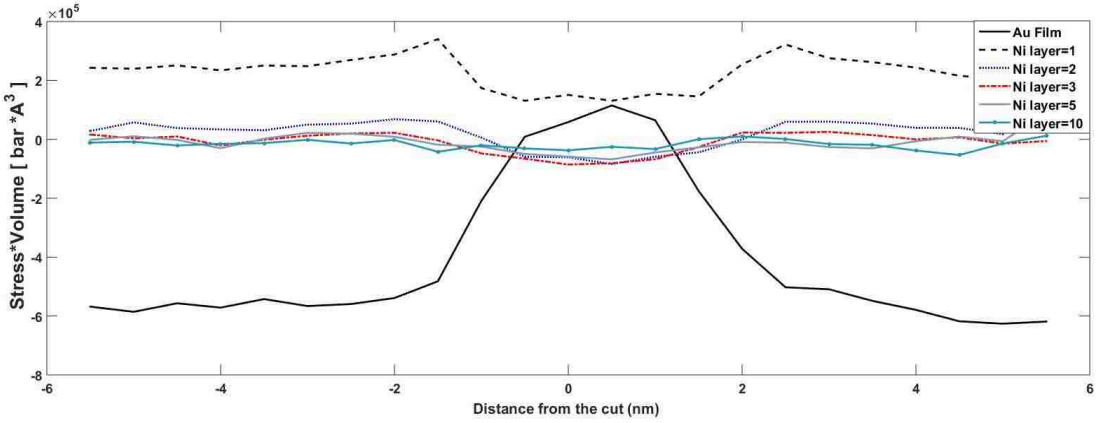

Figure 5-5 Average stress*volume values (raw data) are plotted for successive layers, starting from the Au film layer at the top and including Ni layers at several depths for the sample system with L_x=12nm, L_y=12nm and L_z=20nm after a coalescence run of 40ns.

Chapter 6 Stress Evolution during Early Stages of Island Formation

6.1 Epitaxial Stress Formation

The first stage during the formation of the thin films is the discrete island step where islands start to grow on the substrate randomly. Depending on the growth mode adopted, monolayer islands can grow to coalesce with other islands to form the first film layer or they start growing 3D islands which later impinge on other islands or they start growing in layer by layer mode then turn into building 3D islands for the continuing formation process (see Section 2.4). Especially during the early stages of film formation, the pseudomorphic growth stage, the film atoms deposited on the surface will be forced to adapt the same registry with the surface atoms of the substrate. If the film forms a coherent interface with a substrate of different lattice constant, epitaxial misfit occurs at the interface (see Figure 6-1) [94]. This misfit mechanism yields epitaxial stress which is one of the main sources of stress in very thin films [32].

The amount of the misfit stress depends on the difference in the lattice constants of the film and the substrate materials such that:

$$\varepsilon_{mf} = \varepsilon_{xx} = \varepsilon_{yy} = \frac{a_f - a_s}{a_f} \tag{6-1}$$

In this equation ε_{mf} is the misfit strain under the assumption of anisotropy for the very thin film. a_f and a_s stands for the lattice constants for the film and the substrate, respectively as shown in Figure 6-1.

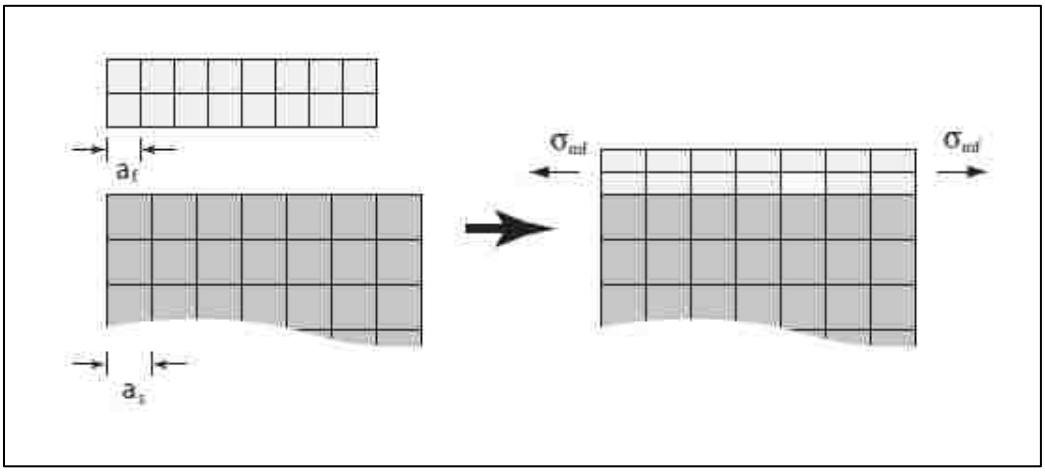

Figure 6-1 Schematic representation of the misfit stress generated due to the epitaxial mismatch between film and the substrate.[94]

Epitaxial stress can be very crucial in thin films since a 1% of strain can lead to a stress of around 2GPa which is well beyond the tensile strength of most metals [32]. Introduction of misfit dislocations through slip planes is one of the mechanisms known to relieve the epitaxial stress accumulation during film growth. This mechanism will be discussed more in detail in the last chapter where Au film is grown with deposition onto the Ni substrate. In this chapter we will focus on the early stage stress evolution during growth of a 2D Au island on the Ni (001) substrate.

As explained in Section 5.1, Au film was grown step by step starting from a small 2D island up to a full monolayer. The equilibrium lattice parameters for Au and Ni at 300K were computed to be $a_{f(Au)} = 4.0953\,\text{Å}$ and $a_{s(Ni)} = 3.5358$ Å. Substituting these values into Eq.(6-1) above yields a misfit strain of $\varepsilon_{mf} = 0.1366$ (13.6%) which corresponds to a very high stress in the Au film as calculated below.

The Au film layer is in single crystal structure, stress calculations are based on the assumption of anisotropy. Additionally, film is in plane stress condition where $\sigma_z = 0$. The Hooke's law applied for the stress on the thin film having its {111} plane parallel to the {001} substrate is given as follows [94] (also see Eqn. (3.50) in Ref.[2]) :

$$\sigma_{mf} = 6C_{44}\left[\frac{C_{11}+2C_{12}}{C_{11+}2C_{12}+4C_{44}}\right]\varepsilon_{mf} \tag{6-2}$$

where $C_{11} = 190\ GPa$, $C_{12} = 161GPa$ and $C_{44} = 42.3GPa$ for Au of anisotropic characterization [95]. Substituting these stiffness coefficients into the equation above we obtain misfit strain for the Au monolayer of (111) texture sitting on the Ni (001) substrate surface as σ_{mf} =26.1GPa of compressive stress for the %13.6 strain which is significantly a high value. It is important to note that this is the upper limit for the compressive stress, provided that Au film would possess the perfect atomic registry with the underlying Ni surface, which is not the case as will be shown in the next section.

The misfit stress is expected to be relieved via either formation of dislocations or 3D islands. There is a critical thickness limit for the thin films where dislocations start to grow on the sliding planes of film crystal to relax the system and after which film converges towards its original lattice size.

For FCC metals (e.g. Cu, Ag, Au, Al, and Ni) slip planes are given as {111} in the 110 slip direction [96]. Burger vector norm, b, for the FCC lattice is calculated using the formula given below:

$$b = \frac{a}{2}|< 110 >| = \frac{a}{\sqrt{2}} \tag{6-3}$$

where a is the lattice constant for the crystal. Misfit dislocations initiate and slip on the planes when the film reaches to the critical thickness. Matthew's formulation of the critical thickness was approximated into a simple equation depending on the Burger's vector and the misfit strain as follows [97]:

$$t_{critical} = \frac{b}{9.9\ \varepsilon_{mf}} \tag{6-4}$$

Substituting lattice constant for the Au film and misfit strain computed above into Eq.(6-3) and Eq. (6-4) we obtain the critical thickness as $\boldsymbol{t_{critical}}$**=2.14Å**. This is very close to the thickness obtained for the Au film monolayer on Ni substrate which yields the conclusion that the dislocations would start right after the first layer as deposition continues if the film would attain the perfect epitaxial registry with Ni substrate. The actual lattice size attained by the Au film atoms on the Ni surface and the corresponding critical thickness is given in the next section.

6.2 Stress Evolution during Au Film Growth

In Section 5.1 we covered how Au island islands grew to form the full film monolayer. In this part, we will focus on the stress evolution over the growing island islands and the film structure changes in the course of growth.

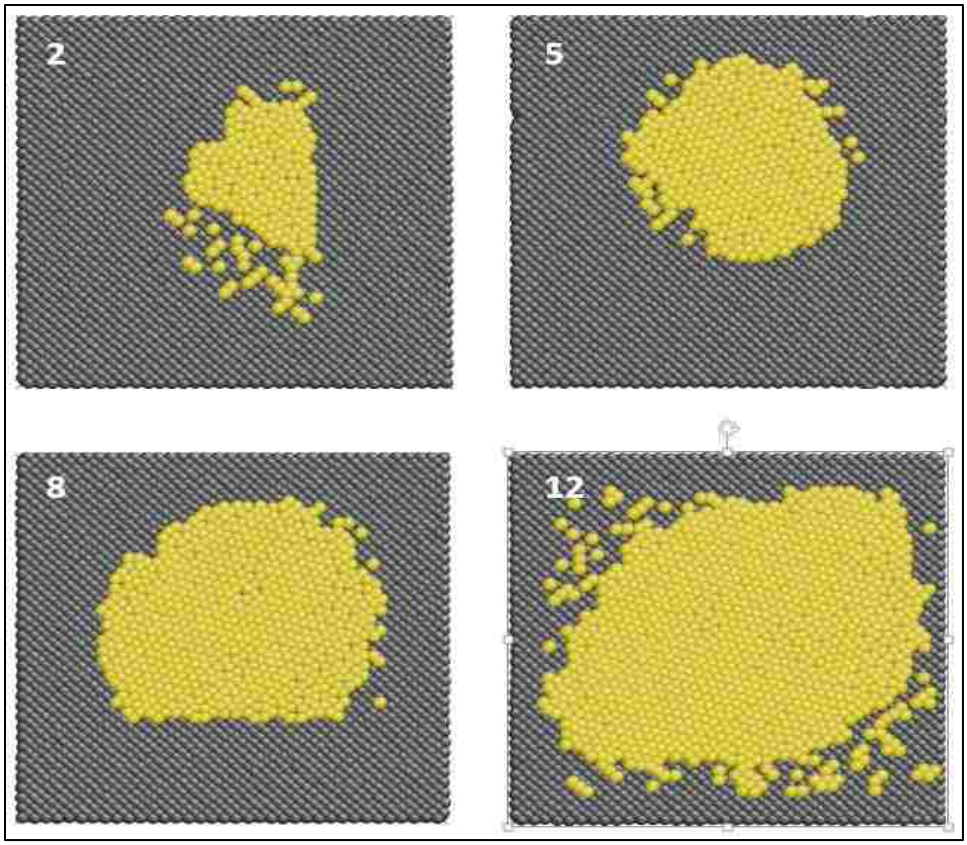

Figure 6-2 Selected steps of the growth of Au island on Ni 001 surface are shown where hexagonal 111 structure is adopted. (Steps 2, 5, 8 and 12)

The deposition process was interrupted between each step of 100 atoms deposition to clean up the atoms on the island to force the system to grow a single layer. Similarly, the atoms away from the island were also removed before launching the next step to avoid multiple island growth in order to eliminate any stress contribution due to coalescence processes. These

modifications enabled us to work on the early stages of stress evolution on a single island more specifically.

As given in Figure 6-2 above, the island started to get into 111 hexagonal order after the 5th step and kept the same structure to the end. Stress information is dumped during the deposition process to keep track of the stress evolution of the island.

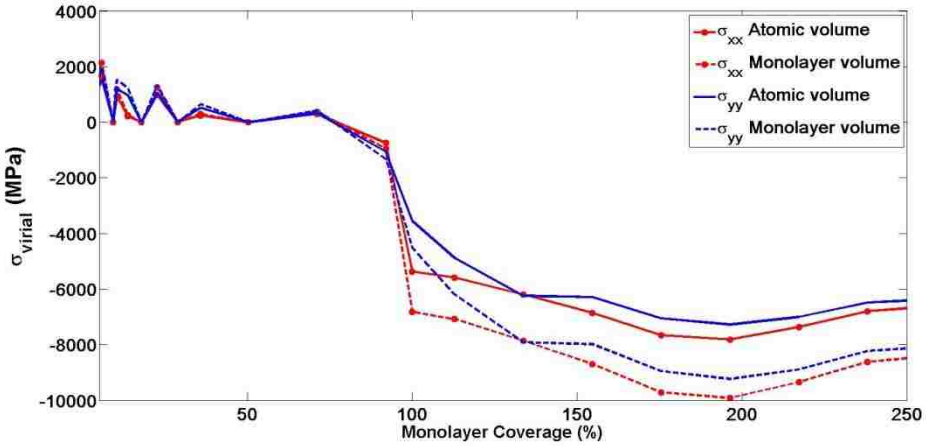

Figure 6-3 σ_{xx} and σ_{yy} components of the virial stress evolution obtained using two different averaging volumes (atomic volume vs monolayer volume) as the monolayer island grows on the substrate is shown with respect to the coverage percentages.

In Figure 6-3, evolution of σ_{xx} and σ_{yy} components of the virial stress are presented as coverage goes to a full monolayer. In one case, averaging volume was taken to be the atomic volume which was obtained from the equilibrium lattice constant for Au at 300K (i.e. a_{bulk_Au}=4.0953Å) where FCC cubic crystal volume is simply divided by four (the number of atoms in a single cubic FCC crystal). Average (stress*volume) per atom values (i.e. the energy term in Eq. (3.47)) computed in MD simulations are divided by the atomic volume yielding the virial stress values, as shown in Figure 6-3 above for σ_{xx} and σ_{yy} with circled-solid and solid lines, respectively. In the other alternative case for volume definition, we computed the island volume

from the island area and the island thickness. For the area of the growing island we used the full monolayer system size as the reference to obtain the area per atom value out of it and multiplied that value with the total number of atoms in the island to get the approximate area of the island. The thickness was found to be 0.2 nm from the vertical (in z) density distribution analysis. The corresponding results are also shown in circled-dashed and dashed lines in the same figure above. It is clearly seen that the volume definition effect becomes more significant after 100% coverage is attained (see Section 3.4 for more detail in atomistic stress calculation methods).

As seen in Figure 6-3 above, stress in the growing island starts with tension, indicating the attraction between surface atoms of the Ni substrate and film atoms of the Au island and becomes more compressive as the island grows to a monolayer. This interaction which is relatively strong enabled us to obtain a layer by layer growth similar to what was reported in previous studies [13]. The strength of the interactions surpasses the compressive effect of epitaxy imposed on the film layer by the substrate of smaller lattice size. However, as the island reaches to a certain size, the epitaxial effect starts dominating the film in overall, thus the stress curves display a compressive behavior towards the end of completion of the first layer and for further growth. The compressive stress values (based on atomic volume definition) attained at the full monolayer level is 5.3GPa and 3.6GPa for $\sigma_{xx \text{ and }} \sigma_{yy}$ components, respectively. Corresponding results based on the monolayer volume definition were found to be 6.8GPa and 4.5GPa compressive for both $\sigma_{xx \text{ and }} \sigma_{yy}$ components, respectively. σ_{yy}= 4.5GPa will be also used as a reference base value in the following chapters to find the delta stress values since we have used similar volume definition for the coalescence and post coalescence deposition studies discussed in the following chapters.

Alternatively, stress behavior was evaluated via first neighbor distance analysis of the growing islands. In Figure 6-4, the average first neighbor distance for the islands is plotted with

respect to the coverage percentage. A parallel behavior was observed where spacing dropped significantly towards completion of the monolayer.

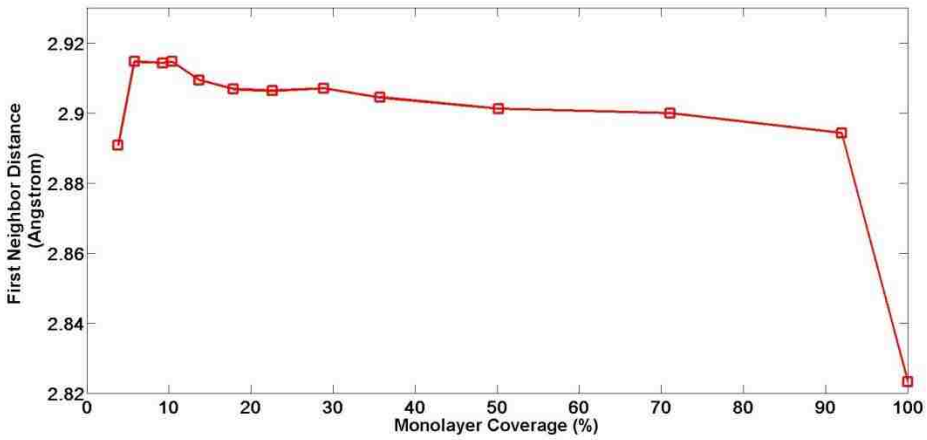

Figure 6-4 Change in the spacing for the island is shown with respect to percent coverage.

We can apply the Hooke's law for the epitaxial stress discussed in the first part of this chapter to find out the corresponding plane stress value for the film. In the figure above, we have the first neighbor distance to be d_{full_ML}=***2.8233 Å*** when monolayer is %100 completed. We can deduce the lattice constant using the first neighbor spacing information as described in Figure 6-5 below. The corresponding lattice constant for the full monolayer state given above is calculated to be a_{full_ML}=***3.9927 Å.***

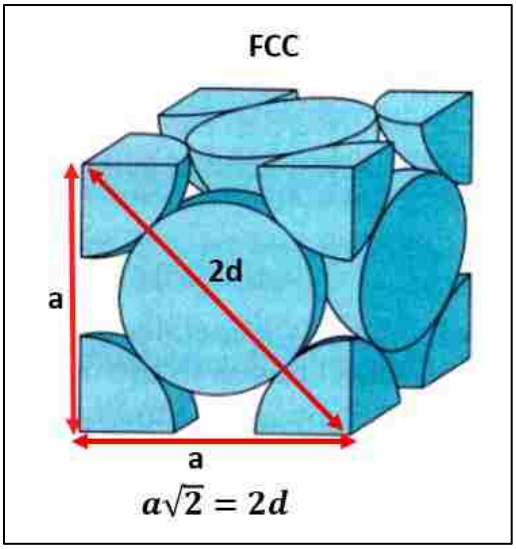

Figure 6-5 The relation between the first neighbor distance and the lattice constant is shown for the FCC crystal structure.

Using Eq. (6-1) with the lattice constant of Au given in the first part for the bulk Au as a_{Au_bulk}=***4.0953 Å***, we find the strain on the full film to be ***2.5%*** compression with respect to the bulk Au. Substituting this amount of strain into Eq. (6-2) yields ***4.7 GPa*** of compressive stress.

If we do the reverse calculation to find out the equilibrium first neighbor spacing using the lattice constant of Au, we get the value for the bulk Au to be d_{Au_bulk}=**2.8958 *Å***. Regarding this spacing distance, we can also conclude from Figure 6-4 that the growing island initially starts with tension and evolves towards relaxing the compressive stress due to the strong island and Ni surface atom interactions. As the islands grows bigger in size, the ratio of the atoms in the periphery of the island which induce tensile stress into the island drops down and compressive stress starts to dominate where eventually reaches to a maximum at the %100 coverage level.

The initial tendency towards compressive stress generation obtained here follows the experimental findings which report compressive stress generation during early nucleation stage of film formation process.

For the further deposition, where second and third layer start to grow, we did not apply controlled growth for the second layer islands. They grew randomly at different sizes and locations. It is observed that compressive stress generation slowed down and started to relax after the second monolayer was completed (see Figure 6-3). This was expected to happen since the Au atoms start to impose the larger lattice on the monolayer underneath, relieving the compression due to substrate mismatch effect. As discussed in the previous section, misfit dislocations arise at a critical thickness which is given as a function of the misfit strain and the equilibrium lattice constant in Eq. (6-4). Substituting $\varepsilon_{mf} = -0.25$ found for the Au film on Ni 001 substrate into Eq. (6-4) we get the actual critical thickness for this system as $\mathbf{t_{critical}}$**=11.6 Å,** which corresponds to 5 to 6 monolayers. Misfit dislocation will initiate at around this thickness and relieve the accumulated stress.This behavior was studied in more detail in Chapter 8.

Chapter 7 Stress Localization Observed During Coalescence Stage of Au Thin Film Formation on Ni (001) Substrate

Coalescence event is a major process which changes the stress drastically as reported in the experimental studies [1], [10], [67]. In many cases stress curves display a significant tensile jump due to grain boundary formation and cohesive attraction during coalescence. Relaxation of the resulting tension and the distribution of the stress over the film depends on various parameters like the film material mobility [27], surface chemistry [26], [41], [71] or size related effects, etc. Models proposed in the literature fall short in explaining initial film formation stages where bulk properties may not apply. Stress evolution studies; in general, considered the overall behavior in the film rather than distribution pattern of the stress over the film. However, as discussed above stress generation manifests differently at certain regions like grain boundary formation sites, surface edges, impurity regions etc. Therefore, stress and morphology is expected to be altered and more critical around these sites where failures are most likely to initiate from. For this reason, it is important to understand the early stress evolution and distribution over the films spatially and temporally.

Atomistic simulation of an idealized coalescence event at the initial regime of the film formation is expected to help us explain the stress distribution and substantial relaxation behavior qualitatively and to extract quantitative data for the maximum stress values occurred and correlate them with system geometries.

In this regard, this chapter is concentrated on stress evolution taking place during coalescence and post coalescence stages of film growth via molecular dynamic simulations. As

explained in Section 5.1, a single Au film monolayer with a linear defect is prepared on a Ni substrate. In this system Au-Ni pair displays a large amount of misfit and both have positive heat of mixing that provides a clear interface without any intermixing.

Coalescence event for the highly characterized linear defect is modeled for different system sizes to find out spatial and thermodynamic manifestation of the film stress and morphology evolution. Simulations also give us a measure for size dependencies and the effect of interatomic interaction strengths. This chapter has two parts dedicated to the stress behavior during coalescence of periodic islands of Au film monolayer and coalescence of discrete islands, respectively.

7.1 Stress Localization During Coalescence: Periodic Monolayer Islands

In order to observe the spatial and temporal evolution of stress during coalescence regime of island formation via MD method, Au thin film monolayer on Ni substrate with a highly characterized linear defect was modeled as explained in detail in Section 5.1. Two sets of periodic islands were prepared as shown in Figure 5-3 and Figure 5-4 and they were set to run for coalescence.

The Au monolayer deposited is assumed to be in anisotropic plane stress condition, where film experiences significant amount of stress changes in y direction, which is perpendicular to the defect line. Therefore, atomic stress per atom (virial stress) in y direction (σ_{yy}) is dumped into files at periodic time intervals. The computed stress is in energy units (i.e. stress*volume) as described in Section 3.4.

In the post processing part our work for analyzing stress behavior, we divided the film surface into bins of 0.5nm wide in y and calculated the average stress for each bin by using the bin volume as the averaging volume for the virial stress computations (see Figure 7-1). The bin width corresponds to the width of two lines of Au atoms approximately. Different bin sizes are also tested where high noise was observed for smaller bin sizes and loss of stress gradient was encountered when wider bins are used as shown in Figure 7-2. We would expect to have less fluctuation as we go from 0.5nm to 0.6 nm but it did not happen due to windowing error where bins started to include varying number of Au atoms since the width violated the repeat length of 0.25 nm which corresponds approximately to one Au atom line thickness. That is why we see less fluctuation when we go to 1nm width bins where we had less gradient resolution but also less fluctuation.

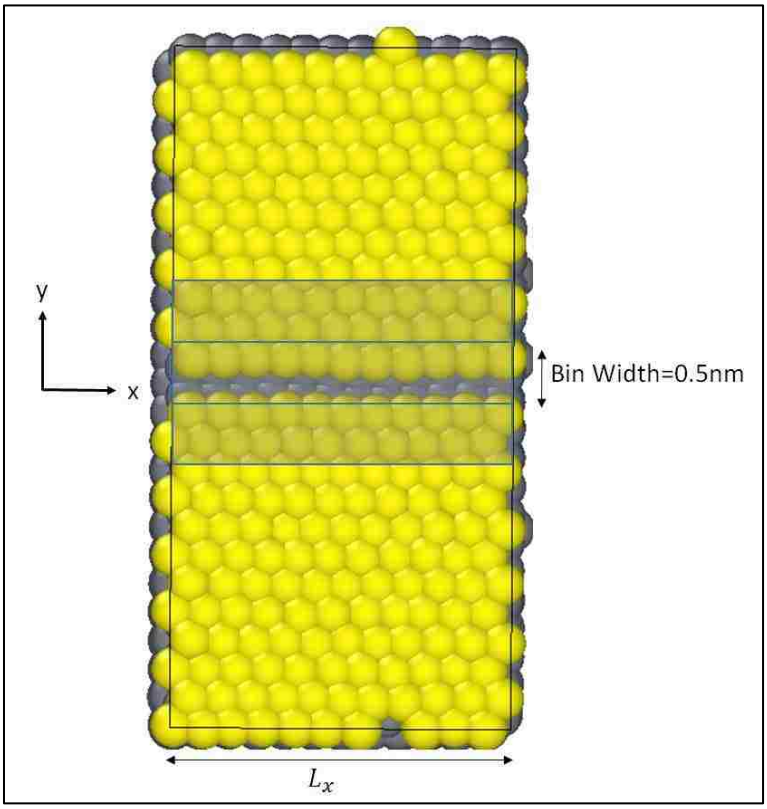

Figure 7-1 Sample Au periodic island with the linear defect and the bins are illustrated, origin being at the center.

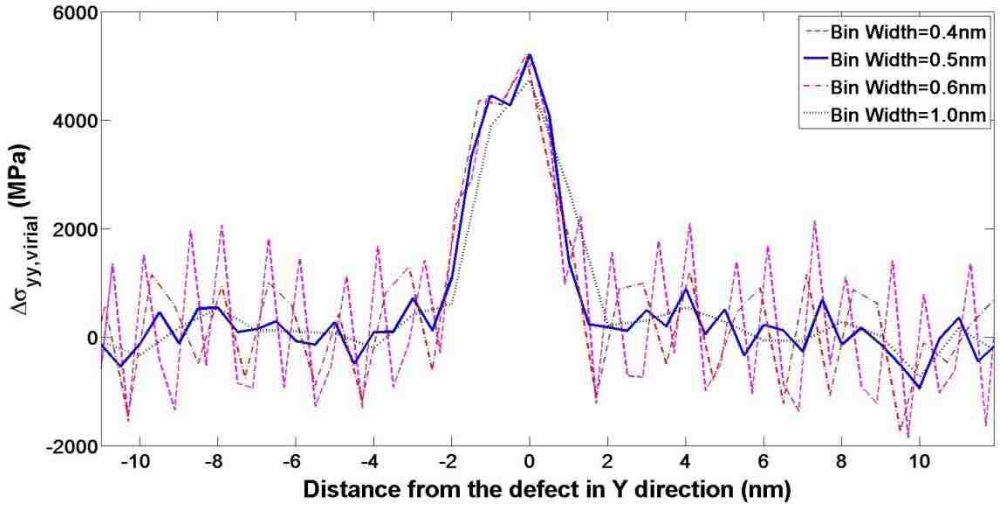

Figure 7-2 Stress distribution curves obtained for different bin widths are shown on 3x24nm model.

The thickness for the monolayer for the volume calculation is taken as 0.2 nm which is derived from the density profile analysis of the system in z direction. The horizontal width L_x for the bins varies for different models. The bin volume (width)*(thickness)*(L_x) has been used as the averaging volume in virial stress calculation for all models simulated hereafter in this work.

Coalescence simulations are first performed for the first set of periodic islands. At the end of 100ns long run 3x3 nm system (Model-a in Figure 5-3) was seen to close the defect fastest at around 1ns and stress distribution was observed to be relatively uniform in the form of a tensile increase in the film due to coalescence. There was not any significant change in the stress behavior in terms of distribution and magnitude computed during 100ns long simulation, which is why this system was not run any further. The delta stress, $\Delta\sigma_{yy,virial}$ ($\sigma_{yy\_COALESCED}$ - $\sigma_{yy\_FULLFILM}$) in y direction, which is the direction of the strain, was computed to be **5GPa** and distributed almost

uniformly over the film (see Figure 7-3). Note that $\Delta\sigma_{yy,virial}$ refers to the time averaged stress value for the last 10ns of the systems in the relevant plots in this study.

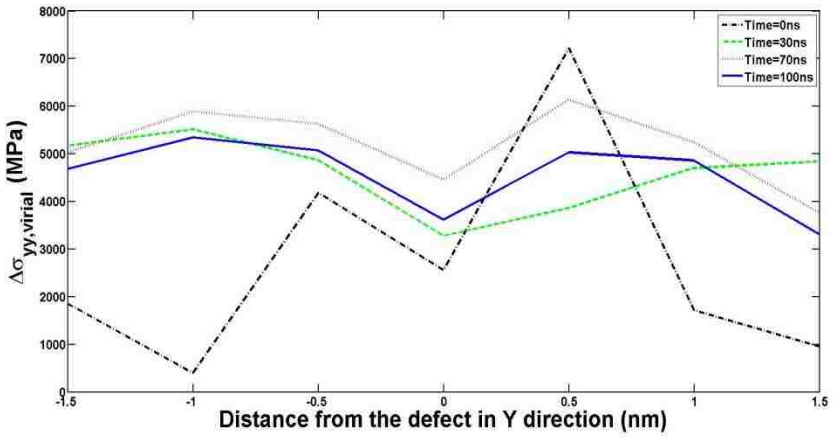

Figure 7-3 Data are shown for the L_x=L_y=3nm system at time t=0 (dash-dot), t=30ns (dashed), t=70ns (dotted) and t=100ns (solid)

On the other hand the other systems displayed a non-uniform stress distribution, where a localized tensile stress was observed to occur around the defect where coalescence was taking place. Furthermore, this stress localization around the coalescence region appeared in the early stages of coalescence and did not relax thereafter although simulations were run longer up to 200ns. A select system, 3x12nm, was even run up to 500ns (i.e. 0.5 milliseconds,) which is relatively long for a MD simulation. The stress localization for this system still existed without any significant changes. Figure 7-4 and Figure 7-5 clearly show the stress localization occurred at the two sets of periodic island models for changing size configurations.

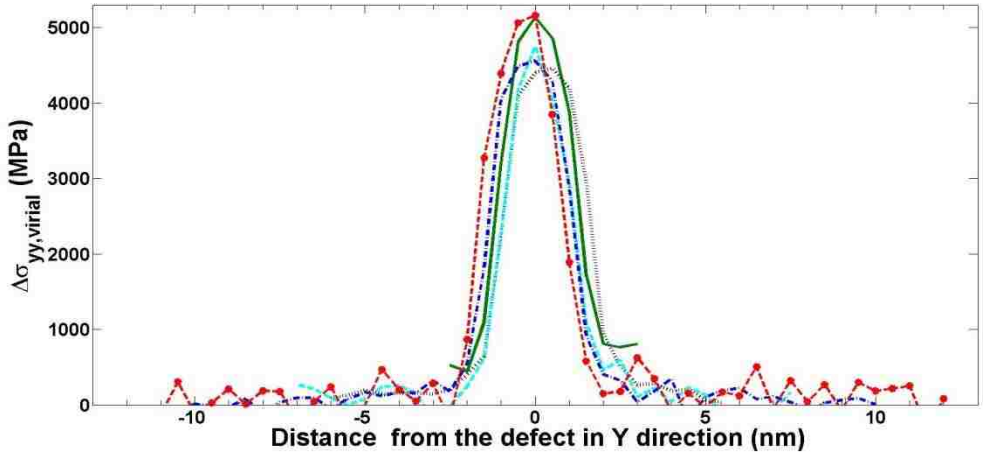

Figure 7-4 All data shown are for L_x=3nm but varying L_y; L_y=6nm (solid), L_y=12nm (dotted), L_y=15 nm (dashed) L_y=21nm (dash-dot) and L_y=24nm (dash-star)

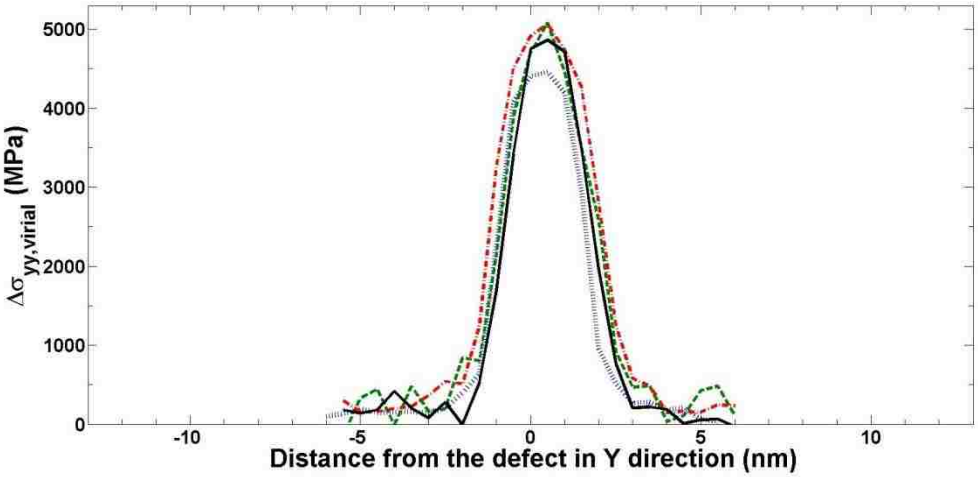

Figure 7-5 Data shown are for L_y=12nm but varying L_x; L_x=3nm (dotted), L_x=6nm (dashed), L_x=12nm (dash-dot) and L_x=24nm (solid)

The localization can also be observed as a disorder at the coalesced region as seen in Figure 7-6 below. This disordered structure has been observed in all coalescing monolayer system simulations performed this work. Figure 7-6 is important since it also shows that atomic structure, thus the stress distribution in x direction is not also uniform. A 2D stress analysis would be needed to capture the stress behavior in x direction as well.

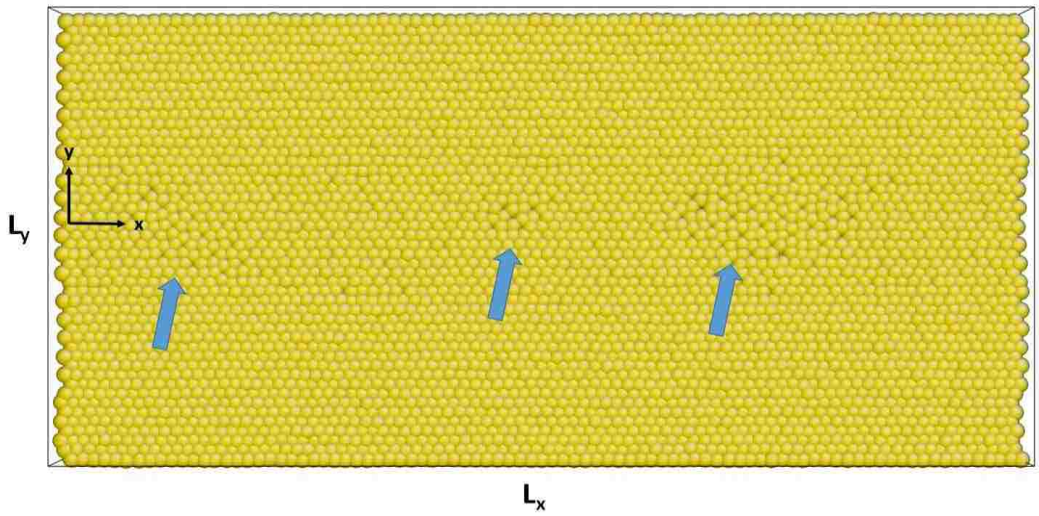

Figure 7-6 Disordered regions for the L_x=24nm and L_y=12nm system after 50 ns of coalescence are shown on the periodic Au film.

Corresponding 2D stress distribution for the system given in the figure above is shown in the contour plots given below. Figure 7-7 shows $\Delta\sigma_{yy}$ stress distribution over the film where it reaches up to around 6GPa while the average value for the maximum $\Delta\sigma_{yy}$ stress was computed to be 5GPa for the stress localization region around the defect. Therefore we can conclude that coalescence effects are not identical in the orientation of the defect, thus stress (all components, as shown below) varies in x direction in the defected region.

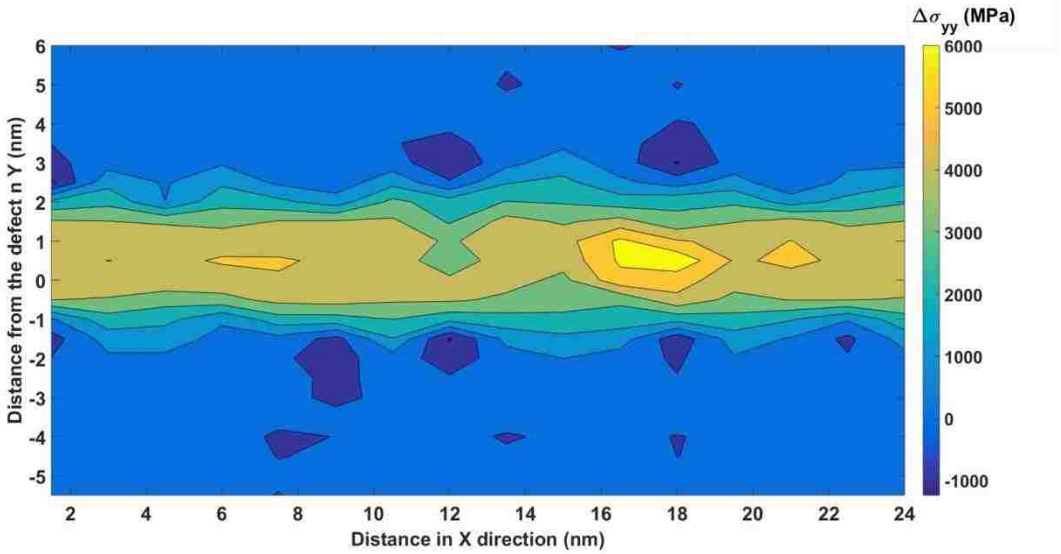

Figure 7-7 Contour plot for $\Delta\sigma_{yy}$ stress distribution over the 24x12nm film monolayer

Figure 7-8 shows the distribution for the $\Delta\sigma_{xx}$ stress where the localization region is similar to that plotted for $\Delta\sigma_{yy}$ above. While there is tension in the defected region due to coalescence event, additional compression has occurred at some spots as seen in both figures .

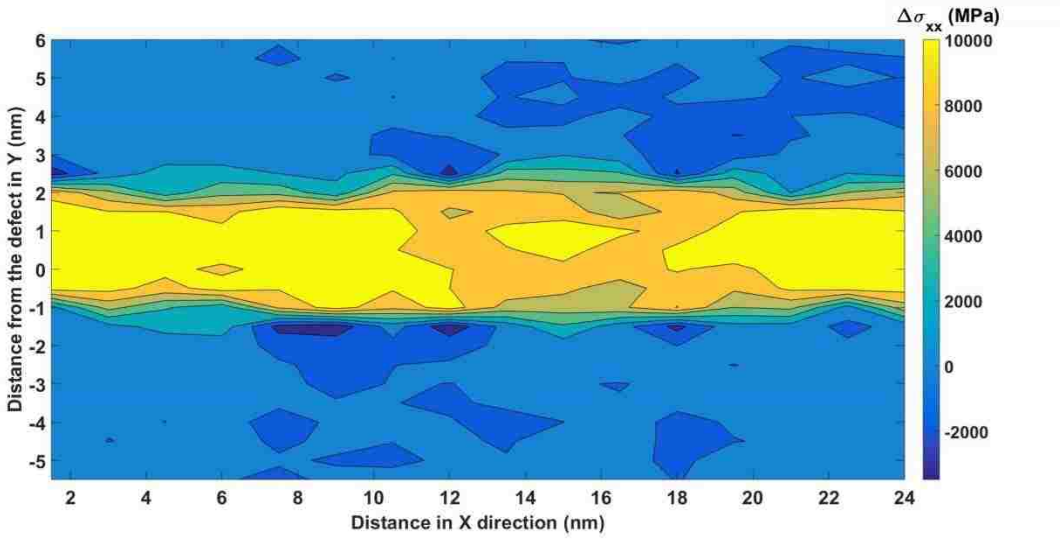

Figure 7-8 Contour plot for $\Delta\sigma_{xx}$ stress distribution over the 24x12nm film monolayer

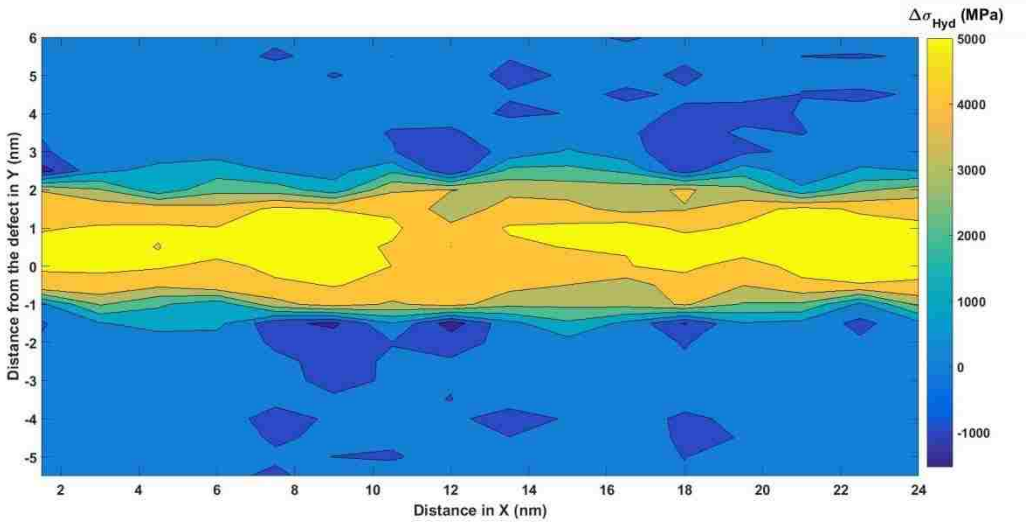

Figure 7-9 Contour plot for the hydrostatic stress $\Delta\sigma_{Hyd}$ distribution over the 24x12nm film monolayer is given where σ_z was neglected in the plane stress assumption.

Lastly, in order to see the combined behavior of the stress over the film we have included the hydrostatic stress distribution over the film monolayer in Figure 7-9. Hydrostatic stress is simply the average of the three normal stress components of the stress tensor.

$$\sigma_{Hyd} = \frac{\sigma_{xx} + \sigma_{yy} + \sigma_{zz}}{3} \tag{7-1}$$

where $\sigma_{zz} = 0$ for the plane stress assumption. Similarly Figure 7-9 shows the stress localization region and the stress gradient in both x and y directions. The maximum stress values attained is found to be around 5GPa.

If we give a closer look at the peak stress values in Figure 7-10 below, we conclude that size effect is not significant on the peak stresses observed (we have also included intermediate sizes of L_y=9,15 and 21nm for the L_x=3nm model set). As seen in the figure, the computed virial peak stress values are confined in the range 4.5GPa to 5.1Gpa. Same conclusions are valid for the width of the stress localization region such that width is independent of the system size and it converges to a full width half max value of around 2.7 nm in the infinite size limit (see Figure 7-11). This results also explains why we did not observe a stress localization for our smallest model of L_x=L_y= 3nm. Since the model size is almost same as the general width size of the localization region, the localization region has become the entire film itself. Thus, it should be noted for Figure 7-11 that the width was taken to be 3nm for L_x=L_y= 3nm. When this manual addition is ignored, it is clear that the width does not change significantly as the system size changes.

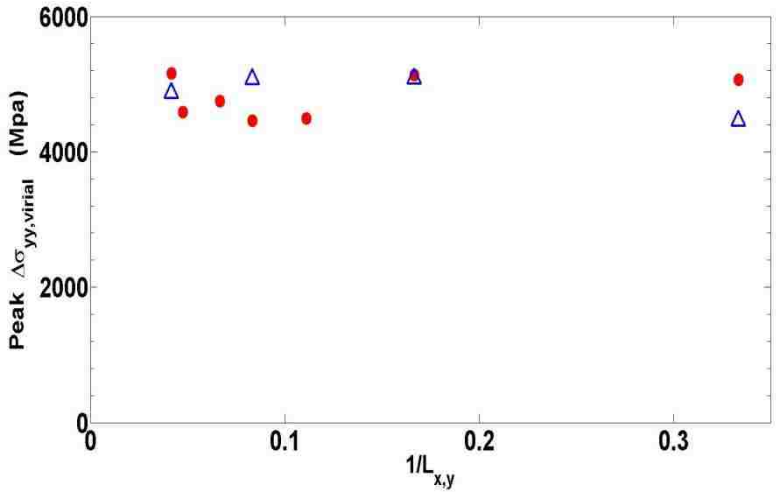

Figure 7-10 Data shown is the Peak $\Delta\sigma_{yy,virial}$ versus $1/L_x$ (circles) and versus $1/L_y$ (triangles)

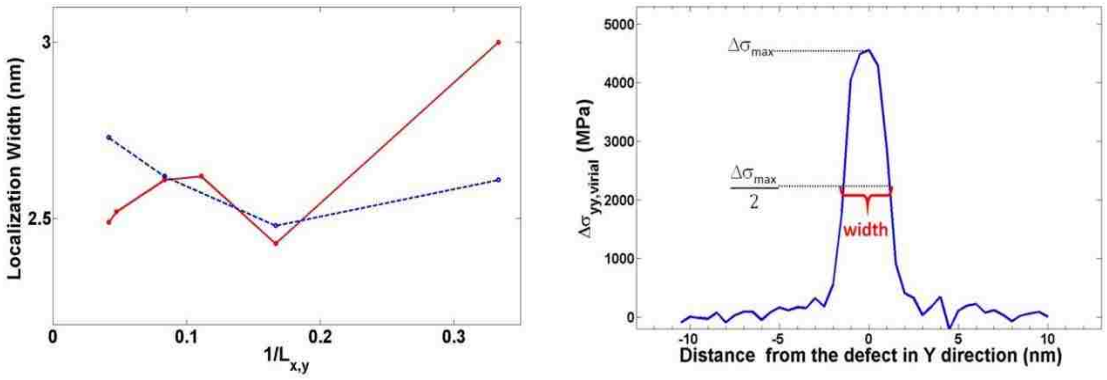

Figure 7-11 Change in width of the stress localization region is shown with respect to $1/L_x$ (solid) and $1/L_y$ (dashed) (left); schematic for the width calculation according to the full width half max method is shown on 3x24nm sample model (right).

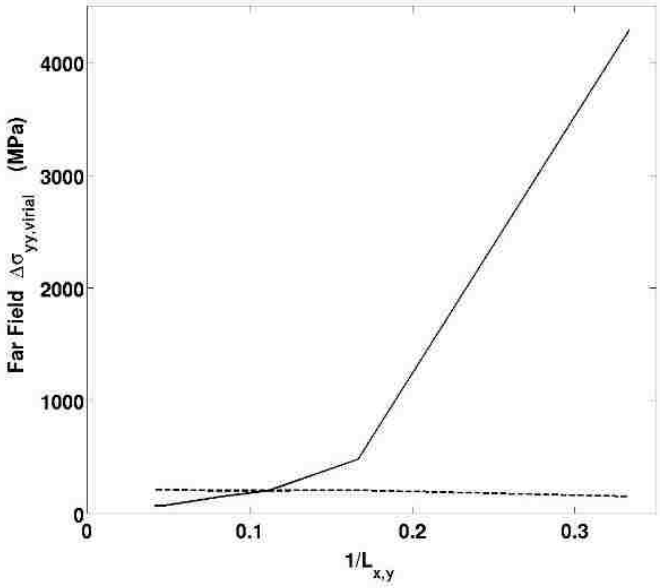

Figure 7-12 Average stress computed for the far field from the defect region is plotted against $1/L_x$ (solid), $1/L_y$ (dashed). Far field stress generation due to coalescence is losing its effect as the system size gets larger, becoming zero at the infinite size.

Contrary to peak stress and stress localization width , mean stress computed at the regions out of the localized stress region is observed to decrease as systems become larger (See

Figure 7-12). This indicates that for bigger systems, the coalescence event generates stress only around the defects and rest of the film is not affected. Thus, no strain (atomic displacement due to strain) or any morhological alterations occur at far ends of the films in larger systems. This is also an important outcome, for strain computations such that one should only consider the size of the localized stress region instead of the full film length.

In the alternative approach we derived stress from the local strain data obtained by computing the spacing for each atom. Plotting the change in the atomic distances for atoms in the full film and in the film after coalescence yielded qualitatively similar results, where strain localization is observed around the initially defected area indicating stress localization (see Figure 7-13). In this figure, atomic spacing is computed for three forms of the Au monolayer for the sample system of L_x=3nm and L_y=24nm is presented. Atomic neighbor spacing computed for the Au atoms in the surface layer of its bulk gets narrower when Au monolayer is on top of the Ni (001) substrate, indicating a state of compression. This is parallel to what we have found in the simulations as the pre-existing stress in the films. The peak in the curve for after coalescence state shows the localization of stress.

In Figure 7-13, first neighbor spacing values for bulk, full monolayer and coalesced film monolayer forms of Au are plotted together. The bulk value is retrieved from the previous chapter as d_{Au_bulk}=2.8958 Å. Curves for the full film and the coalesced film are plotted using the data files for that specific system. The average value for the full film first neighbor spacing was found as d_{full_ML}=2.8233 Å in the previous chapter. The peak spacing distance for the coalesced film occurred at the center is 2.9210 Å.

Using the same procedure as in Section 6.1 to calculate the state of strain and the associated stress amounts with respect to the bulk state of the Au film we find the strain for the full film monolayer to be ε_{full_film}=2.5% (compressed) and for the coalesced film to be

$\varepsilon_{coalesced\_film}$=0.87% (stretched). These corresponding stress values for the full film and the coalesced film are σ_{full_film}= -4.7GPa and $\sigma_{coalesced\_film}$= 1.67GPa, respectively with respect to the bulk.

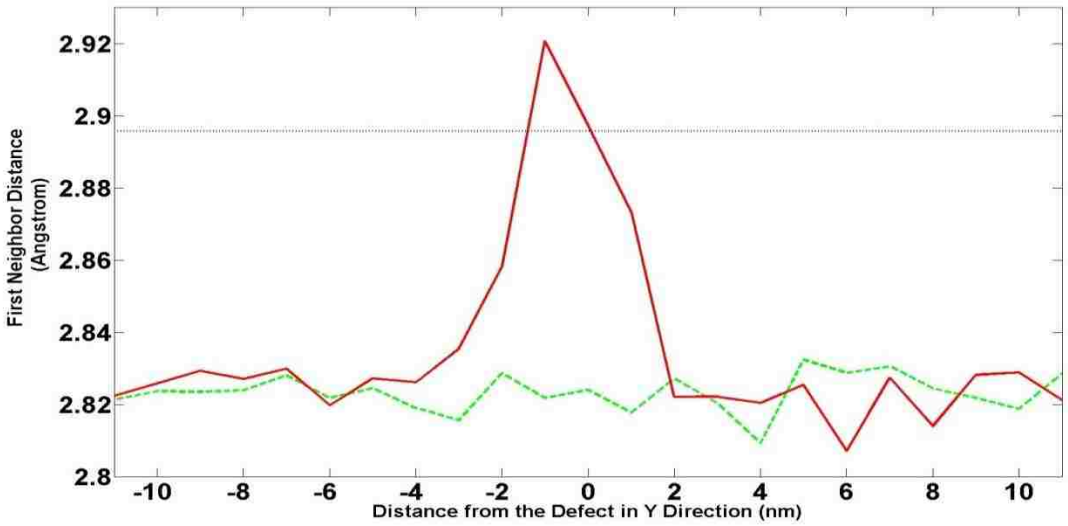

Figure 7-13 First neighbor spacing plots for L_x=3nm and L_y=24nm system plotted for the surface layer of the Au bulk (dotted), Au full film monolayer on Ni (001) substrate (dashed) and Au film after coalescence is completed(solid).

In order to make these calculations comparable to the corresponding virial stress values computed via MD method above, we need to take the full film layer as the reference for the delta stress amount. The coalesced film is strained 3.45% in total with respect to the full film monolayer which yields a delta stress of 6.6GPa. The $\Delta\sigma_{yy,virial}$ value computed via MD was 5.1GPa for the 3x24nm system (see Figure 7-4). Similarly; time $\Delta\sigma_{yy,virial}$ computed using MD for the full film stress was -4.5GPa while it was found to be -4.7GPa via first neighbor distance method (See Table 3).

	Full Film Stress	Coalesced Film Delta Stress ($\Delta\sigma_{yy}$)
MD Virial Stress Definition	**-4.5 GPa**	**5.1 GPa**
First Neighbor Distance Approach	**-4.7 GPa**	**6.6 GPa**

Table 3 Comparison chart for stress calculations for L_y=24 nm system via the virial expression and first neighbor distance approach is given.

As the table tells us, the LAMMPS stress values are on average %15 less than their corresponding first neighbor results for the coalesced film delta stress case, while they are close for the full film case of where there is no defect. As you may recall, the volume definition in virial stress calculation for the monolayer was criticized for the surfaces, especially in the vicinity of defects where significant stress gradients occur. It was also shown that they produce better results for homogenously deformed regions [56]. This can be the reason for the difference with the MD results. Also note that, for the neighbor spacing calculations we have used radial distances instead of distance in a single coordinate as x or y and simply substituted the delta value to get the strain which was then used in Hooke's law above in Eq. (6-2) to solve for the biaxial stress. But, simulation stress results plotted the normal stress value in y direction only (for $\Delta\sigma_{yy}$). Lastly, the reference state for stain calculation is already a deformed state of the Au material (compressed on the Ni substrate) which makes the strain we obtained arguable. Nonetheless, it is worth showing that both approaches yield stress localization.

As a conclusion to this work herein, we have demonstrated that there is stress localization around the coalescing regions of the periodic Au islands on Ni substrates. The peak stress (i.e. $\Delta\sigma_{yy,virial}$), which is tensile, is observed at where the highly characterized linear defect was initially located and the magnitude varied between 4.5 GPa and 5.1 GPa regardless of the system size. The averaging volume taken for the virial stress calculation was the bin volume given as L_x(system size in x)*0.5nm(bin width)*0.2nm(monolayer thickness).

The localization region width size was observed to be independent of the system sizes, converging to a value around 2.7 nm in the infinite size limit. For this reason the smallest system (3x3nm), being almost at the same size with the localization width, did not display a significant localization of stress. For the systems with stress localization at the center, far field stress measurements yield a nice correlation with the size such that it decreased to zero at the infinite size limit.

The alternative approach where first neighbor spacing calculation is used to define amount of strain from which stress is derived via Hooke's law yielded qualitatively similar results of stress localization around the coalescence region.

7.2 Comparing Coalescence of Discrete and Periodic Monolayer Islands

In this part, we will present the stress evolution results for the coalescence of discrete Au islands of single monolayer. For this part, the first set of periodic islands used in the first part above (models given in Figure 5-3) are modified to obtain discrete islands via elimination of periodicity in y direction while keeping the Ni substrate still periodic in x and y directions.

The last model given in Figure 7-14 below is for a new model, where L_y=48nm. This model is simulated to expand the size span studied in this work. Depending on the smaller models' stress evolution behavior, the periodic island form of this model would be also simulated if any drastic change would be detected. Two discrete islands, upper and lower, of identical sizes of width L_x and length L_y are set to coalesce as applied to the periodic islands in the previous section.

At the end of coalescence run of 50ns, the smallest system (L_x=L_y=3nm) did not display any stress localization with the exception of less tension on the lower island. The coalesced islands are in tension, highest value computed for the $\Delta\sigma_{yy,virial}$ to be **~5.7GPa** as the time averaged quantity for the last 10ns (see Figure 7-15).

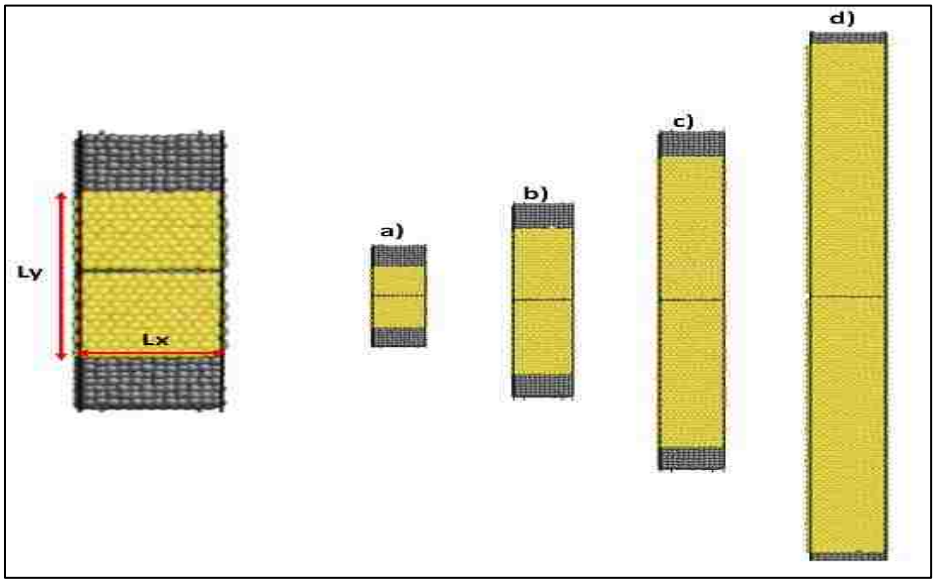

Figure 7-14 Discrete islands models, where L_x=3nm for all, and L_y=3nm, 6nm, 12nm and 48 nm for systems a, b, c and d, respectively.

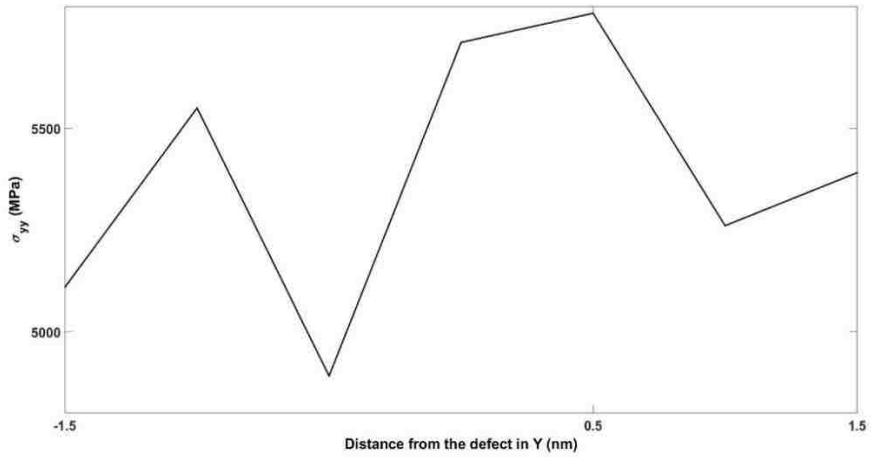

Figure 7-15 Discrete island of L_x=3nm and L_y=3nm coalescing simulation run, at the end of 50ns.

As it is seen in Figure 7-16, similar to the periodic island simulations carried in the first part, there is a stress localization region around the coalesced region. But there is also a tension at both ends of the islands which indicates the edge interactions with the substrate.

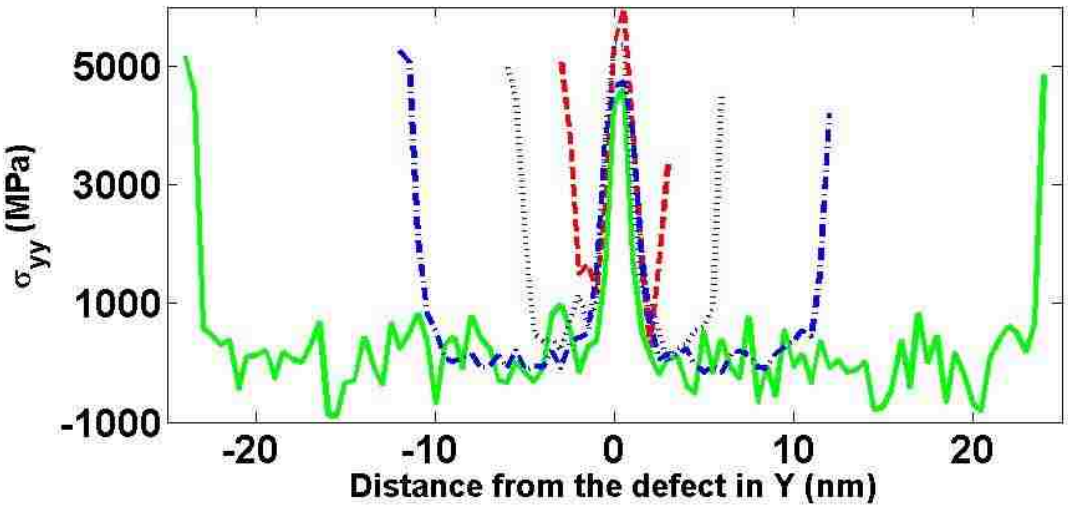

Figure 7-16 Discrete islands $\Delta\sigma_{yy}$ stress distribution for models L_y=6nm, L_y=12nm, L_y=24nm and L_y=48nm are shown with dashed, dotted, dashed-dot and solid lines, respectively

In Figure 7-17 below, a closer view for the stress distribution for the two systems with L_y=6nm and L_y=12nm is given. For these systems the maximum $\sigma_{yy,virial}$ is ~5.9GPa for L_y=6nm system and ~ 5.4GPa for the L_y=12nm system which are close to the smallest model discussed above and higher than the respective periodic islands (L_y=3nm case).

Looking at the plots presented below, we see that as the systems have shifted from periodic islands to discrete ones, the localization behavior existed. However, peak stress values rose up from 4.6GPa to 5.9GPa for the models size up to L_y=12nm. The tensile increase can be attributed to the high tension observed at the edges. During coalescence film will be strained to close the defect at the center, while it is also being strained at the edges due to the edge interactions with the substrate. Therefore the islands are in a higher tension state in overall.

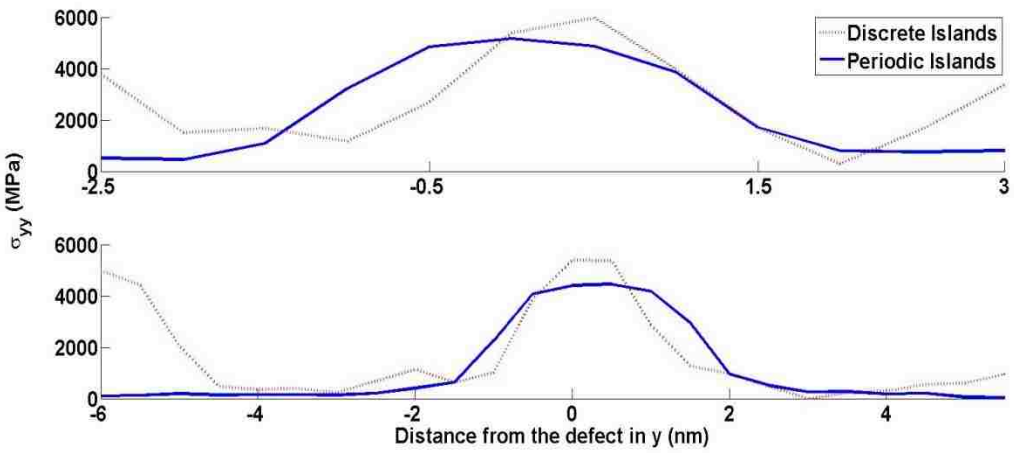

Figure 7-17 Delta stress ($\Delta\sigma_{yy}$) average at the end of the coalescence processes for system L_x=3nm, L_y=6nm (top) and system L_x=3nm, L_y=12nm (bottom) are shown for periodic islands (solid) and discrete islands (dotted).

This conclusion also revealed us that substrate interactions play a crucial role in coalescence as well. Because, as we see in the figures above, the tensile stress values computed at the island edges are comparable to the peak stress values. The coalesced region initially has two edges facing each other. Therefore; besides the cohesive forces between Au atoms on both sides substrate interactions also play a role in coalescence of the islands.

On the other hand, the biggest system with L_y=48nm had peak values at the center which is around 4.6GPa, being less than the smaller discrete island models but close to the periodic islands' average peak value (see Figure 7-16). This shows that the L_y=48nm long film started to behave like a periodic film. In order to get find out the transition size where the film started to behave like a periodic film we run the simulation for the L_y=24nm model which we did not consider at the beginning for the discrete islands. The average delta stress plot is given in Figure 7-16, showing that the transition to periodic island behavior started at an earlier size since the peak stress was found to be around 4.7GPa which is significantly lower than the other smaller discrete island models. In fact, when we compare the periodic and discrete island simulations for

the Ly=24nm case, we observe even a lower tensile stress at the localization region (see Figure 7-18) which also supports our conclusion about periodic behavior at size 24nm and higher. More simulations of intermediate sizes between 12nm and 24nm are required to find out the transition size.

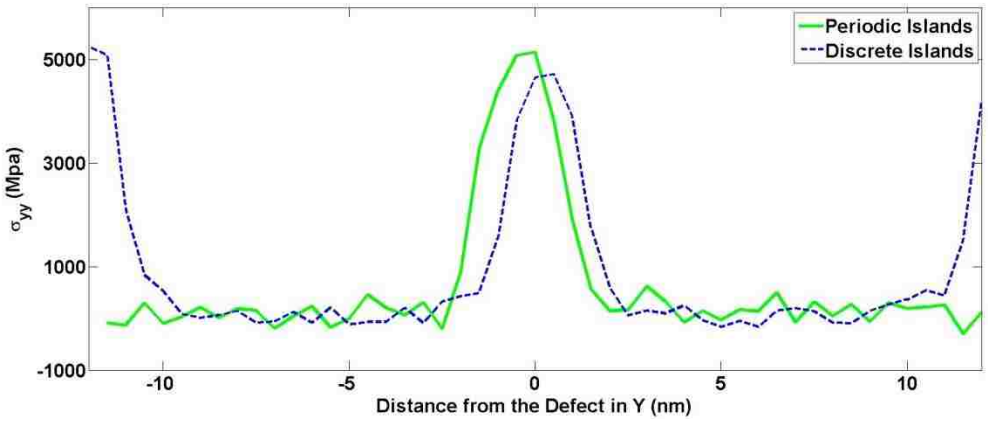

Figure 7-18 Stress distribution for Periodic island versus Discrete Island cases of L_y=24nm models.

The localization width is again found to be independent of size being 2.4nm in average for the discrete islands which is %15 percent less than the periodic island counterparts. This can be explained with the sliding mechanism which may have occurred during coalescence which is less like to occur at the periodic islands. The lower tensile stress might also be related to this mechanism as well.

Lastly, we applied the alternative first neighbor distance analysis again in here where we used Hooke's law as given in Section 6.1 to obtain the stress value. Figure 7-19 below shows that periodic and discrete island spacing at the end of the simulations produced similar results in terms of peak separation distance and overall distribution of the neighbor spacing.

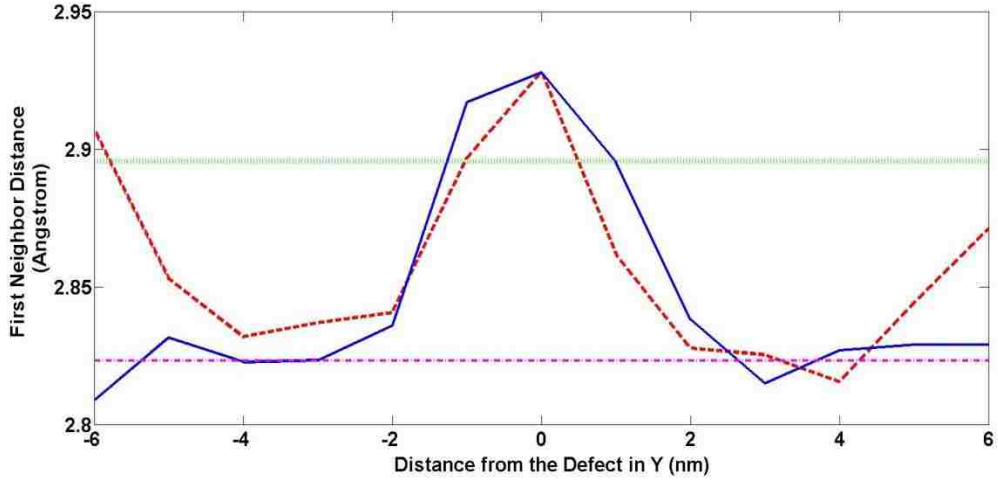

Figure 7-19 First neighbor distance distributions for periodic (solid) and the discrete (dashed) island systems of L_x=3nm and L_y=12nm are shown together with the full single island spacing (dash-dot) and the Au bulk spacing (dotted)

It was computed above in the first part of this chapter that the full film was in compression at an amount of 4.7GPa with respect to bulk. The peak value for the discrete island is $d_{discrete}$= *2.928* Å which corresponds to a strain of 1.11% with respect to bulk. Substituting this value into Eq. (6-2) yields 2.1GPa of tensile stress. For the case where we take the full film as the reference, the strain amount is 3.7% between the full film and the coalesced discrete island. The corresponding stress using Eq. (6-2) is found to be 7.1GPa. The corresponding delta stress computed via MD was 5.4Gpa as summarized in the Table 4 below.

	Full Film Stress	**Delta Stress Center ($\Delta\sigma_{yy}$)**	**Delta Stress Edge(Lower/Upper)**
MD Virial Stress Definition	**-4.5 GPa**	**5.4 GPa**	**4.98/0.95 GPa**
First Neighbor Distance Approach	**-4.7 GPa**	**7.1 GPa**	**5.6/3.2 GPa**

Table 4 Comparison table of the stresses computed via two approaches for L_y=12nm case.

We can also check for the edge stress values computed via two methods. Virial stress values are retrieved from the data as given in Table 4 for both upper and lower halves of the islands. The corresponding strain amounts read from the first neighbor plot above are 2.907 Å and 2.871 Å for the lower and the upper halves, respectively. The corresponding $\Delta\sigma_{yy}$ stresses for the upper and the lower halves are found to be 5.6GPa and 3.2GPa, respectively.

The stress values given in Figure 7-16 and Figure 7-17 above are the delta stress values computed with respect to the full film stress values obtained previously where we did not have any edge effects therefore any tensile jumps. Below in Figure 7-20, we have presented the full single island stress before defect was introduced, and the delta stress with respect to it after coalescence is completed for the L_y=12nm long discrete islands. This figure shows that the stress values in the non-defected forms of the periodic and the discrete islands are quite the same with exception that the discrete islands experience tension at the ends which also affects the far field stress making it slightly more tensile than that is observed in the periodic islands.

The edge effect has also been observed in the displacements analysis done for both ends of the islands. It was found that islands were pulled back (i.e. extended outwards) 0.3-0.5 Å on both ends, rather than sliding towards each other. Similar behavior was observed during preliminary works, where Au islands on Au were also simulated. In those simulations, Au islands moved a bit away from the defect right at the beginning of the coalescence simulations and did not coalesce after 100ns. Besides the edge effect, this result for Au film on Au substrate was also associated with the strong interaction at the similar materials interface and the perfect epitaxy of Au surface atoms with the underlying Au atoms.

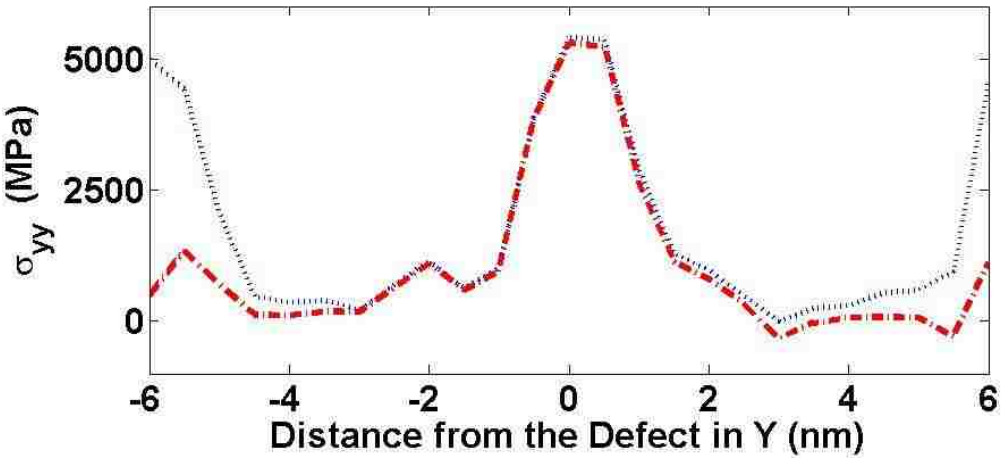

Figure 7-20 Delta stress values for the L_y=12nm discrete island system, computed with respect to the full film stress (dotted) and the single island stress without defect (dashed) are shown together.

To sum up, we can say that stress localization occurs in both systems regardless of the system size. Peak stress values are independent of the system size and geometry, but it changes with periodicity where it goes higher for the discrete islands. Same for the region width, it does not change with size but narrows when periodicity is removed. However, for the discrete islands there is a size limit, after which systems start to behave like a periodic system. The first neighbor distance calculations for the stress also yielded similar qualitative results.

Chapter 8 Stress Evolution During Post-Coalescence Film Growth

Coalescence simulations for the highly characterized Au monolayers have shown stress localization formation around the defect which did not relax for further runs that were relatively long simulations in MD time scale. It was discussed in Section 6.1 where early stage stress evolution was studied and also in the literature (Section 4.4.6) that misfit dislocation mechanisms play a major role in relieving the stress accumulated in the film during hetero-epitaxial growth. The lattice misfit defines the critical thickness where misfit dislocations start to grow.

One other mechanism is the diffusion of atoms into the grain boundaries which is reported to yield compressive stress/tensile relaxation (see references included in Section 4.4.2). Although the Au film is a single crystal without grain boundaries, the atom incorporation into the film layer can be considered in a similar manner.

In this chapter, we resumed the deposition process onto select systems, which coalesced fully, to see the change, if any, in the stress state of the film and the morphological changes of the thickening film. The main interest was on whether the localization was removed or still maintained after deposition. For this purpose we selected systems 3x12nm and 3x24nm (named as Model A and Model B, respectively in this chapter). Model A is the reference model mainly used for deposition simulation, but Model B is also included as a supportive work. Depositing atoms are sent randomly onto the coalesced monolayer at the same rate as used during monolayer formation process. (i.e. 1 atom/3ps)

8.1 Stress Evolution during Early Deposition Steps

Initial observation during depositions was the incorporation of the Au atoms which were deposited onto the localization region into the film layer (see Figure 8-1). This verifies what was reported in the literature as covered in Section 2.4 where it says defected regions are energetically more favorable for nucleation.

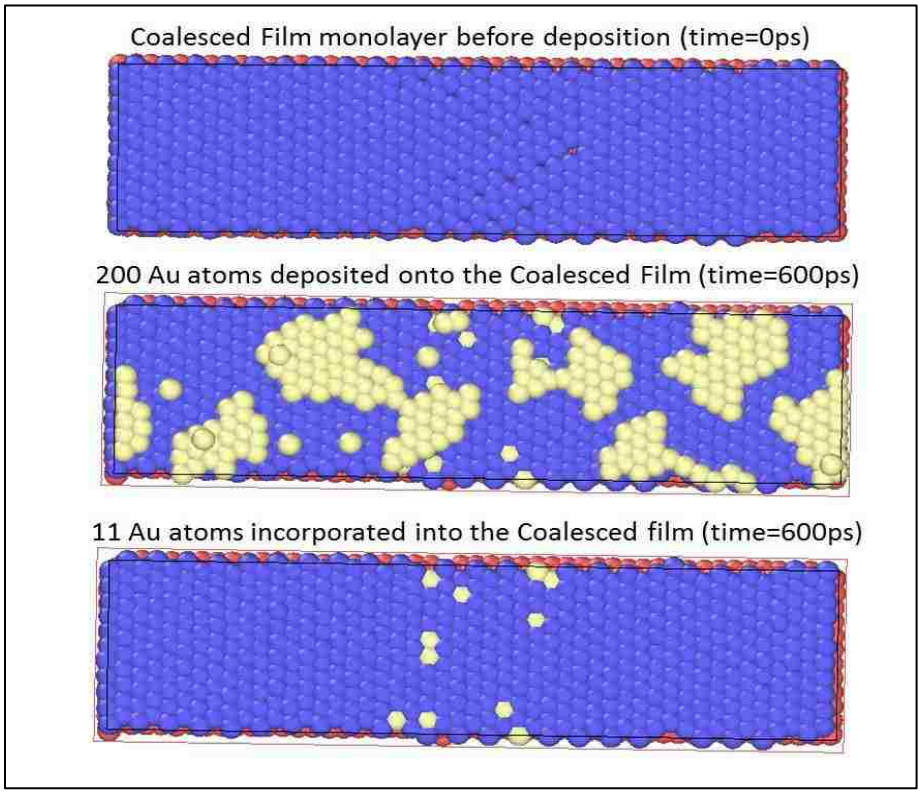

Figure 8-1 Bare coalesced film layer before deposition (top) and the system after deposition of 200 Au atoms (middle) are shown. Au atoms on the coalesced film monolayer are made invisible to show the incorporated Au atoms (yellow) into deformed region (coalesced region) of the Au film monolayer (bottom).(Au film monolayer atoms are shown in blue, underlying Ni atoms are shown in red)

In Figure 8-1 above the coalesced film is shown before deposition where the deformed hexagonal structure can be seen around the stress localization region at the center. After 600ps, deposition of 200 Au atoms is completed and at this instant the monolayer with the incorporated Au atoms is rendered making the upper layer Au atoms invisible, which are shown in middle and bottom images in Figure 8-1, respectively. The number of incorporated atoms incorporated into the stress localization region which was deformed after to coalescence is the same as the number of atoms that were removed in the process of defect formation. As explained in the procedure chapter previously, a line of Au atoms (there are 12 atoms in a line for L_x=3nm systems) were removed to obtain a horizontal highly characterized linear defect in the middle of the film layer which was then set to run for coalescence. The atom incorporation into the film layer starts at the very first steps of deposition process and it is very fast. The adatoms falling onto the far field regions cannot incorporate into the film layer, rather they start forming the second monolayer. However, at later stages of deposition they are observed to replace the initial film layer's atoms which do not change the film structure. Figure 8-1 bottom image also shows the healing in the hexagonal structure of the film when compared to the disordered localization region in Figure 7-6.

The evolution of stress in the film layer is in the form of a tensile relaxation which continued towards compression as seen in Figure 8-2 and Figure 8-3 below. During the initial stages of deposition where the atoms start forming discrete islands on the first monolayer, relaxations occur reducing the tensile stress in the localization region as expected due to atom insertion into the film. However, the film goes into a high compression in overall.

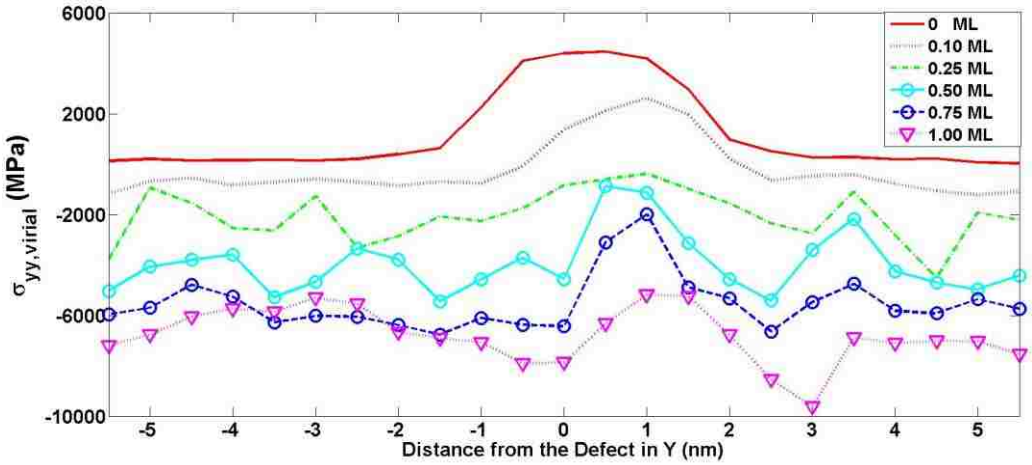

Figure 8-2 Stress (σ_{yy}) evolution during the deposition onto Model A is shown for the starting state where 0 monolayer (ML) deposited, i.e. bare coalesced film (solid) and for the subsequent deposition times for 0.10(dotted), 0.25(dash-dot), 0.50(solid-circle), 0.75(dashed-circle) and 1.00(dotted-triangle) monolayers.

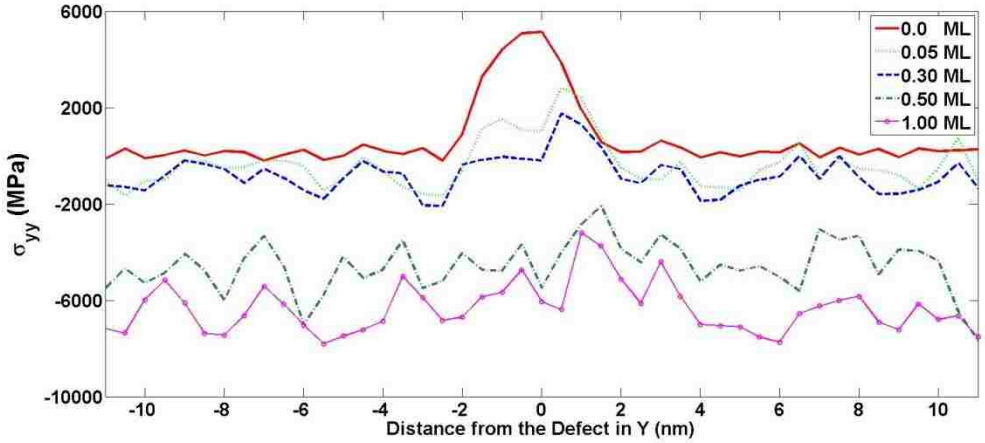

Figure 8-3 Stress (σ_{yy}) evolution during the deposition onto Model A is shown for the starting state where 0 monolayer (ML) deposited, i.e. bare coalesced film (solid) and for the subsequent deposition times for 0.05(dotted), 0.30(dashed), 0.50(dash-dotted) and 1.00(solid-circles) monolayers.

The deposition image given for Model A in Figure 8-4 helps to understand the significant compressive stress generation over the film during the deposition process. As seen in the figure, there are formations of discrete islands which also try to incorporate into the film to reduce the interatomic distance to increase their equilibrium electron charge densities, similar to what is

observed in metal surface atoms which experience surface stress due to the reduced electron density with respect to the bulk atoms. This results in increase in compressive stress in the underlying film as given in the evolution plots above. Compressive stress formation continues till the second layer is formed as also seen in the figures above.

Tensile relaxation or compressive stress generation is commonly observed for FCC metals including Au at room temperature after coalescence stage of film formation process as given in Figure 1-3.Simulation results reported compressive stress generation in the second layer formation during FM Type of film growth [44]. Experimental findings also support this result such that sliding of nucleated islands over the film can also cause compression [13].

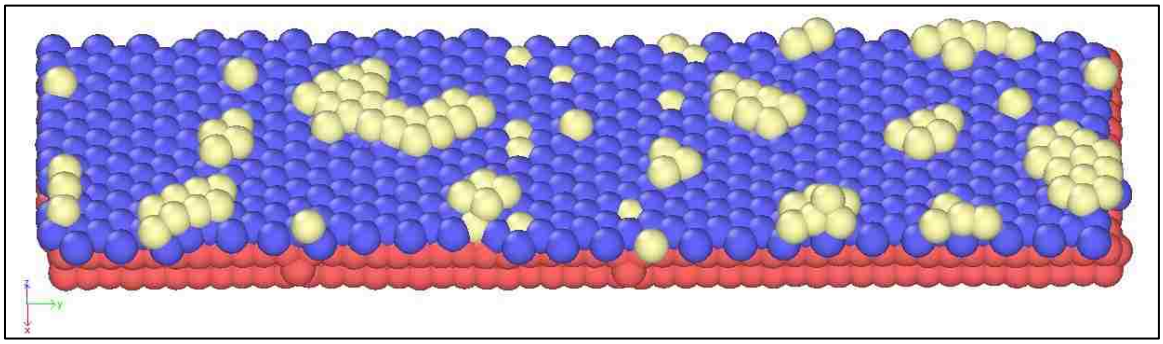

Figure 8-4 Image captured during deposition process onto Model A. which corresponds to ~20% ML coverage shows independent 2D clusters and the incorporated atoms into the first ML at the center.

The first neighbor analysis for Model A is performed and results show the tensile relaxation in the stress localization region more clearly. As seen in Figure 8-5, towards the completion of the monolayer over the coalesced film, the spacing distances gradually drop to the same values observed in the fair field regions. Although the drop in tension is qualitatively consistent with the MD computations (also see Figure 8-10), tendency towards compressive state

observed in MD results does not appear in first neighbor spacing plots for the coalesced monolayer.

For further deposition, the first neighbor spacing curves for the coalesced film layer display a stable behavior with the exception that at the upper half (y>0) there is an increase in neighbor spacing (see Figure 8-7).The images in Figure 8-8 which belong to the 1.9 ML instance show that those atoms from the first deposited monolayer have been replaced with the lower coalesced layer atoms in the region where higher spacing is recorded.

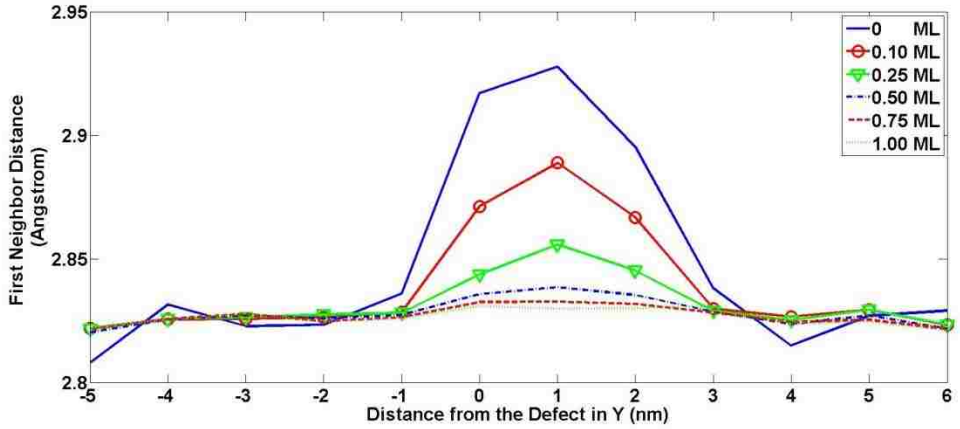

Figure 8-5 First neighbor distance distributions are shown for Model A at the initial coalesced film (solid) and deposition stages for 0.10(solid-circle), 0.25(solid-triangle), 0.50(dashed-dot), 0.75(dashed) and 1.00(dotted) monolayers of deposition.

Compressive stress formation continues till the second layer is formed as also seen in Figure 8-2 and Figure 8-3 above. After the completion of the first layer it starts to relax at some locations showing tensile stress generation as deposition continues, as shown in Figure 8-6.

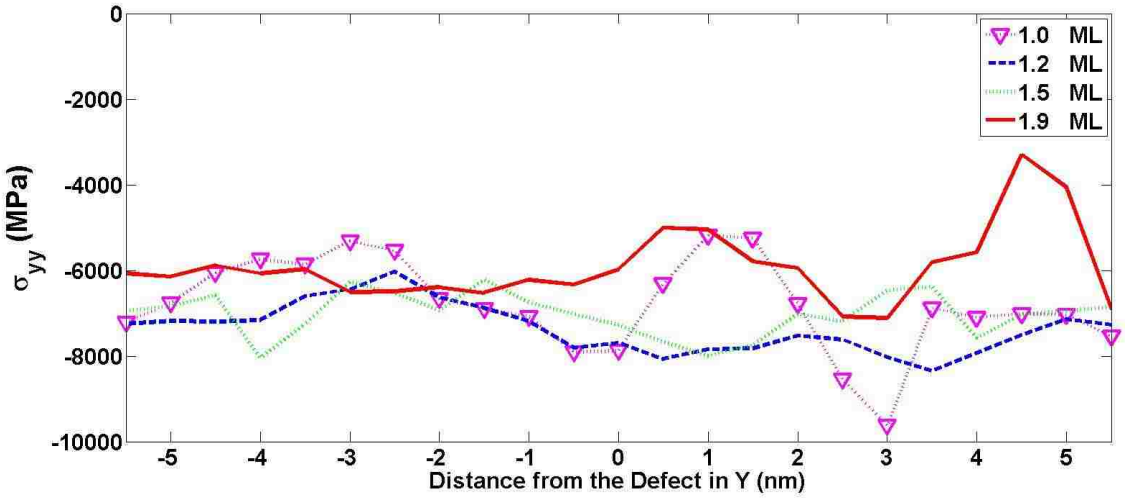

Figure 8-6 Compressive relaxation after completion of one layer deposition is shown. Curves are for deposition instances of 1(dotted-triangle), 1.2(dashed), 1.5(dotted) and 1.9(solid) monolayers on Model A.

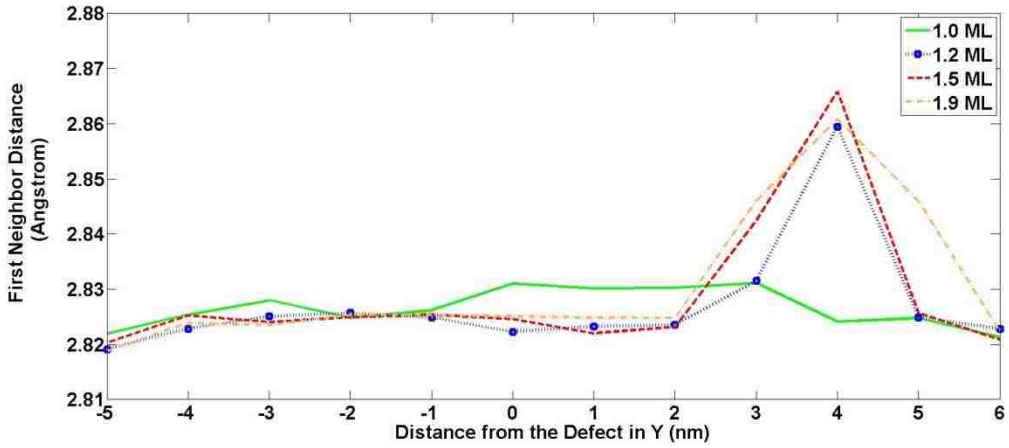

Figure 8-7 First neighbor distance distribution for ongoing deposition after completion of 1 ML (solid) is given for 1.2 (dashed-circle), 1.5(dashed) and 1.9(dash-dot) ML deposition instances.

Atom number check for the coalesced film layer shows that it recovers its original number of atoms of the full film quickly during deposition. However, it starts losing some, where at the end of 1.9ML it has 8 less atoms than the full film form (see Figure 8-10). This would cause an increase in the average first neighbor spacing due to lower atom density in the layer in

those regions. In the region with less atomic density compressive stress is also relieved to a certain extent which is also observed in Figure 8-6 above.

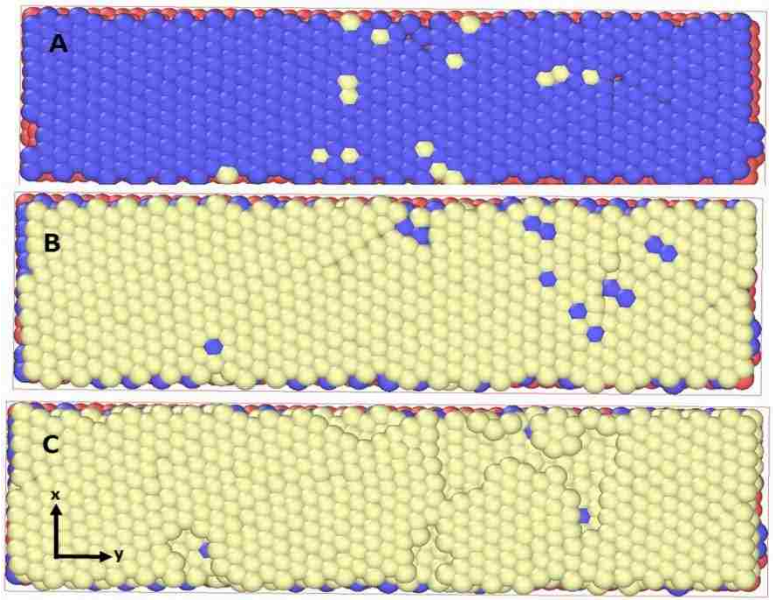

Figure 8-8 Top view of Model A for the three layers after deposition of 1.9 ML is shown in A, B and C which belong to the coalesced film, the first deposited ML and the second ML, respectively (in the picture Ni substrate are red, coalesced Au film monolayer are blue and the deposited Au atoms are yellow).

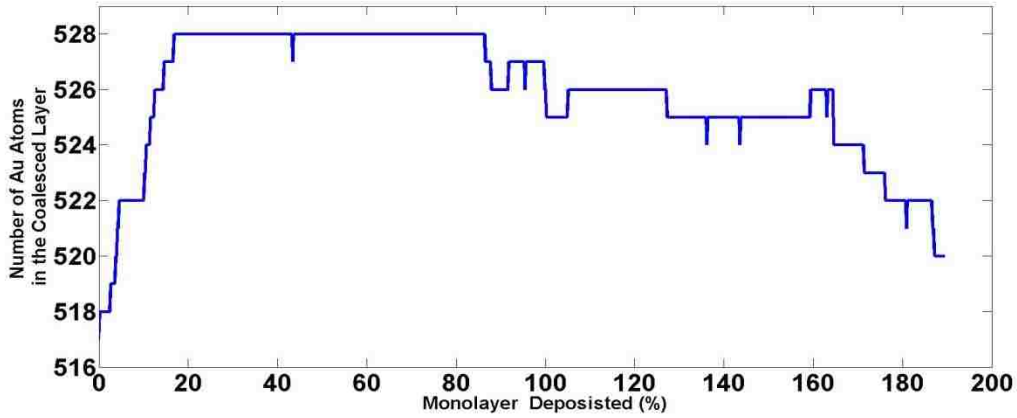

Figure 8-9 Number of Au atoms in the coalesced film layer is shown, where full film total is 528 atoms.

Qualitatively, peak values for $\Delta\sigma_{yy}$ (difference with respect to the full film without defect) component of the virial stress, which was computed to be at the center of the stress localization region in the vicinity of the defect, reduce gradually from 4.5GPa of the coalesced form to 2.6GPa, -0.4GPa, -0.9GPa, -2GPa and -5.2GPa for 0.10, 0.25, 0.50, 0.75 and 1.00 ML deposition stages, respectively for Model A (L_y=12nm) (see Figure 8-2). Corresponding peak stress values computed via first neighbor spacing values from Figure 8-5 are 7.1GPa for the coalesced film and 4.4GPa, 2.2GPa, 1.1GPa, 0.7GPa and 0.4GPa for 0.10, 0.25, 0.50, 0.75 and 1.00 ML deposition stages, respectively (see Table 5). Figure 8-10, shows better that although the numbers are not overlapping, the qualitative responses can be considered similar.

	Bare ML	**0.10 ML**	**0.25 ML**	**0.50 ML**	**0.75 ML**	**1.00 ML**
MD Virial Delta Stress	4.5	2.6	-0.4	-1.1	-2.0	-5.2
First Neighbor D. results	7.1	4.4	2.2	1.1	0.7	0.4

Table 5 Table showing the delta peak stress results computed at various monolayer (ML) deposition instances using MD virial stress definition and First Neighbor Spacing values, units are in GPa.

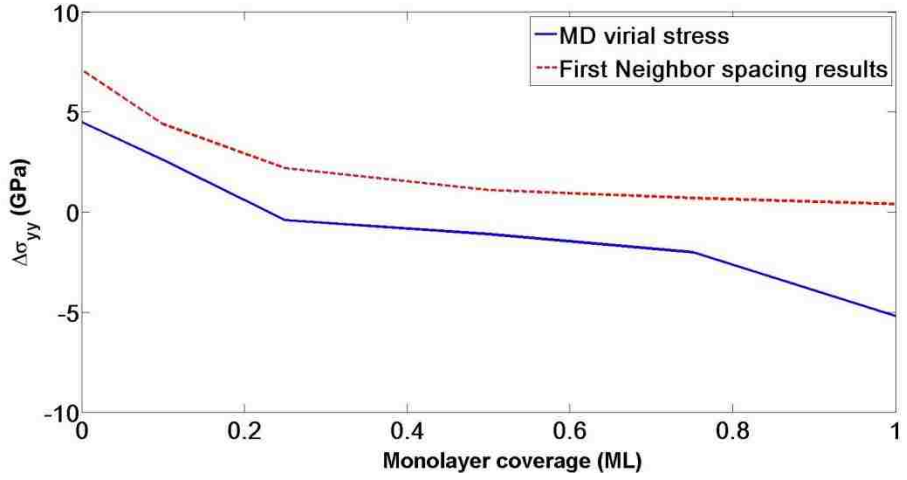

Figure 8-10 Tabulated values in Table 5 above for MD virial stress and First neighbor spacing are plotted for comparison.

8.2 Misfit Dislocation Formation and Comparison to Predictions from Theory

We continued deposition up to 8 ML in Model B to see the stress evolution in thickening films. Tensile peaks were observed in both first neighbor plots and MD stress plots for this model (see Figure 8-11). In order to elucidate the reason for the multiple tensile peaks observed in Model B we applied centro-symmetry analysis for the model where the number of nearest atoms for each atom is computed for the film layers. This method is utilized to detect crystallographically defected regions like misfit dislocations or in the atomic crystal structure. The colored centro-symmetry image given in Figure 8-12 clearly shows the misfit dislocations where atomic order becomes more defected as colors go from blue to red.

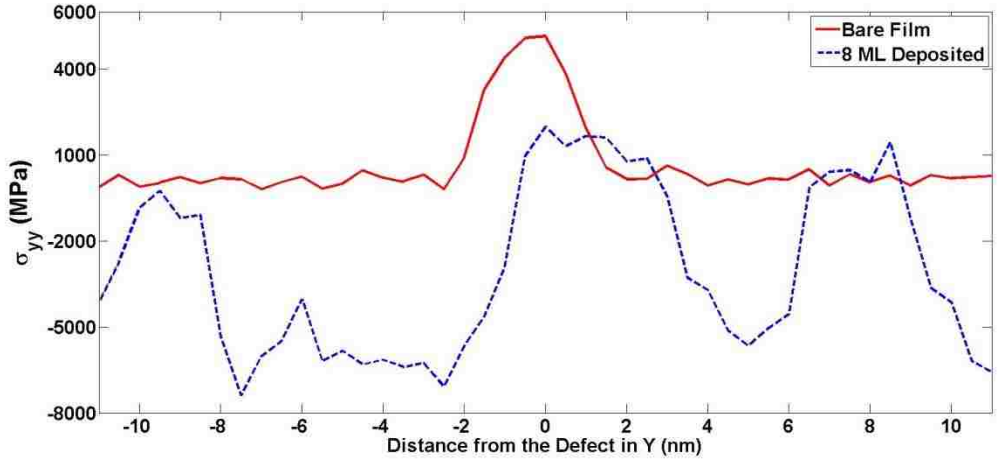

Figure 8-11 Stress distribution on the coalesced film before deposition (solid) and after 8ML of film deposition (dashed) are shown.

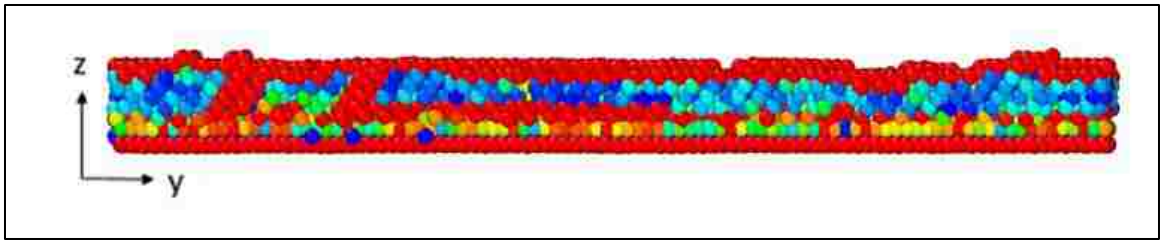

Figure 8-12 Centro-symmetry image for Model B showing the misfit dislocations started from right above the initial film monolayer. Disorder increases as color goes from blue to red.

As computed in Section 6.2 the critical thickness was computed to be $\boldsymbol{t_{critical}}$**=11.6Å** and Au monolayer thickness derived from the density distribution analysis was found to be $\boldsymbol{t_{monolayer}}$**=2.0 Å**. This corresponds to around 6 ML of Au film which is also shown in Figure 8-12. This figure also explains the reason behind tensile recovery in the film such that the accumulated compressive stress is relieved by misfit dislocations which gave rise to tensile stress generations at the dislocation regions.

In a crystal structure slip planes on which dislocation form are the planes which possess the highest planar density of atoms which corresponds to the widest spacing plane. The direction in which defect propagates is the one with highest linear density. Thus in an FCC system {111} is the slip plane with <110> being the slip directions (see Figure 8-13).

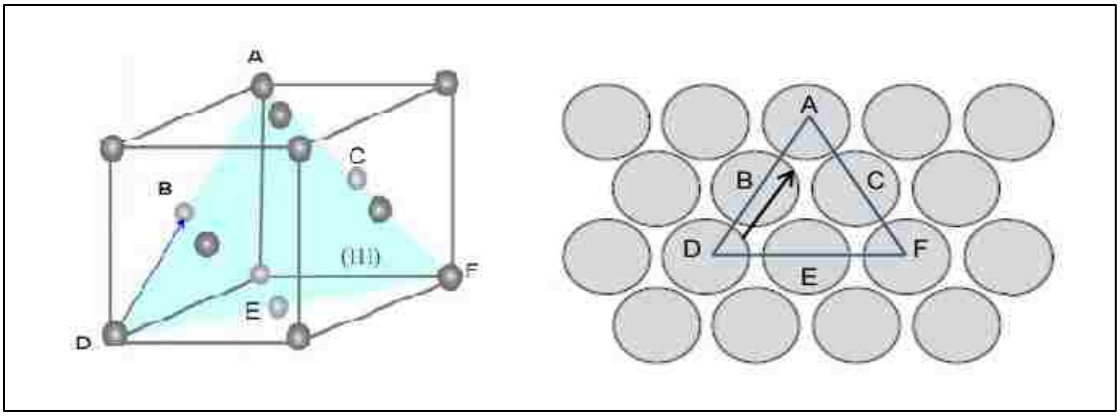

Figure 8-13 Slip plane (left) and Slip direction (right) for an FCC crystal are shown. [Pictures are adapted from MIT OpenCourseWare]

The centro-symmetry image given in Figure 8-14 below for the first monolayer deposited onto the coalesced layer verifies that the dislocations are introduced on the slip directions as given above.

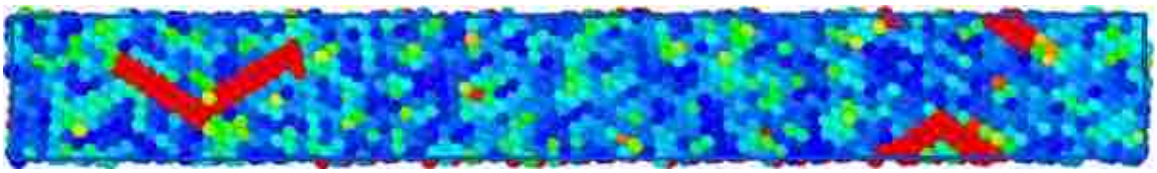

Figure 8-14 Centro-symmetry distribution showing the dislocations started on the first monolayer of Model B.

Due to the shortcoming of periodicity the misfit dislocations are not captured fully since the repeat length could be greater than our model size. This work shows the formation of the dislocations but in a bigger system with longer deposition providing a thicker film would enable us to capture dislocation evolution minimizing the simulation artifact. Similar work has been carried out by Pereira and Silva [39] where they deposited Pd on Au (001) substrate. In their work they simulated a larger model with 13.4x13.4 nm size in XY plane and continued deposition up to 15ML on top of Au substrate. Pd film growth on Au (001) substrate started to grow dislocations after 8th ML. They obtained a better map of the dislocations which grew in the film leading

tensile relaxation as shown in the image below .There it shows the cross-section views of different layers of the Pd film with the colored Ackland-Jones method (AJM) values after completion of the 15th ML. AJM shows the crystal structure which each atom belongs to. It clearly shows the dislocation network; where on <110> slip directions red atoms are changed into HCP structure, and the greens still being in FCC.

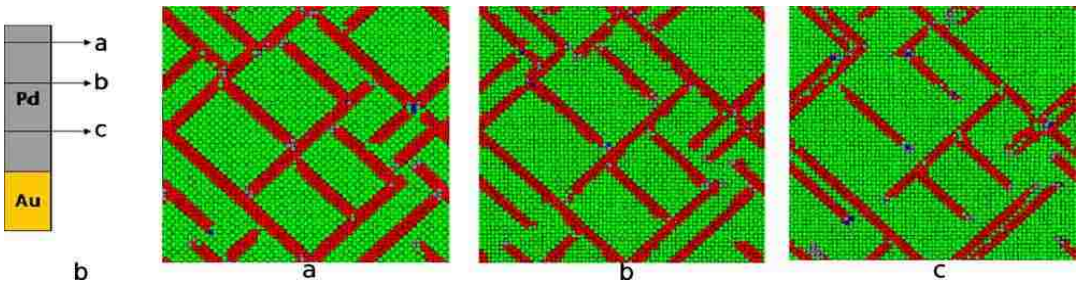

Figure 8-15 After 15ML of Pd film depositon on Au (001) substrate, cross-section views of AJM distribution for different layers are shown in a, b and c for 10,6 and 3 MLs, respectively. [39]

Chapter 9 Conclusion and Future Work

Stress evolution in early stages of thin metal film growth has been studied in atomistic scale using molecular dynamic methods with particular interest on spatial and temporal distribution of the stress over the thin films having dissimilar material interface with the substrate.

Stress evolution and distribution was modeled for the coalescence stage of film formation process where a single, highly characterized linear defect was manually formed in the Au monolayer which was previously deposited on the Ni substrate. Stress manifestation during early film formation and subsequent deposition on the coalesced film stages were also studied.

In Chapter 6, we analyzed the stress formation during the controlled growth of Au monolayer which started as a small 2D cluster and grew to a monolayer. A sharp interface with no intermixing was obtained for Au deposited onto the Ni (001) substrate due to the high lattice mismatch and the positive heat of mixing values of both metals. As the island grew larger, the ratio of the edge atoms (which are under tension due to surface interactions) to the total number of atoms in the cluster went down thus the compressive state became more significant which was due to the lattice mismatch between Au and Ni. The compressive stress attained at the full film monolayer was 4.5GPa.

In hetero-epitaxial film growth there is a critical thickness where misfit dislocations are triggered due to the misfit stress accumulated in the film. That was computed to be 11.6Å which corresponded to 6 ML of thin film thickness as also obtained in the simulations. This result indicated that due to the high lattice misfit between the metal pair, the dislocation would start in the sixth monolayer.

Chapter 7, involving the major part of this study, elucidates the stress distribution evolution during coalescence process of the manually formed linear defect on the Au monolayer of different geometries. In the first part, periodic islands of different sizes were simulated for coalescence. The most significant finding of the simulations was that dissimilar material interfaces induce a significant effect on stress distribution in thin films that is the stress localization which was observed around the defect region during coalescence and in post coalescence regime as a residual stress.

Localization region extended to a certain width, which was independent of the system size, being around 2.7nm. Similar to the width, the delta peak stresses observed in the localized region were also observed to be independent of size, ranging between 4.5-5.1GPa. However, the far field stress was computed to be dropping for increasing system sizes down to the full film, pre-coalescence stress levels.

In Figure 7-6, we have seen that the stress and morphology after coalescence was not also uniform in x direction. We performed a 2D stress analysis for bot x and y components of the stress together with the hydrostatic stress distribution analysis for the 24x12nm film monolayer to capture the complete behavior of stress distribution evolution during coalescence. We have seen the change in stress in the direction parallel to the defect orientation and verified the existence and size of the stress localization region using the combination of other stress components as well. Having the stress distribution contours in hand, that would be helpful to apply deposition over this system to see how stress localization sites affect the spatial distribution of the deposited atoms.

The coalescence simulations were repeated for the discrete Au monolayer islands, which were the counterpart of the periodic island models with the exception of periodicity in Y direction. It was found that there was ‘stress localization’ around the defect similar to the periodic

island case. However, the peak stresses and the width displayed different behaviors with changing system sizes, such that up to 12nm, the peak stresses were in the range 5.4-5.9GPa and widths were computed to be around 2.4nm and both were independent of the size. Peak stresses for this size range were raised up around 25%, while the width size reduced around 12% with respect to the corresponding models in the periodic islands case. The overall rise in tension in the film including the peak stress at the center is attributed to the penetration of the edge effect from the ends towards the film center which is in tension. The tension at the edges was independent of the system size and computed to be around 5.1GPa of tension. The reduction in the width could be due to sliding of islands towards each other to close the defect.

For discrete islands we also modelled 3x24nm and 3x48nm systems, the latter being the largest system modelled in this work. They yielded a lower peak stress of around 4.6 GPa which was distinctly below the smaller discrete islands' peak stress average. However, it was close to the range of periodic island peak stress values. Therefore we concluded that the discrete islands start to behave like periodic islands after a certain size. As a completion work for the future, the transition size can be determined via further simulations of intermediate sizes between 12nm and 24nm.

Different coalescence mechanisms are proposed in the literature. Sliding is one of those mechanisms which is likely to occur when there is a weak interaction at the interface causing low traction. It was remarkable in this work that although having conditions favorable for sliding (i.e. sharp interface without intermixing, big lattice mismatch and non-epitaxial interface); not even the smallest model of discrete islands slid for coalescing where it was even found that they were extended outwards at the same amount on both ends, tended to further wet the Ni bare surface during coalescing for all models studied.

The other important finding of the coalescence simulations is related to the temporal behavior of stress distribution in thin films. That is, the stress reaches to its maximum when the defect fully heals and it does not relax after that. We verified this conclusion of stable residual stress for all systems by running those for hundreds of nanoseconds longer after completion of coalescence. This is crucially important when you consider an application utilizing thin films for critical parts. It may not be a single layer of film for now, but even for the uppermost layers of thicker films, where deposition will be ended; it is likely to have coalescence events to take place to close the incomplete layers or surface defects. Thus the localized stress shown in this work may exist as a residual stress on the parts. As we continue to decrease system size for various technological devices dependent on thin film architectures, film dimensions are correspondingly decreased, including thickness. Thus, effects in a film due to coalescence events near the surface of a film become more pronounced.

From a different point of consideration, the experimental data obtained via curvature measurements cannot explain the stress distributions down to the atomic scale accessed in here. The stress-thickness plots show the overall stress evolution in the film without referencing the critical locations with maximum stress. In other words, for the models simulated in this work, the curvature plots would show a decreasing overall stress down to a few MPa, but would not be able to explore the peak stress at the coalescence regions reaching up to several GPa.

Lastly, having the localized residual stress on the coalesced films, we deployed deposition on to select periodic islands. The initial observation was that the adatoms were absorbed into the film layers in the stress localization region, such that the number of atoms diffused into the layer were the same as the atoms that were removed manually to form the defect. As a result, we observed healing in the deformed hexagonal structure of the film in the localized region. However, as mentioned above stress varies in x direction; therefore, it would be a better

practice to simulate deposition over a larger system like 24x12nm is given in Figure 7-6, to fully understand the incorporation process in to the film layer.

The major outcome for the deposition was that, starting from the very first atom the tensile peak in the localized region dropped down. The first neighbor spacing analysis for the deposition work showed this gradual tensile drop in the localized region very clearly while having no significant changes for the far field regions. MD simulations also produced parallel results in terms of tensile drop, but they also yielded significant compressive stress, which increases up to completion of the first deposition ML. That can be due to the tendency of the deposited adatoms on the surface to incorporate with the underlying film atoms to compensate their electron charge density loss due to having much less number of neighbor atoms on the surface than the bulk atoms. This conclusion was also verified by the slight relaxation in compressive stress as the second deposition layer starts to grow. This can be explained as follows; the atoms in the first deposition layer will be surrounded fully in the xy plane and also will start to be interacting with the upper layer atoms which will break the intensity of their tendency to squeeze themselves into the coalesced film layer, thus relaxing the compressive stress or at least stop further increase in the compression.

Different than the first neighbor analysis results, MD simulations revealed a compressive stress increasing as deposition continued towards a thicker film. This was similar to what was found in relevant experimental studies [1], [45]. Seel et al. have also reported compressive stress generation during deposition process due to the sliding of islands over the film layer up to a certain coverage limit [14].

The deposition process is different than the coalescence process in terms of simulation kinetics and thermodynamics. Coalescence is actually an equilibrium run where we set the system run for equilibrium at the constant temperature of 300K. However, during deposition every 3ps

we introduce a new atoms with a certain velocity into the system affecting the system temperature and thus velocities and therefore interactions. System tries to equilibrate itself before the next atom comes in. It was reported in the literature [2] that temperature and the deposition rate are the two most important parameters affecting thin film structure. The deposition rate used in the simulations is 1 atom per 3ps which corresponds to 48 meters of Au film deposition in just 1 hour, which is relatively fast. Also, it was shown experimentally for layer by layer growths that when deposition is interrupted relaxation occurs in films and stress is recovered back to where it was left before interruption as deposition restarts [45]. Therefore, more care should be exercised while working on the stress computed during deposition.

Having said that, it might be helpful as a future work, to repeat the stress evolution analysis for the deposition process at a slower rate and also adding interruption periods to let the system equilibrate after certain ML coverage levels before gathering stress data. This may require longer time of simulations meaning more computational resources to be planned for the future studies but deposition rate was reported to be an important factor affecting the stress behavior of thin films as summarized in Section 4.4.3. Indeed, it may be necessary to consider combining molecular dynamics with some type of kinetic Monte Carlo algorithm to properly address macroscopic time scales. Again, this is a non-trivial endeavor well suited to follow-on research.

The misfit dislocations which started to grow in the Au film layer were not able to be captured fully due to the system size limitations. It was also required to have more layers of film to be deposited to map the dislocation behavior completely. Having the concerns mentioned above, further deposition would help to better understand the stress evolution as the film continues to grow up to at least few nanometers (note that 5ML of deposition corresponds to 1nm thick film) which is required for today's thin film applications.

Atomistic stress is computed via virial method, which accounts the atomic interactions only within a simulation domain. When used to evaluate stress in a local region of an atomistic ensemble, this method has been criticized for its accuracy, but it has been reported that local stress behavior interpreted via virial method is qualitatively correct. On the other hand, quantitative results produced by the virial stress method are shown to be poor in accuracy around high stress gradient region like surface defects. Taking these concerns into consideration, we applied an alternative approach to compute stress on the film using first neighbor spacing data for the film atoms where local strain was calculated via the difference between the nearest space distances. Strain is then converted into stress using Hooke's law for films with 111 plane sitting on a 001 substrate surface with plane stress assumption. The results were perfectly matching the MD counterparts qualitatively (i.e. occurrence of stress localization around the defect, residual behavior, etc.). However, quantitatively there was a mismatch where first neighbor distance results were higher in magnitude. This can be attributed to the selected volume which was used to divide (pressure*volume) values computed via MD tool to get virial stress. Atomic volume can be hard to define especially in deformed solids or liquids. We defined volume for the stress analysis bins as the product of their width in x, length in y and an average thickness of the film layer extracted from the density distribution analysis. While the first two dimensions were rigorously defined, the third was not; a rather small value was obtained from density analysis for the monolayer thickness $t_{mono} \sim 0.20$ nm; however, this is a fairly simplistic interpretation of the spatial extent of the film. If the interaction cut-off distance for the interatomic potentials used here ($R_c \sim 0.55$ nm) is instead used as the thickness, computed stress values are more than halved. Therefore, definitions of film dimensions in atomic scale simulations of thin film growth should be considered more carefully as a part of the future work.

However, the outcomes of the virial stress definition, for the surface coalescence of defects, have been shown to be in fairly good agreement with the stress results obtained from

deformation gradient analysis. Therefore local atomistic stress computations can be regarded as a semi-quantitative measure.

The semi-quantitative, atomistic scale stress distribution analysis conducted in this work can be utilized to advance Tello and Bower's work where they developed a finite element model for the stress evolution near grain boundaries of the surface of the growing film islands, using the cohesive zone model [59]. At the outset of research here, a goal was to determine if sub-ensemble averaging of stress in atomic scale simulations could give sufficiently robust answers – quantitatively – to allow comparison to similar results from continuum models based on cohesive zone formulations for describing interaction between free material surfaces across a gap. Tello and Bower performed such work; as is traditional practice with continuum formalisms, they performed all dimensionless simulations. The cohesive zone law they employed is shown below (see Figure 9-1 and Figure 9-2, reprinted from Tello and Bower, 2008), along with a dimensionless plot of their cohesive zone law.

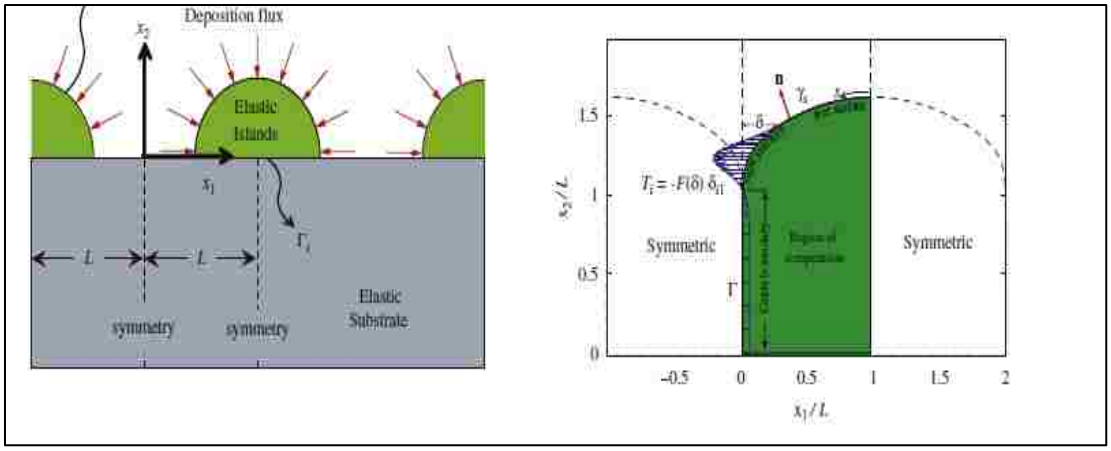

Figure 9-1 Representative geometry of half of an evolving island is shown. The arrows represent the cohesive tractions (reprinted from Tello and Bower, 2008)

In Eq.(9-1) below, σ_m is the maximum traction experienced between free surfaces and δ is the distance between the free surfaces (i.e. the gap size), where zero corresponds to equilibrium contact of the surfaces; lastly, Δ is the position where the peak traction occurs. Tello and Bower used a finite element formalism including this cohesive zone law to model film growth in the Volmer-Weber mode. Examples of stress evolution (again in dimensionless presentation) obtained from their work are shown in Figure 9-3 below.

$$T_i = -F(\delta)\delta_{i1} \text{ and } F(\delta) = \sigma_m \exp\left(1 - \frac{\delta}{\Delta}\right)\frac{\delta}{\Delta} \qquad 9\text{-}1$$

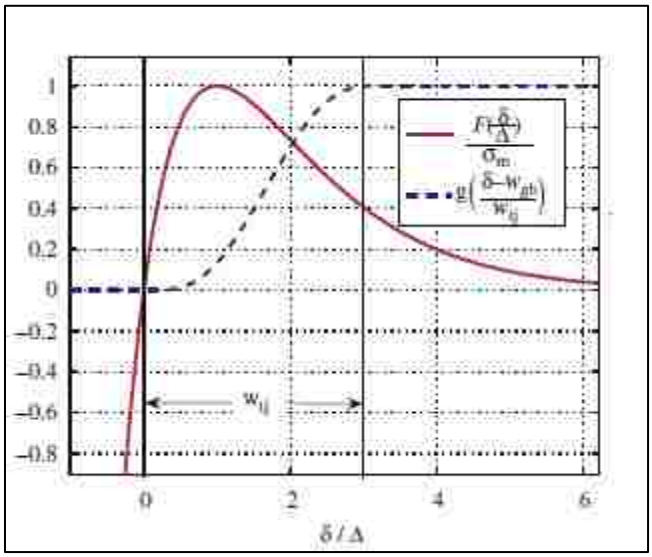

Figure 9-2 Cohesive zone law (solid) and truncation function (dashed)

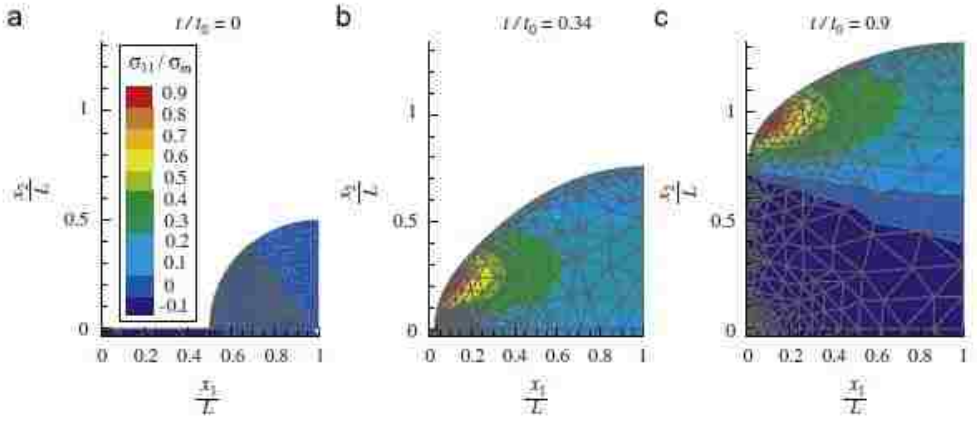

Figure 9-3 Stress evolution of the growing islands for three successive instances

In this study, Au and Ni were taken as the film-substrate pair and certain conclusions are made on spatial and temporal manifestation of stress evolution during and after coalescence of thin film formation and also while under ongoing deposition. The results can be generalized if we use modified interaction potential to obtain weaker/stronger between the film and substrate and in between film atoms. This can also lead to different cases like diffusive interfaces. Different material systems can also be studied other than pure metals. Materials like single and polycrystalline silicon, Al alloys, silicon oxides, etc. are used in integrated circuits or for different applications like barrier films. Stress affects the electron band gap in semi-conductor materials which is very crucial for the reliability of their performance. Therefore, this study would lead us to look into stress evolution in atomistic level in such materials.

Aside from studying the stress evolution in different materials there is another issue to be addressed in this study which is the reliability of the stress computation method used in here, meaning the virial stress method. Hardy stress method is reported to be better in accuracy for the stress computation and it should be implemented and results should be compared to the virial and the first neighbor outcomes obtained in this work.

This study will provide the thin film and small scale mechanical properties community with new interpretations regarding the range of strain and stress present in a sample measured to possess some average stress. We advance that such knowledge will be highly useful to materials reliability analysis as well as fracture initiation analysis. It will also provide the foundation for multiscale formulation of advanced constitutive expressions used in finite element models of materials behavior during thin film growth. Collectively, this study has potential to greatly benefit theoretical descriptions of the mechanical behavior of materials, particularly as manifest in small-scale structures.

References

[1] R. Koch, “Stress in Evaporated and Sputtered Thin Films - A Comparison,” *Surf. Coatings Technol.*, 2010.

[2] L. B. Freund and S. Suresh, *Thin Film Materials: Stress, Defect Formation and Surface Evolution*. Cambridge University Press, 2004.

[3] R. Koch, “The intrinsic stress of polycrystalline and epitaxial thin metal films,” *J. Phys. Condens. Matter*, vol. 6, no. 45, pp. 9519–9550, Nov. 1994.

[4] A. G. Evans and J. W. Hutchinson, “The thermomechanical integrity of thin films and multilayers,” *Acta Metall. Mater.*, vol. 43, no. 7, pp. 2507–2530, Jul. 1995.

[5] R. Koch, D. Winau, A. Führmann, and K. H. Rieder, “Growth-mode-specific intrinsic stress of thin silver films,” *Phys. Rev. B*, vol. 44, no. 7, pp. 3369–3372, Aug. 1991.

[6] D. Winau, R. Koch, A. Führmann, and K. H. Rieder, “Film growth studies with intrinsic stress measurement: Polycrystalline and epitaxial Ag, Cu, and Au films on mica(001),” *J. Appl. Phys.*, vol. 70, no. 6, p. 3081, 1991.

[7] M. D. Rauscher, A. Boyne, S. A. Dregia, and S. A. Akbar, “Self-Assembly of Pseudoperiodic Arrays of Nanoislands on YSZ-(001),” *Adv. Mater.*, vol. 20, no. 9, pp. 1699–1705, May 2008.

[8] Q. Ma and D. R. Clarke, “Stress Measurement in Single-Crystal and Polycrystalline Ceramics Using Their Optical Fluorescence,” *J. Am. Ceram. Soc.*, vol. 76, no. 6, pp. 1433–1440, Jun. 1993.

[9] W. D. Nix, “Mechanical properties of thin films,” *Metall. Trans. A*, vol. 20, no. 11, pp. 2217–2245, Nov. 1989.

[10] S. J. Hearne, S. C. Seel, J. A. Floro, C. W. Dyck, W. Fan, and S. R. J. Brueck, “Quantitative determination of tensile stress creation during island coalescence using selective-area growth,” *J. Appl. Phys.*, 2005.

[11] E. Chason, J. W. Shin, C. H. Chen, A. M. Engwall, C. M. Miller, S. J. Hearne, and L. B. Freund, “Growth of patterned island arrays to identify origins of thin film stress,” *J. Appl. Phys.*, 2014.

[12] S. Plimpton, “Fast Parallel Algorithms for Short – Range Molecular Dynamics,” *J. Comput. Phys.*, vol. 117, no. June 1994, pp. 1–19, 1995.

[13] W. D. Luedtke and U. Landman, “Metal-on-metal thin-film growth: Au/Ni(001) and Ni/Au(001),” *Phys. Rev. B*, 1991.

[14] S. C. Seel, C. V. Thompson, S. J. Hearne, and J. A. Floro, “Tensile stress evolution during deposition of Volmer–Weber thin films,” *J. Appl. Phys.*, vol. 88, no. 12, p. 7079, 2000.

[15] S. C. Seel, J. J. Hoyt, E. B. Webb, and J. A. Zimmerman, “Modeling metallic island coalescence stress via adhesive contact between surfaces,” *Phys. Rev. B*, vol. 73, no. 24, p. 245402, Jun. 2006.

[16] L. A. Zepeda-Ruiz, E. Chason, G. H. Gilmer, Y. Wang, H. Xu, A. Nikroo, and A. V. Hamza, “Understanding the relation between stress and surface morphology in sputtered films: Atomistic simulations and experiments,” *Appl. Phys. Lett.*, vol. 95, no. 15, p. 151910, 2009.

[17] T. Zientarski, “Molecular dynamic simulation of stress development during coalescence of grain in presence of depositing atoms,” in *Crystal Research and Technology*, 2010.

[18] D. Chocyk, T. Zientarski, A. Proszynski, T. Pienkos, L. Gladyszewski, and G. Gladyszewski, "Evolution of stress and structure in Cu thin films," in *Crystal Research and Technology*, 2005.

[19] C.-W. Pao, S. M. Foiles, E. B. Webb, D. J. Srolovitz, and J. A. Floro, "Thin Film Compressive Stresses due to Adatom Insertion into Grain Boundaries," *Phys. Rev. Lett.*, vol. 99, no. 3, p. 036102, Jul. 2007.

[20] T. Zientarski and D. Chocyk, "Structure and stress in Cu/Au and Fe/Au systems: A molecular dynamics study," 2014.

[21] R. C. Cammarata, "Surface and interface stress effects in thin-films," *Prog. Surf. Sci.*, vol. 46, no. 1, pp. 1–38, 1994.

[22] R. C. Cammarata and K. Sieradzki, "Surface and Interface Stresses," *Annual Review of Materials Science*. 1994.

[23] R. C. Cammarata, "Surface stress effects on the intrinsic stress in thin films," *Adhes. Asp. Thin Film.*, vol. 1, pp. 31–54, 2001.

[24] G. C. A. M. Janssen, "Stress and strain in polycrystalline thin films," *Thin Solid Films*, vol. 515, no. 17, pp. 6654–6664, Jun. 2007.

[25] G. G. Stoney, "The Tension of Metallic Films Deposited by Electrolysis ," *Proc. R. Soc. London. Ser. A*, vol. 82, no. 553, pp. 172–175, 1909.

[26] E. Chason, "A kinetic analysis of residual stress evolution in polycrystalline thin films," *Thin Solid Films*. 2012.

[27] G. Abadias, A. Fillon, J. J. Colin, A. Michel, and C. Jaouen, "Real-time stress evolution

during early growth stages of sputter-deposited metal films: Influence of adatom mobility," 2014.

[28] O. Ergincan, G. Palasantzas, and B. J. Kooi, "Influence of random roughness on cantilever curvature sensitivity," *Appl. Phys. Lett.*, vol. 96, no. 4, p. 041912, 2010.

[29] D. Flötotto, Z. M. Wang, L. P. H. Jeurgens, E. Bischoff, and E. J. Mittemeijer, "Effect of adatom surface diffusivity on microstructure and intrinsic stress evolutions during Ag film growth," *J. Appl. Phys.*, vol. 112, no. 4, p. 043503, 2012.

[30] J. A. Floro, S. J. Hearne, J. A. Hunter, P. Kotula, E. Chason, S. C. Seel, and C. V. Thompson, "The dynamic competition between stress generation and relaxation mechanisms during coalescence of Volmer–Weber thin films," *J. Appl. Phys.*, vol. 89, no. 9, p. 4886, 2001.

[31] A. L. Del Vecchio and F. Spaepen, "The effect of deposition rate on the intrinsic stress in copper and silver thin films," *J. Appl. Phys.*, vol. 101, no. 063518, 2007.

[32] R. Koch, "Intrinsic stress of ultrathin epitaxial films," *Appl. Phys. A Mater. Sci. Process.*, vol. 69, no. 5, pp. 529–536, Nov. 1999.

[33] X. Xiao, B. W. Sheldon, Y. Qi, and A. K. Kothari, "Intrinsic stress evolution in nanocrystalline diamond thin films with," 2008.

[34] M. Pletea, W. Brückner, H. Wendrock, and R. Kaltofen, "Stress evolution during and after sputter deposition of Cu thin films onto Si (100) substrates under various sputtering pressures," *J. Appl. Phys.*, vol. 97, no. 5, p. 054908, 2005.

[35] A. Fillon, G. Abadias, A. Michel, and C. Jaouen, "Stress and microstructure evolution during growth of magnetron-sputtered low-mobility metal films: Influence of the nucleation conditions," in *Thin Solid Films*, 2010.

[36] G. Abadias, Y. Y. Tse, P. Guérin, and V. Pelosin, "Interdependence between stress, preferred orientation, and surface morphology of nanocrystalline TiN thin films deposited by dual ion beam sputtering," *J. Appl. Phys.*, vol. 99, no. 11, p. 113519, 2006.

[37] H. Yang, X. Zhang, Z. Jiang, X. Yang, and Y. Fan, "SiGe quantum dot molecules grown on patterned Si (001) substrates," *J. Appl. Phys.*, vol. 104, no. 4, p. 044303, 2008.

[38] M. J. Rost, "In situ real-time observation of thin film deposition: Roughening, zeno effect, grain boundary crossing barrier, and steering," *Phys. Rev. Lett.*, 2007.

[39] Z. S. Pereira and E. Z. da Silva, "Study of defects in Pd thin films on Au(100) using molecular dynamics," *Phys. Rev. B*, vol. 81, no. 19, p. 195417, May 2010.

[40] H. Hu, H. Gao, and F. Liu, "Quantitative Model of Heterogeneous Nucleation and Growth of SiGe Quantum Dot Molecules," *Phys. Rev. Lett.*, vol. 109, no. 10, p. 106103, Sep. 2012.

[41] Y. Qi, B. W. Sheldon, H. Guo, X. Xiao, and A. K. Kothari, "Impact of Surface Chemistry on Grain Boundary Induced Intrinsic Stress Evolution during Polycrystalline Thin Film Growth," *Phys. Rev. Lett.*, vol. 102, no. 5, p. 056101, Feb. 2009.

[42] J. A. Floro, E. Chason, R. C. Cammarata, and D. J. Srolovitz, "Physical Origins of Intrinsic Stresses in Volmer–Weber Thin Films," *MRS Bull.*, vol. 27, no. 01, pp. 19–25, Jan. 2002.

[43] J. S. Tello, A. F. Bower, E. Chason, and B. W. Sheldon, "Kinetic model of stress evolution during coalescence and growth of polycrystalline thin films," *Phys. Rev. Lett.*, 2007.

[44] A. Fillon, G. Abadias, A. Michel, C. Jaouen, and P. Villechaise, "Influence of phase transformation on stress evolution during growth of metal thin films on silicon," *Phys. Rev. Lett.*, vol. 104, no. 9, p. 96101, 2010.

[45] C.-W. Pao and David J. Srolovitz, “Compressive film stress in a thin, tensile heteroepitaxial film,” *Applied Physics Letters*, 2008. [Online]. Available: http://www.researchgate.net/profile/Chun-Wei_Pao/publication/234940609_Compressive_film_stress_in_a_thin_tensile_heteroepitaxial_film/links/00b7d52b868c8982bc000000.pdf. [Accessed: 06-Nov-2015].

[46] A. Martini, “Short Course on Molecular Dynamics Simulation,” 2009. [Online]. Available: https://nanohub.org/resources/7573/download/Martini_L1_Introduction.pdf.

[47] M. P. Allen and D. J. Tildesley, *Computer Simulation of Liquids*. Clarendon Press, 1989.

[48] M. S. Daw, S. M. Foiles, and M. I. Baskes, “The embedded-atom method: a review of theory and applications,” *Mater. Sci. Reports*, vol. 9, no. 7–8, pp. 251–310, Mar. 1993.

[49] S. M. Foiles, M. I. Baskes, M. S. Daw, M. Foiles, S., I. Baskes,M., and S. Daw, M., “Embedded-atom-method functions for the fcc metals Cu,Ag,Au,Ni,Pd,Pt, and their alloys,” *Phys. Rev. B*, vol. 33, no. 12, pp. 7983–7991, 1986.

[50] J. H. Irving and J. G. Kirkwood, “The Statistical Mechanical Theory of Transport Processes. IV. The Equations of Hydrodynamics,” *J. Chem. Phys.*, vol. 18, no. 6, p. 817, 1950.

[51] N. C. Admal and E. B. Tadmor, “A unified interpretation of stress in molecular systems,” *J. Elast.*, 2010.

[52] M. H. Ulz, K. K. Mandadapu, and P. Papadopoulos, “On the estimation of spatial averaging volume for determining stress using atomistic methods,” *Model. Simul. Mater. Sci. Eng.*, vol. 21, no. 1, p. 015010, 2013.

[53] E. B. Webb, J. A. Zimmerman, and S. C. Seel, “Reconsideration of Continuum Thermomechanical Quantities in Atomic Scale Simulations,” *Math. Mech. Solids*, vol. 13,

no. 3–4, pp. 221–266, May 2008.

[54] J. A. Zimmerman, E. B. WebbIII, J. J. Hoyt, R. E. Jones, P. A. Klein, and D. J. Bammann, "Calculation of stress in atomistic simulation," *Model. Simul. Mater. Sci. Eng.*, vol. 12, no. 4, pp. S319–S332, Jul. 2004.

[55] A. Torres-Sánchez, J. M. Vanegas, and M. Arroyo, "Examining the Mechanical Equilibrium of Microscopic Stresses in Molecular Simulations," *Phys. Rev. Lett.*, vol. 114, no. 25, p. 258102, Jun. 2015.

[56] J. Cormier, J. M. Rickman, and T. J. Delph, "Stress calculation in atomistic simulations of perfect and imperfect solids."

[57] R. C. Cammarata, "Surface and interface stress effects in thin films," *Prog. Surf. Sci.*, vol. 46, no. 1, pp. 1–38, May 1994.

[58] R. Koch, D. Hu, and A. K. Das, "Compressive stress in polycrystalline Volmer-Weber films," *Phys. Rev. Lett.*, vol. 94, p. 146101, 2005.

[59] R. C. Cammarata, T. M. Trimble, and D. J. Srolovitz, "Surface stress model for intrinsic stresses in thin films," *J. Mater. Res.*, vol. 15, no. 11, pp. 2468–2474, Jan. 2000.

[60] C. W. Pao and D. J. Srolovitz, "Stress and morphology evolution during island growth," *Phys. Rev. Lett.*, 2006.

[61] C. Friesen, S. C. Seel, and C. V. Thompson, "Reversible stress changes at all stages of Volmer–Weber film growth," *J. Appl. Phys.*, vol. 95, no. 3, p. 1011, 2004.

[62] J. S. Tello and A. F. Bower, "Numerical simulations of stress generation and evolution in Volmer-Weber thin films," *J. Mech. Phys. Solids*, 2008.

[63] R. W. Hoffman, “Stresses in thin films: The relevance of grain boundaries and impurities,” *Thin Solid Films*, vol. 34, no. 2, pp. 185–190, May 1976.

[64] W. D. Nix and B. M. Clemens, “Crystallite coalescence: A mechanism for intrinsic tensile stresses in thin films,” *J. Mater. Res.*, vol. 14, no. 08, pp. 3467–3473, Jan. 2011.

[65] L. B. Freund and E. Chason, “Model for stress generated upon contact of neighboring islands on the surface of a substrate,” *J. Appl. Phys.*, 2001.

[66] A. Rajamani, B. W. Sheldon, E. Chason, and A. F. Bower, “Intrinsic tensile stress and grain boundary formation during Volmer–Weber film growth,” *Appl. Phys. Lett.*, vol. 81, no. 7, p. 1204, 2002.

[67] A. Bhandari, B. W. Sheldon, and S. J. Hearne, “Competition between tensile and compressive stress creation during constrained thin film island coalescence,” *J. Appl. Phys.*, 2007.

[68] P. R. Guduru, E. Chason, and L. B. Freund, “Mechanics of compressive stress evolution during thin film growth,” *J. Mech. Phys. Solids*, vol. 51, no. 11–12, pp. 2127–2148, Nov. 2003.

[69] C. W. Pao, D. J. Srolovitz, and C. V. Thompson, “Effects of surface defects on surface stress of Cu(001) and Cu(111),” *Phys. Rev. B - Condens. Matter Mater. Phys.*, 2006.

[70] C.-W. Pao, S. M. Foiles, E. B. Webb, D. J. Srolovitz, and J. A. Floro, “Atomistic simulations of stress and microstructure evolution during polycrystalline Ni film growth,” *Phys. Rev. B*, vol. 79, no. 22, p. 224113, Jun. 2009.

[71] E. Chason, B. W. Sheldon, L. B. Freund, J. A. Floro, and S. J. Hearne, “Origin of compressive residual stress in polycrystalline thin films.,” *Phys. Rev. Lett.*, vol. 88, no. 15, 2002.

[72] J. Leib, R. Mönig, and C. V. Thompson, “Direct Evidence for Effects of Grain Structure on Reversible Compressive Deposition Stresses in Polycrystalline Gold Films,” *Phys. Rev. Lett.*, vol. 102, no. 25, p. 256101, Jun. 2009.

[73] Y. Pauleau, “Generation and evolution of residual stresses in physical vapour-deposited thin films,” *Vacuum*, vol. 61, no. 2–4, pp. 175–181, May 2001.

[74] D. Magnfält, G. Abadias, and K. Sarakinos, “Atom insertion into grain boundaries and stress generation in physically vapor deposited films,” *Appl. Phys. Lett.*, vol. 103, no. 5, p. 051910, 2013.

[75] Y. Yang, H. Huang, S. K. Xiang, and E. Chason, “Stress control in polycrystalline thin films-reduction in adatoms diffusion into grain boundaries via surfactants,” *Appl. Phys. Lett.*, 2010.

[76] B. W. Sheldon, A. Bhandari, A. F. Bower, S. Raghavan, X. Weng, and J. M. Redwing, “Steady-state tensile stresses during the growth of polycrystalline films,” *Acta Mater.*, 2007.

[77] R. Birringer and P. Zimmer, “Grain- and phase-boundary stress effects in nanocrystalline materials,” *Acta Mater.*, vol. 57, no. 6, pp. 1703–1716, Apr. 2009.

[78] E. Chason, J. W. Shin, S. J. Hearne, and L. B. Freund, “Kinetic model for dependence of thin film stress on growth rate, temperature, and microstructure,” *J. Appl. Phys.*, 2012.

[79] A. González-González, C. Polop, and E. Vasco, “Postcoalescence evolution of growth stress in polycrystalline films,” *Phys. Rev. Lett.*, 2013.

[80] C. V. Thompson and R. Carel, “Stress and grain growth in thin films,” *J. Mech. Phys. Solids*, vol. 44, no. 5, pp. 657–673, May 1996.

[81] J. Proost and F. Spaepen, “Evolution of the growth stress, stiffness, and microstructure of alumina thin films during vapor deposition,” *J. Appl. Phys.*, vol. 91, no. 1, p. 204, 2002.

[82] L. Ç. Arslan, C. Sanborn, E. Anzenberg, and K. F. Ludwig, “Evidence for Family-Meakin Dynamical Scaling in Island Growth and Coalescence during Vapor Phase Deposition,” *Phys. Rev. Lett.*, vol. 109, no. 10, p. 106102, Sep. 2012.

[83] C. Ayas and E. Van Der Giessen, “A continuum framework for grain boundary diffusion in thin film/substrate systems,” *J. Appl. Phys.*, 2010.

[84] C. Ayas and E. Van der Giessen, “Stress relaxation in thin film/substrate systems by grain boundary diffusion: a discrete dislocation framework,” *Modelling and Simulation in Materials Science and Engineering*. 2009.

[85] C.-W. Pao, D. J. Srolovitz, and H. W. Zandbergen, “Thermodynamic and kinetic properties of surface dislocations on Au(001) from atomistic simulations,” *Phys. Rev. B*, vol. 75, no. 19, p. 195405, May 2007.

[86] H. W. Zandbergen, C.-W. Pao, and D. J. Srolovitz, “Dislocation Injection, Reconstruction, and Atomic Transport on {001} Au Terraces,” *Phys. Rev. Lett.*, vol. 98, no. 3, p. 036103, Jan. 2007.

[87] H. Zheng, “Molecular Dynamic Simulation of Thin Film Growth Stress Evolution,” Lehigh University, 2011.

[88] W. R. Tyson and W. A. Miller, “Surface free energies of solid metals: Estimation from liquid surface tension measurements,” *Surf. Sci.*, vol. 62, no. 1, pp. 267–276, Jan. 1977.

[89] G. L. Kellogg and R. Plass, “The relationship between the growth shape of three-dimensional Pb islands on Cu(100) and the domain orientation of the underlying c(5×)R45

structure," *Surf. Sci.*, vol. 465, no. 3, pp. L777–L782, Oct. 2000.

[90] J. Luo, H. Cheng, K. M. Asl, C. J. Kiely, and M. P. Harmer, "The Role of a Bilayer Interfacial Phase on Liquid Metal Embrittlement," *Sci.* , vol. 333 , no. 6050 , pp. 1730–1733, Sep. 2011.

[91] G. Ehrlich, "Atomic View of Surface Self-Diffusion: Tungsten on Tungsten," *J. Chem. Phys.*, vol. 44, no. 3, p. 1039, Jan. 1966.

[92] R. L. Schwoebel, "Step Motion on Crystal Surfaces," *J. Appl. Phys.*, vol. 37, no. 10, p. 3682, Jun. 1966.

[93] C. M. Retford, M. Asta, M. J. Miksis, P. W. Voorhees, and E. B. Webb, "Energetics of {105}-faceted Ge nanowires on Si(001): An atomistic calculation of edge contributions," *Phys. Rev. B - Condens. Matter Mater. Phys.*, 2007.

[94] J. Vlassak, "Thin Film Mechanics," 2004.

[95] C. Teodosiu, *Elastic Models of Crystal Defects*. Berlin, Heidelberg: Springer Berlin Heidelberg, 1982.

[96] Van Vliet and Krystyn J., *Mechanical Behavior of Materials*. 2006.

[97] J. W. Matthews and A. E. Blakeslee, "Defects in epitaxial multilayers," *J. Cryst. Growth*, vol. 27, pp. 118–125, Dec. 1974.

Vita

I was born in Samsun, a coastal city in the north of Turkey in June, 1981.My father Mustafa and mother Arife are both teachers. I have one younger brother, M. Serhat who is working as a software engineer in Turkey. I got married with Saliha, who is also a teacher, in 2012 and became father to my son, Mehmet, in May 2013 and to my daughter Melek Seniha, in December 2015.

I had my bachelor's degree in mechanical engineering at Middle East Technical University in 2003 as an honor student.

After working in the industry as a manufacturing engineer about a year and a half I received Turkish Petroleum Company's (TPIC) scholarship for masters at Rutgers University in 2005 and came to US. I completed my masters at Rutgers University, with special focus on biomaterials and biomechanical applications in 2007 and went back to Turkey to work for TPIC as a manufacturing engineer in Ankara. I worked there for almost 2 years.

In order to continue my career in academia, I came to Lehigh University in 2009 for PhD. Started my research with my advisor Edmund B. Webb III and completed my dissertation in December, 2015.